RMN de sólidos

Aplicações ao estudo de meios porosos

Jair C. C. Freitas

Departamento de Física - UFES

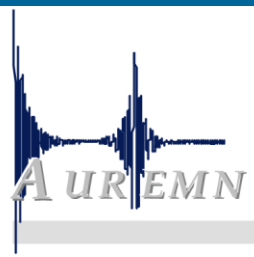

CURSO AUREMN - MAIO/2015
RMN APLICADA À CIÊNCIA DO PETRÓLEO
04 A 08 DE MAIO DE 2015
Universidade Federal do Espírito Santo (UFES)

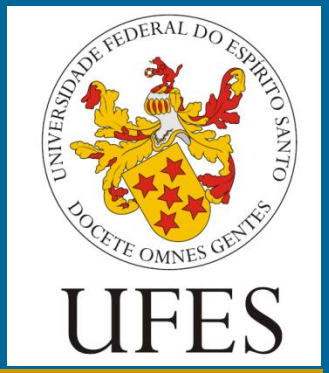

Sumário

- Fundamentos sobre RMN de sólidos:
  - Introdução geral.
  - Interações anisotrópicas.
  - Alargamento homogêneo e inomogêneo.
- RMN de sólidos:
  - Técnicas de alta resolução.
  - Instrumentação para RMN de sólidos.

Sumário

- RMN em meios porosos:
  - Contraste de suscetibilidade magnética.
  - Relaxometria por RMN de ^{1}H
    - Aplicações em petrofísica.
  - Utilização de métodos de RMN de sólidos.
  - Materiais micro e mesoporosos:
    - Materiais de carbono.
    - Silicatos.
    - Estruturas metal-orgânicas (MOFs).

Generalidades sobre RMN

Precessão de Larmor:

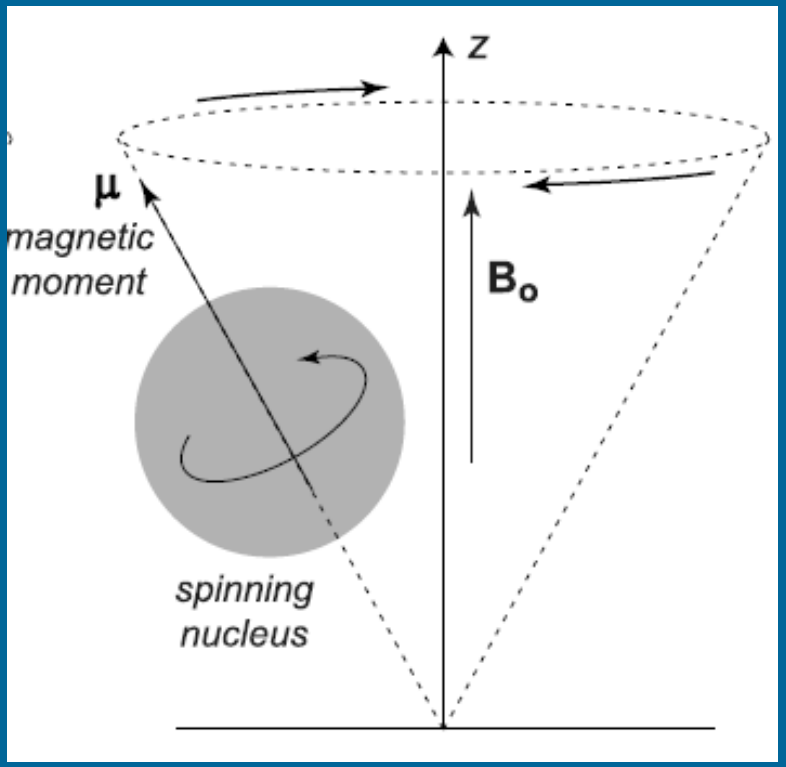

Frequência de Larmor:

$$\omega_L = \gamma B_0$$ (~10^7 rad/s)

$$f_L = \gamma B_0 / 2\pi$$ (~MHz)

↓

Radiofrequência (RF)

Generalidades sobre RMN

Nuclide	*Natural abundance* (%)	*Nuclear spin*	*Larmor frequency* [a] (MHz)	*Sensitivity* [b]
^{1}H	99.99	1/2	100.000	1.000
^{13}C	1.07	1/2	25.145	1.70×10^{-4}
^{14}N	99.632	1	7.226	1.00×10^{-3}
^{17}O	0.038	5/2	13.556	1.11×10^{-5}
^{23}Na	100	3/2	26.452	9.27×10^{-2}
^{27}Al	100	5/2	26.057	0.207
^{29}Si	4.683	1/2	19.867	3.68×10^{-4}
^{31}P	100	1/2	40.481	6.65×10^{-2}
^{33}S	0.76	3/2	7.676	1.72×10^{-5}
^{39}K	93.258	3/2	4.666	4.76×10^{-4}
^{43}Ca	0.135	7/2	6.730	8.68×10^{-6}
^{129}Xe	26.44	1/2	27.810	5.72×10^{-3}

[a] Corresponding to the magnetic field of 2.35 T of a 100 MHz NMR spectrometer.
[b] Relative to ^{1}H.

Harris et al., *Pure Appl. Chem.* 2001;73(11):1795-1818

Generalidades sobre RMN

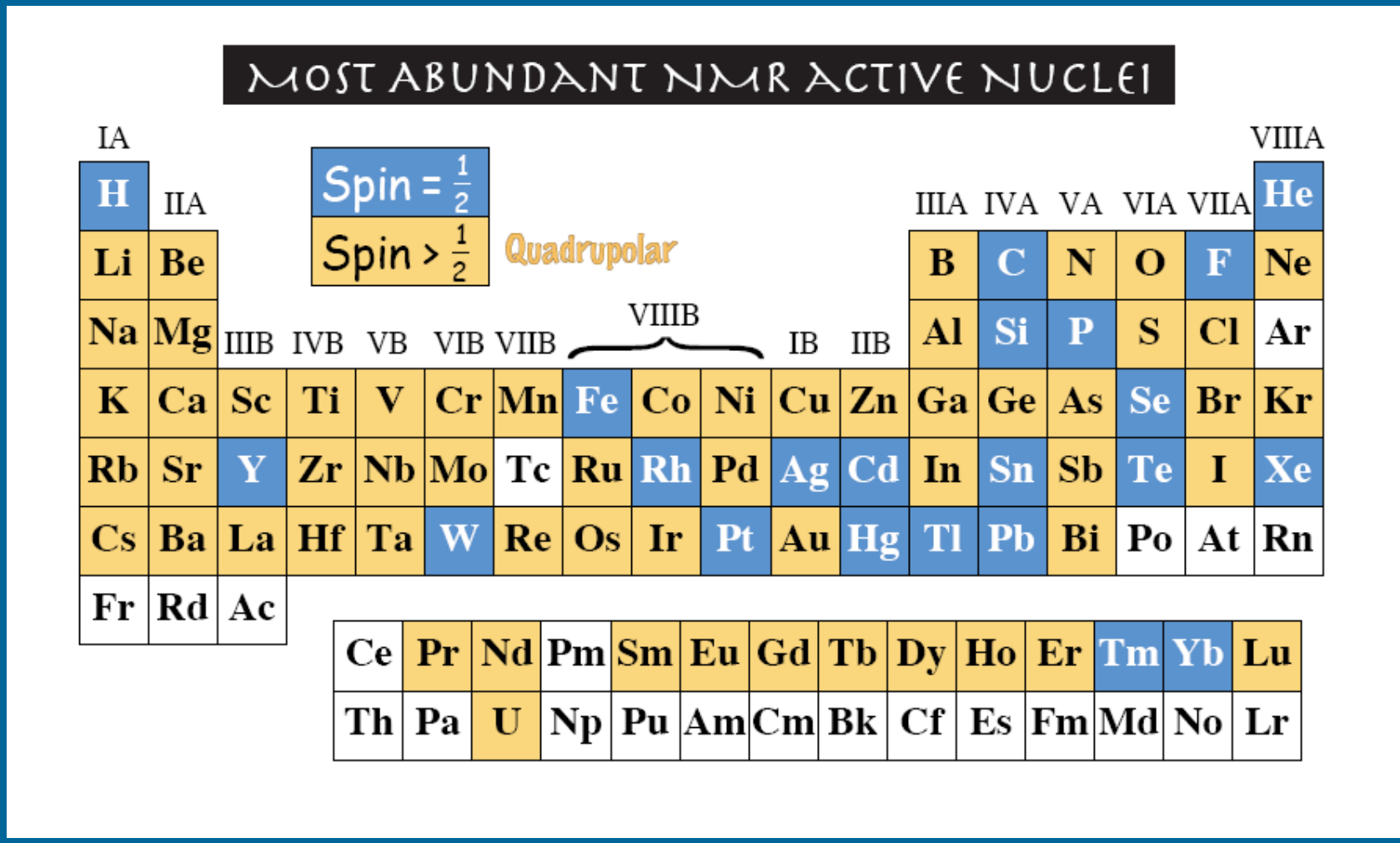

http://www.grandinetti.org/Research/NMR

Generalidades sobre RMN

Paramagnetismo nuclear:

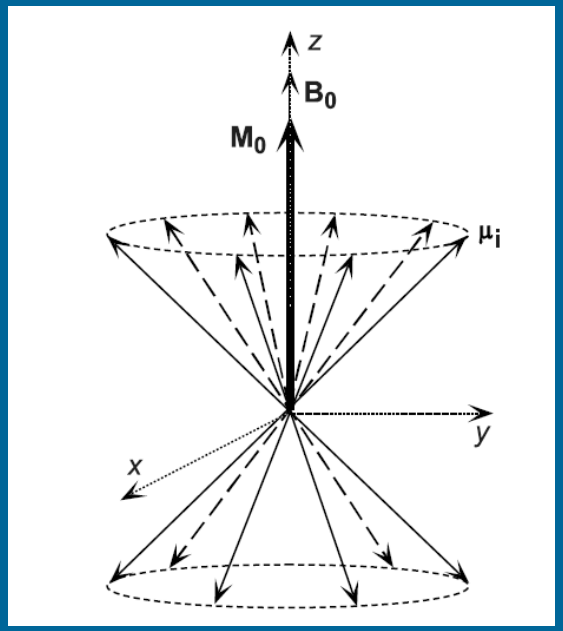

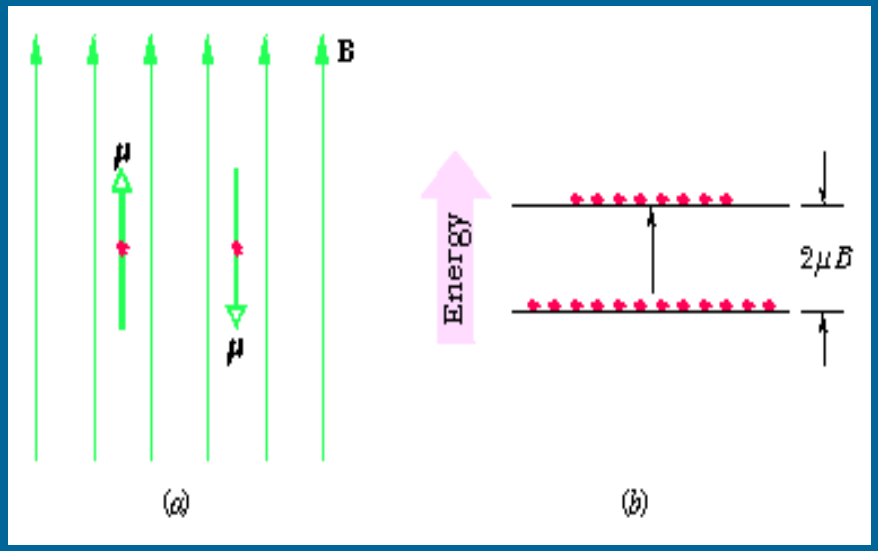

$$\mathrm{M}_0 = \frac{N\mu^2 B_0}{3kT}$$

$$E = -\vec{\mu} \cdot \vec{B}_0 = -\gamma m \hbar B_0 = -m\hbar\omega_L$$

$$\frac{n_-}{n_+} = \mathrm{e}^{(-\hbar\omega_L / kT)}$$

Generalidades sobre RMN

$$B_0 \sim 1\text{T} \Rightarrow \begin{cases} f_L \sim 43\ \text{MHz} \ (^1\text{H}) \\ f_L \sim 28\ \text{GHz} \ (\text{elétron}) \end{cases}$$

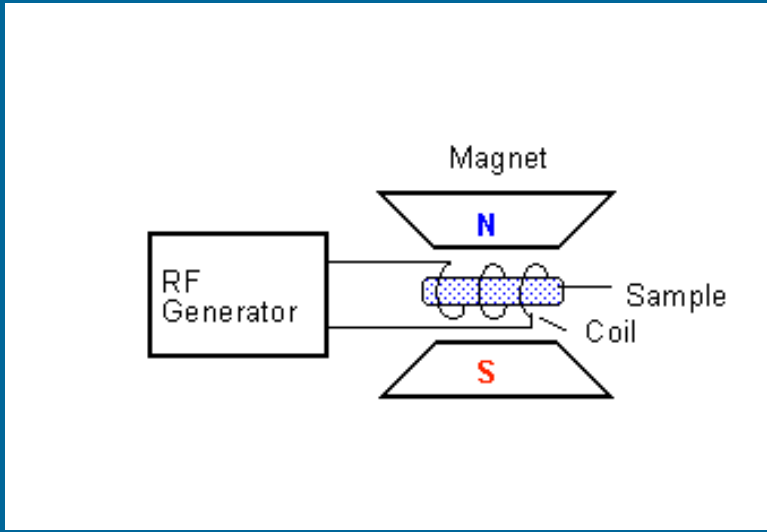

Campo de RF: $B_1 \sim 10\text{G} = 10^{-3}\text{T}$

Campo da Terra: $B_T \sim 10^{-5}\text{T}$

$$\vec{B}_0 = B_0 \hat{z}$$

$$\vec{B}_1 = (2B_1 \cos \omega t)\hat{x}$$

Pulsos de RF

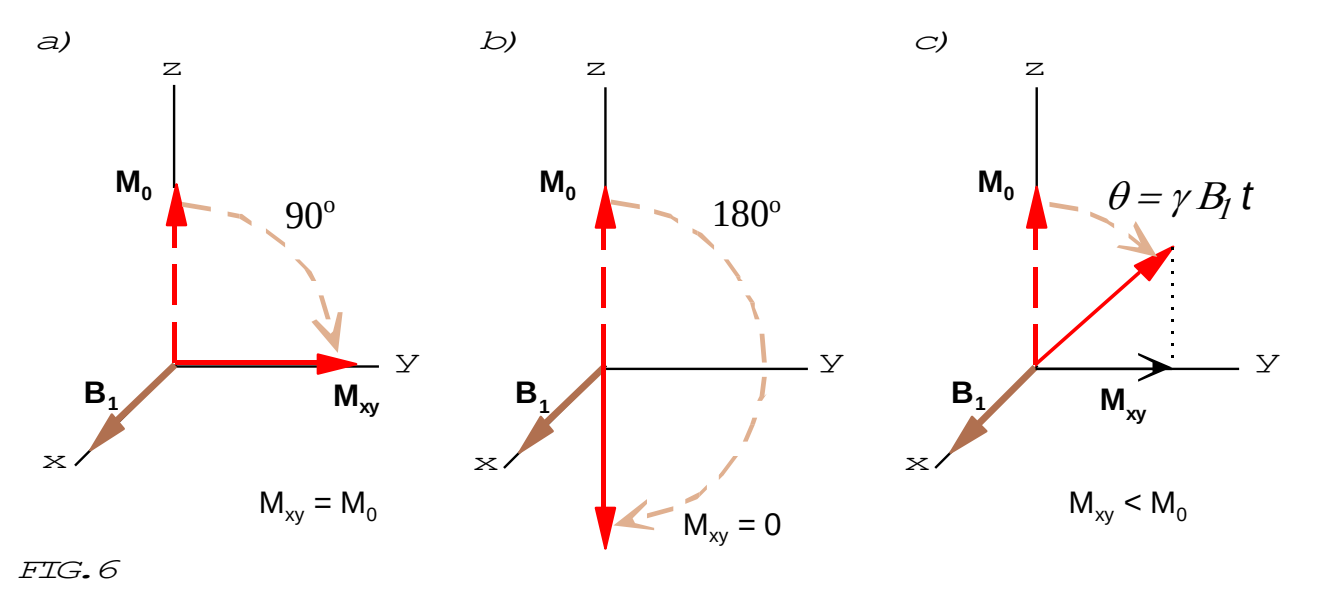

FIG. 6

Pulso π/2

Pulso π

Pulso θ

Controle

- Duração (~ μs)
- Amplitude (~ 10^2 kHz)
- Fase (0, 90°, 180°, 270°)

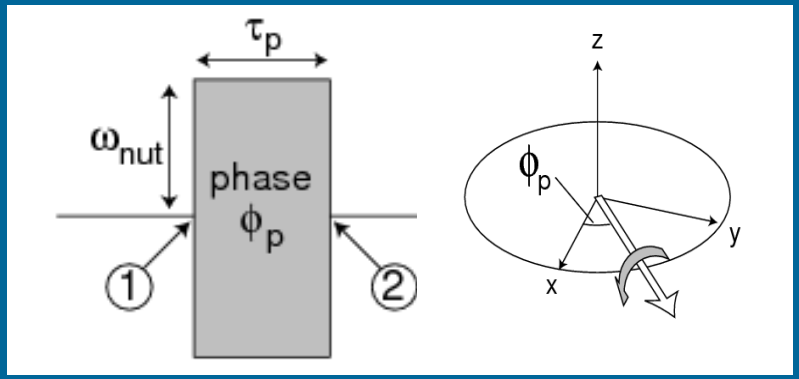

Detecção do sinal de RMN

FID = decaimeno livre de indução

ω_L

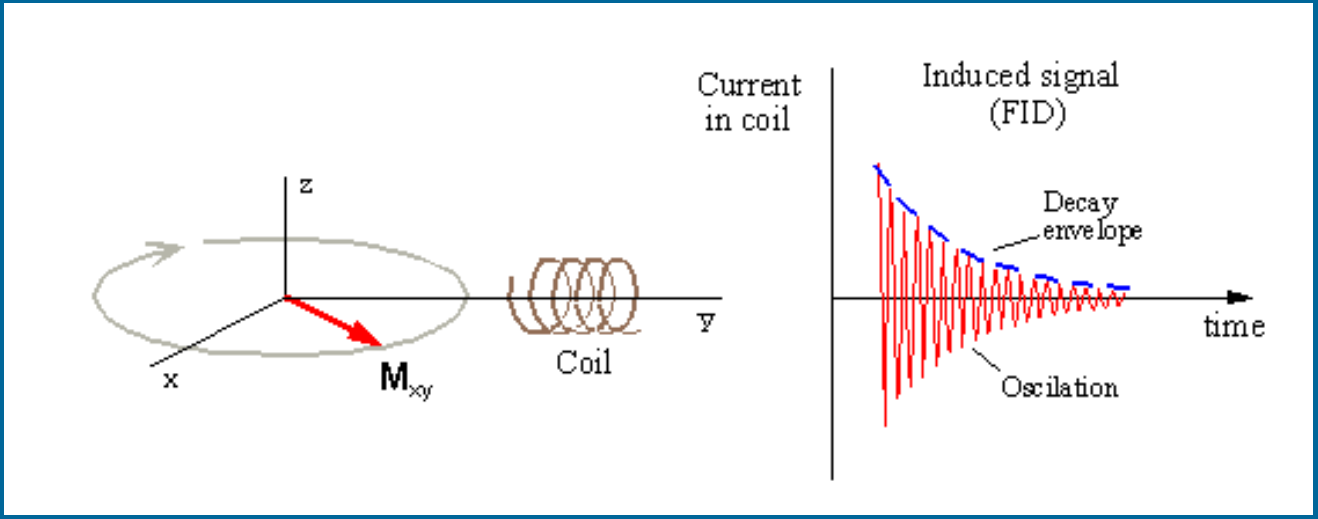

Transformada de Fourier (FT)

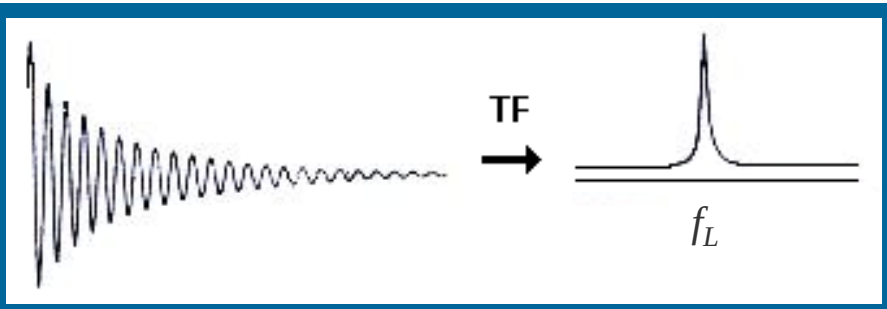

FID

Espectro

Um experimento simples de RMN (1D)

Experimento de **pulso simples** ou **decaimento de Bloch**:

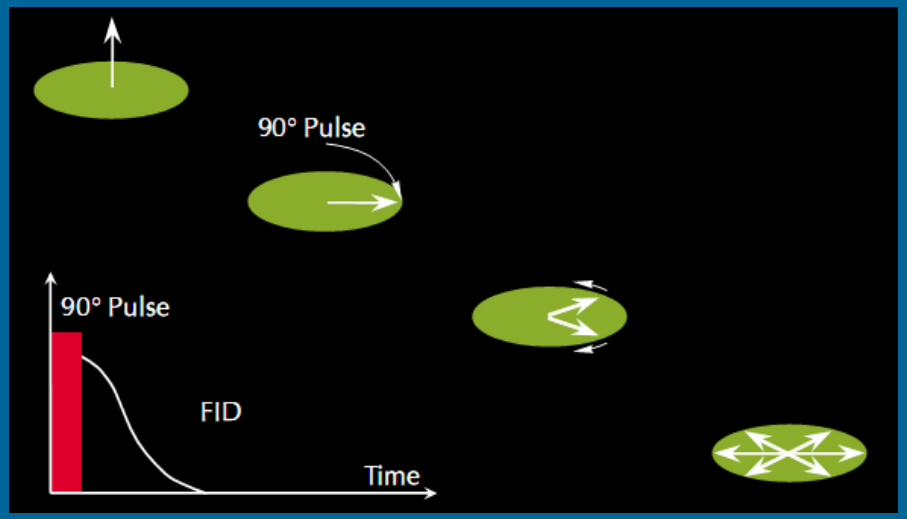

Sinal detectado com frequência:
$\Delta f = f_L - f_{RF}$ (áudio)

Sinal em ressonância: $\Delta f = 0$

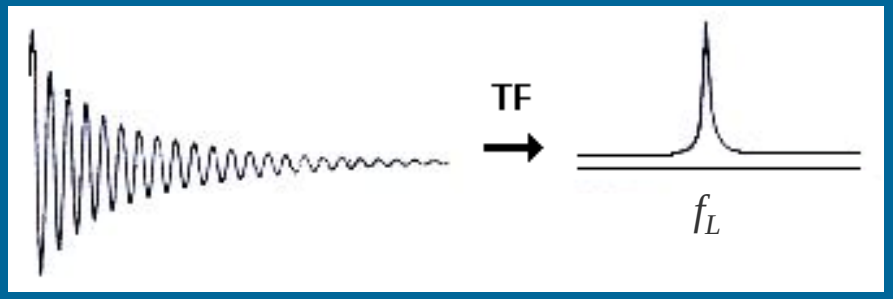

FID

Espectro

Relaxação do sistema de spins

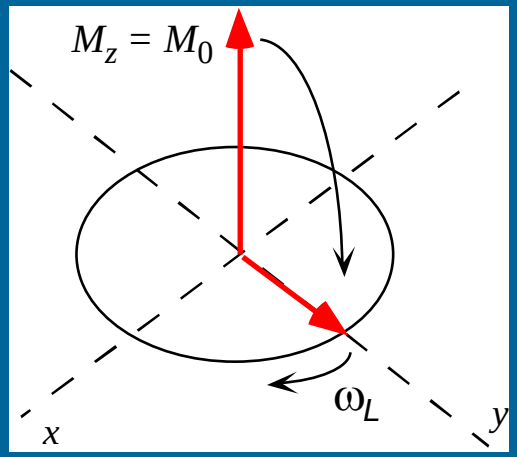

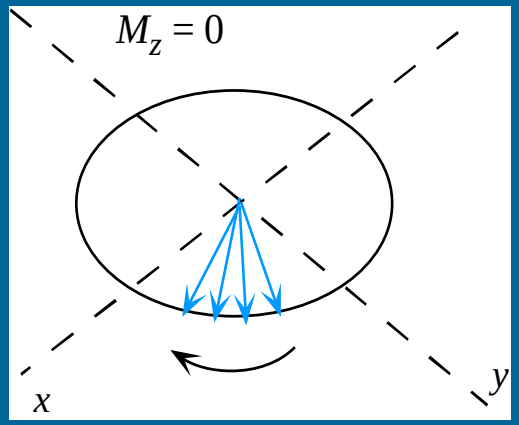

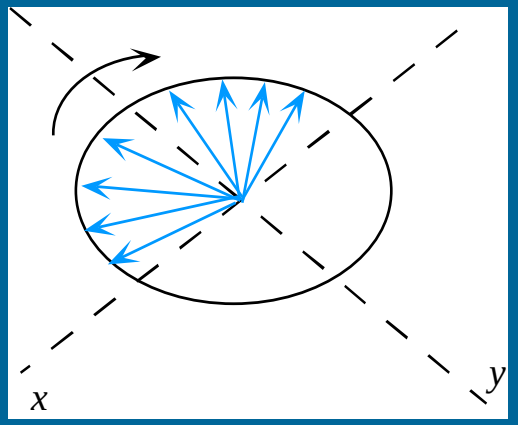

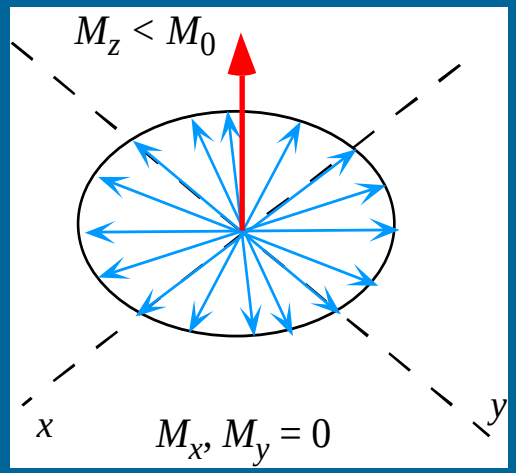

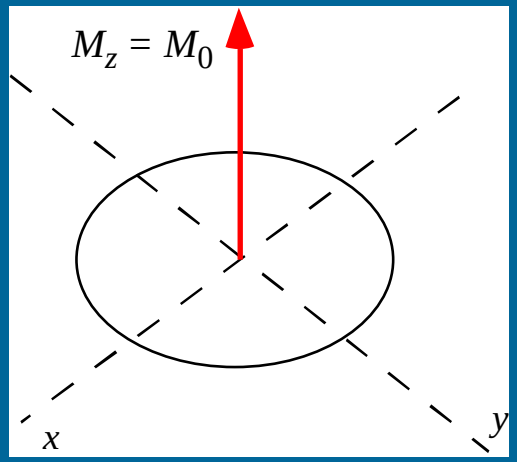

Relaxação transversal

- Inomogeneidade do campo magnético:

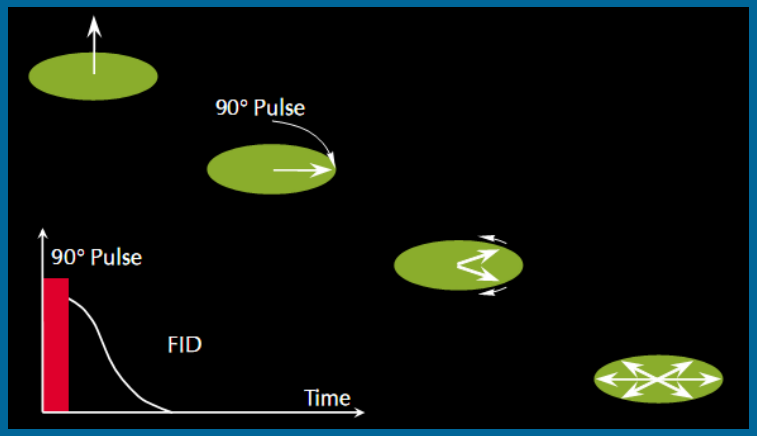

$$\omega_L(\mathbf{r}) = \gamma B_0(\mathbf{r})$$

$$\Omega(\mathbf{r}) = \omega_L(\mathbf{r}) - \omega_{RF}$$

$$S_{\text{total}}(t) = \int\int\int \rho(\mathbf{r}) e^{i\Omega(\mathbf{r})t} \cdot e^{-t/T_2} dV$$

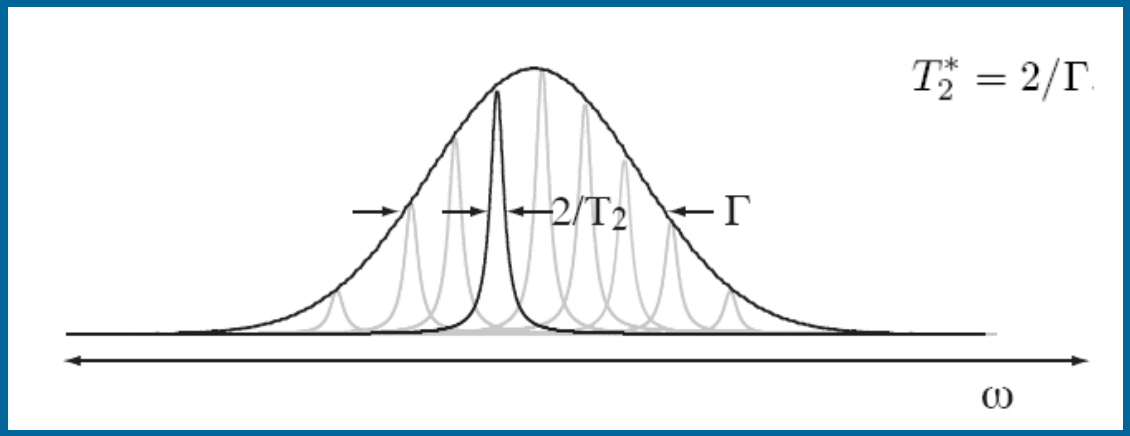

$$\frac{1}{T_2^*} = \frac{1}{T_2} + \gamma \Delta B_0$$

http://grandinetti.org/Teaching/Chem824/Notes

Relaxação transversal

- Inomogeneidade do campo magnético:

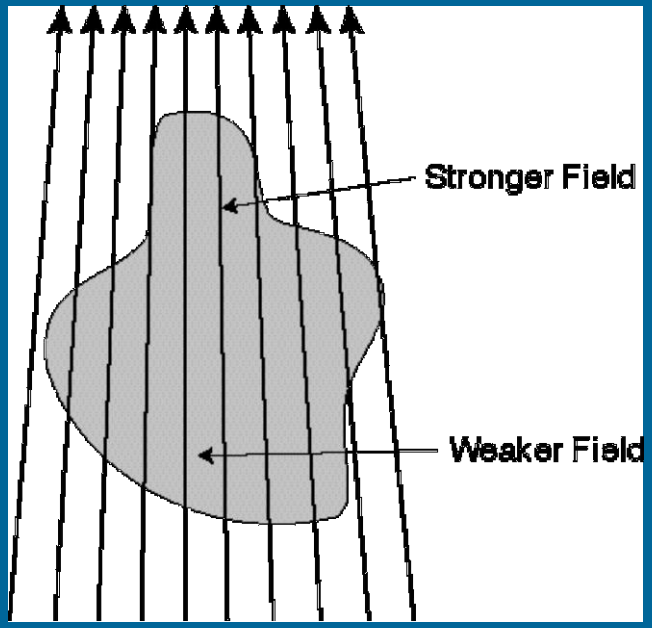

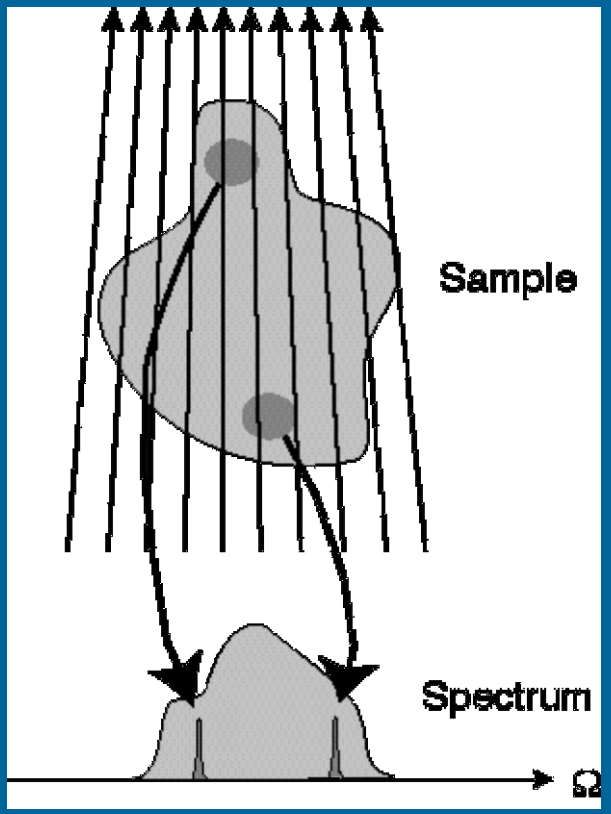

"Spin dynamics", M. H. Levitt. John Wiley & Sons, 2002.

Relaxação transversal

- Relaxação transversal em sólidos:

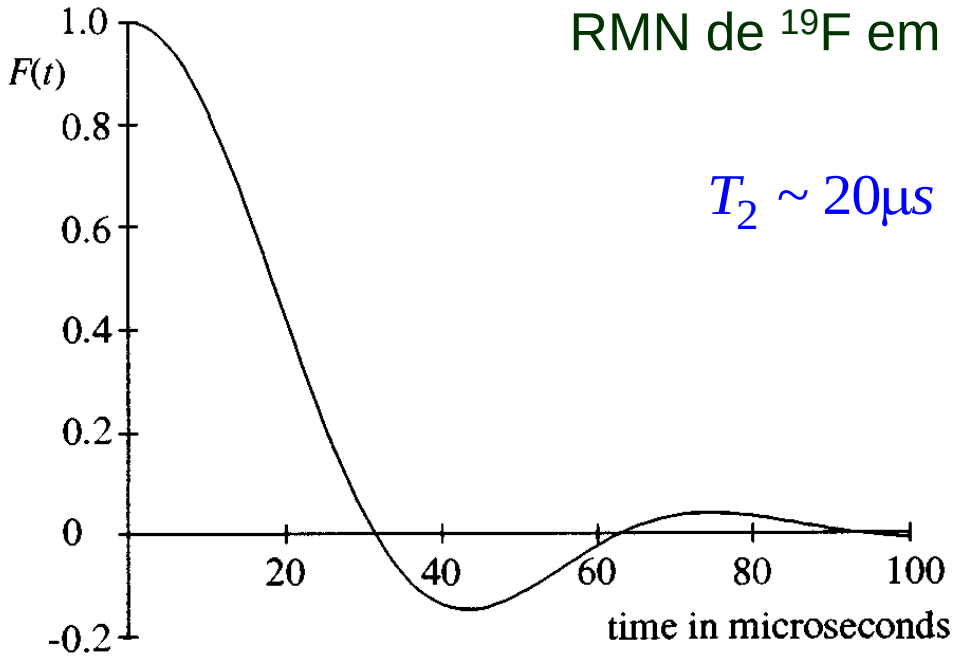

Figure 4.2 FID of calcium fluoride.

"NMR and relaxation", Cowan. Cambridge University Press, 1997.

Relaxação transversal

- Relaxação transversal em líquidos:

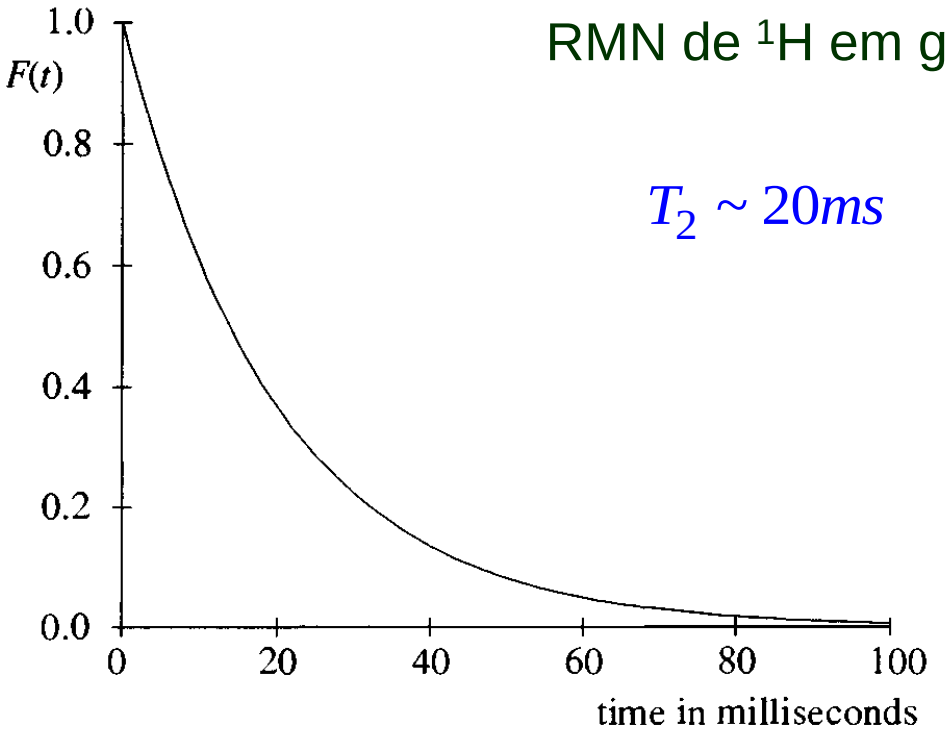

RMN de ^{1}H em glicerol

$T_2 \sim 20ms$

Figure 4.3 Proton transverse relaxation in glycerol.

"NMR and relaxation", Cowan. Cambridge University Press, 1997.

Sequência CPMG

Carr & Purcell (1954); Meiboom & Gill (1958)

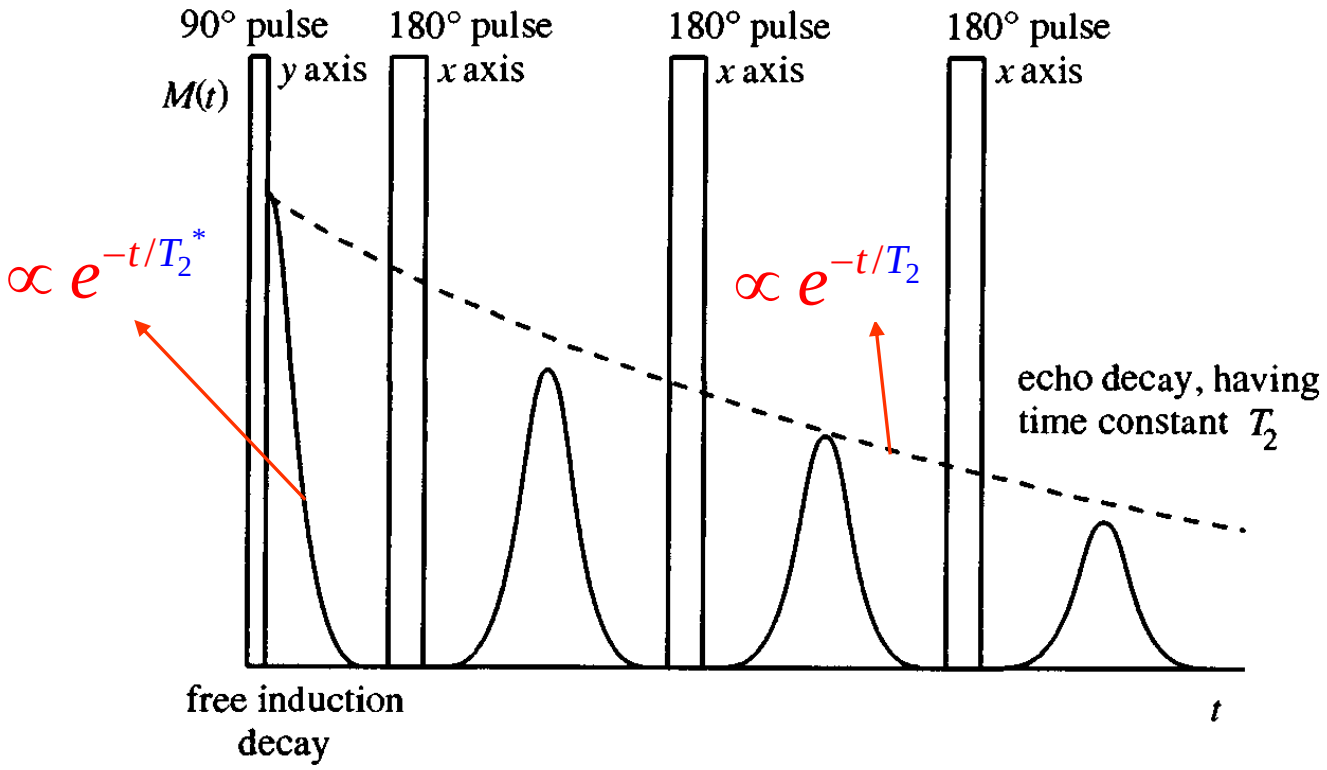

Figure 4.13 Carr–Purcell–Meiboom–Gill sequence.

"NMR and relaxation", Cowan. Cambridge University Press, 1997.

Sequência CPMG

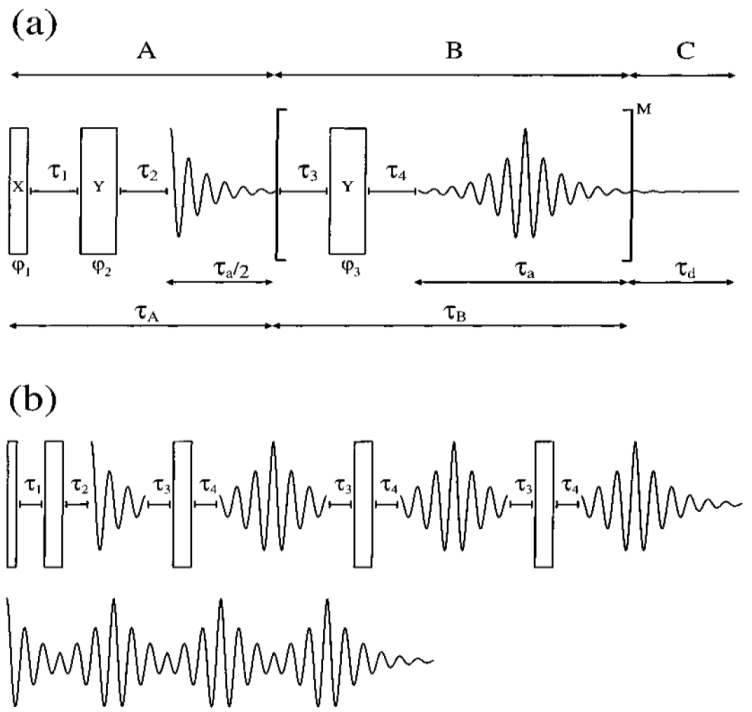

Figure 1. Quadrupolar CPMG (QCPMG) pulse sequence for sensitivity-enhanced quadrupolar-echo (QE) solid-state NMR of half-integer quadrupolar nuclei: (a) timing scheme of the pulse sequence; (b) relation between the pulse sequence timing t and the timing t_2 of the free induction decay (see text). Shaded and open bars correspond to selective (central transition) $\pi/2$ and π pulses, respectively. The phases ϕ_1, ϕ_2, ϕ_3, and the receiver reference phase ϕ_{rec} are cycled (see Table 2) to select the $p = 0 \rightarrow \pm 1 \rightarrow \mp 1 \rightarrow \pm 1$ etc. coherence transfer pathways.

Larsen et al., *J. Phys. Chem. A* 101 (1997) 8597

RMN de ^{25}Mg – $Mg(OAc)_2 \cdot 4H_2O$

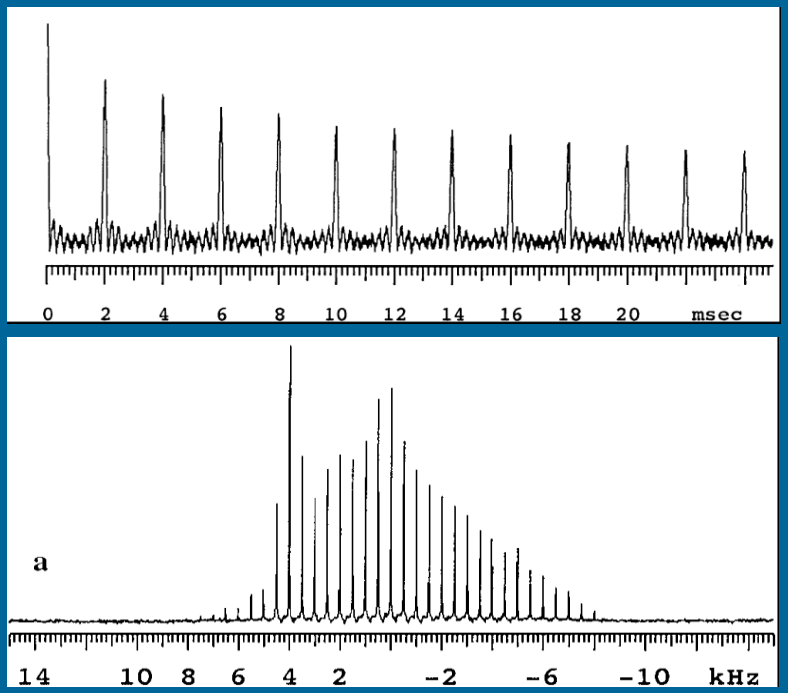

Ellis et al., *J. Magn. Reson.* 151 (2001) 48

Alargamento homogêneo e inomogêneo em sólidos

RMN de ^{13}C – uso de MAS e sequência CPMG:

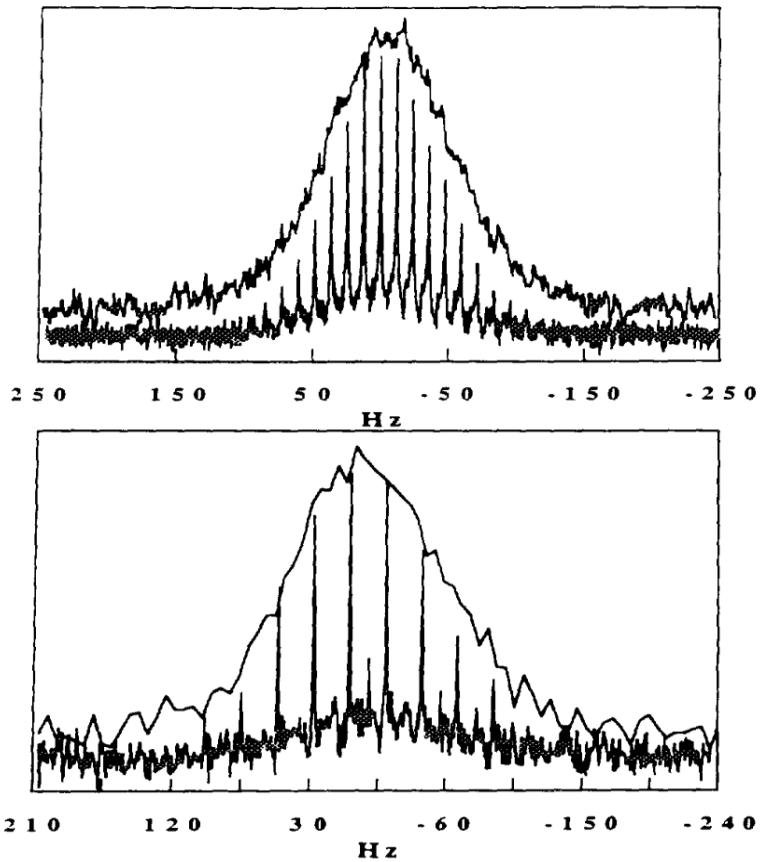

FIG. 6. CPMAS and spin-echo spectra taken on-resonance for the methyl (top) and isotropic aromatic (bottom) resonances of HMB. The τ value used for the methyl spectrum was approximately double that used for the aromatic spectrum.

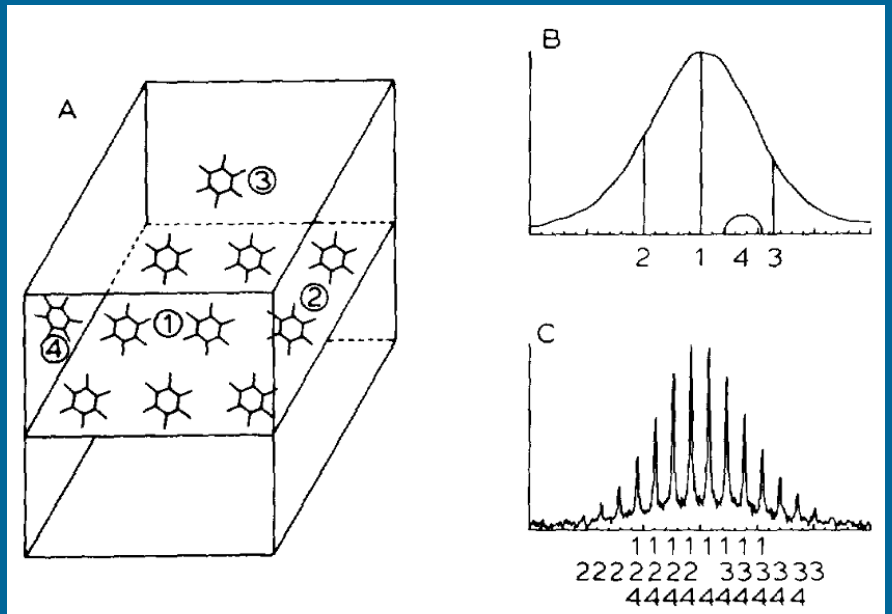

FIG. 7. The effect of various contributions broadened by ABMS on the spike spectrum. (A) Crystallite model showing location of various contributions. 1, molecule in the center of a crystallite in the 001 plane; 2, molecule at the edge of a crystallite in the 001 plane; 3, molecule at the edge of a crystallite not in the 001 plane; 4, molecule in the defect site. (B) Contribution of frequencies from various sites in a single crystallite to the MAS spectrum. (C) Contribution of frequencies from various sites to the echo spectrum.

Cowans & Grutzner, *J. Magn. Reson.* 1993;105:10-18.

Interações de spin nuclear

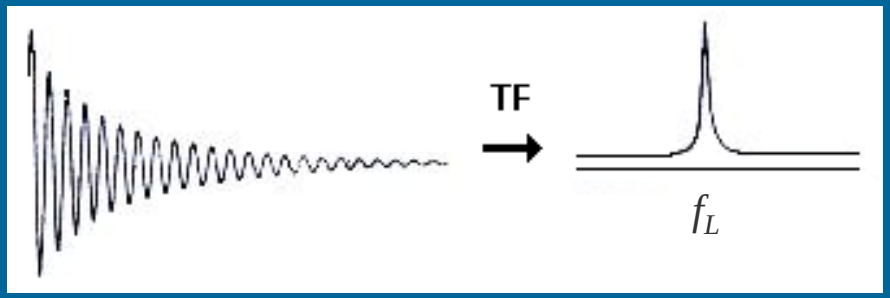

$$f_L = \gamma B_0 / 2\pi$$

- Núcleo atômico *isolado*: medida de f_L fornece B_0 ou γ.
- Núcleo atômico na *matéria*: espectros de RMN (contendo vários valores ou distribuições de f_L) fornecem informações sobre a estrutura da matéria.

Interações de spin nuclear

Materiais isolantes e diamagnéticos:

- Deslocamento químico: Termo isotrópico + parte anisotrópica
- Interação dipolar direta: Homonuclear ou heteronuclear.
- Acoplamento escalar *(J)*: Termo isotrópico.
- Interação quadrupolar: $I > 1/2$.

Interações de spin nuclear

Materiais isolantes e diamagnéticos:

- Hamiltoniano contendo diferentes interações:

$$H_{spin} = \underbrace{H_0 + H_{RF}}_{H_{ext}} + \underbrace{H_{DQ} + H_{dip} + H_J + H_Q}_{H_{int}}$$

$$H_{ext} = -\vec{\mu} \cdot \vec{B}_0 - \vec{\mu} \cdot \vec{B}_1(t)$$

$$H_{int}$$

Deslocamento químico ("chemical shift")

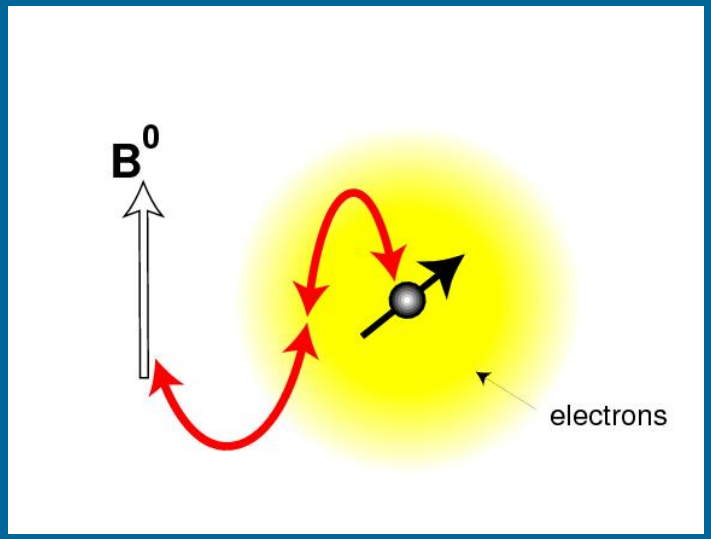

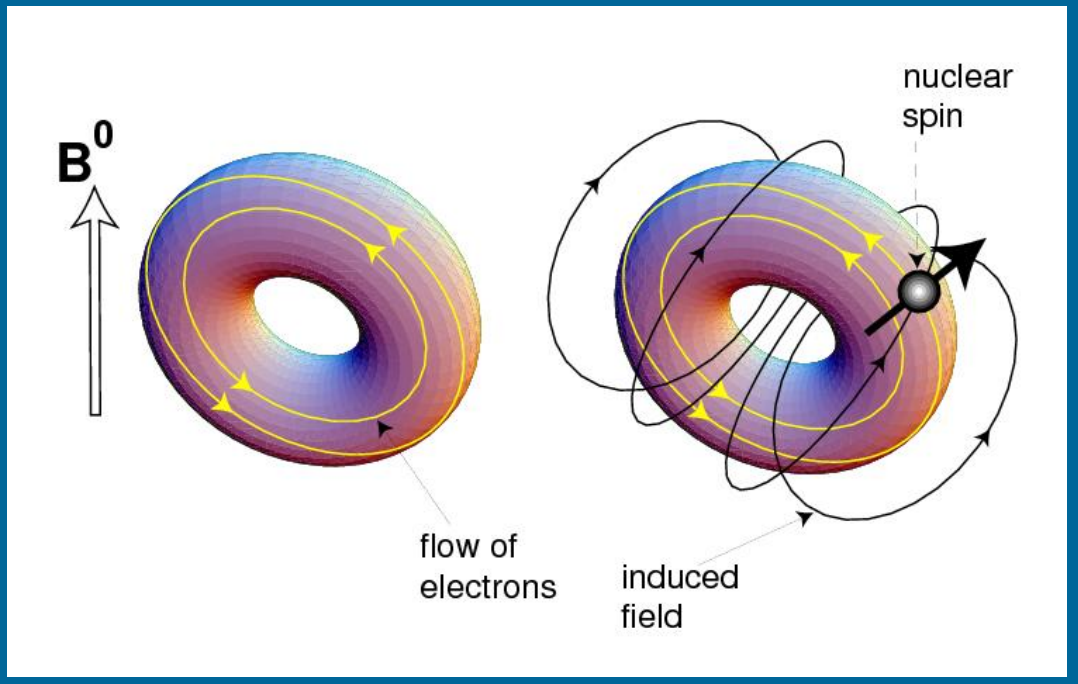

Em líquidos:

$$\omega = \gamma B_{loc} = \gamma(1-\sigma_{iso})B_0$$

$$\delta = (f_{obs} - f_{ref}) / f_{ref}$$

ppm TMS

$$\delta = \frac{f_{obs} - f_{ref}}{f_{ref}} = \frac{\sigma_{ref} - \sigma_{obs}}{1-\sigma_{ref}} \cong \sigma_{ref} - \sigma_{obs}$$

"Spin dynamics", M. H. Levitt. John Wiley & Sons, 2002.

Deslocamento químico em líquidos

RMN de ^{1}H

CH_3CH_2OH

Packard et al. (1951)

$$\vec{B}_{loc} = (1-\sigma_{iso})\vec{B}_0$$

$$f_{obs} = \frac{\gamma B_{loc}}{2\pi} = f_L(1-\sigma_{iso})$$

$$\delta = \frac{f_{obs} - f_{ref}}{f_{ref}}$$

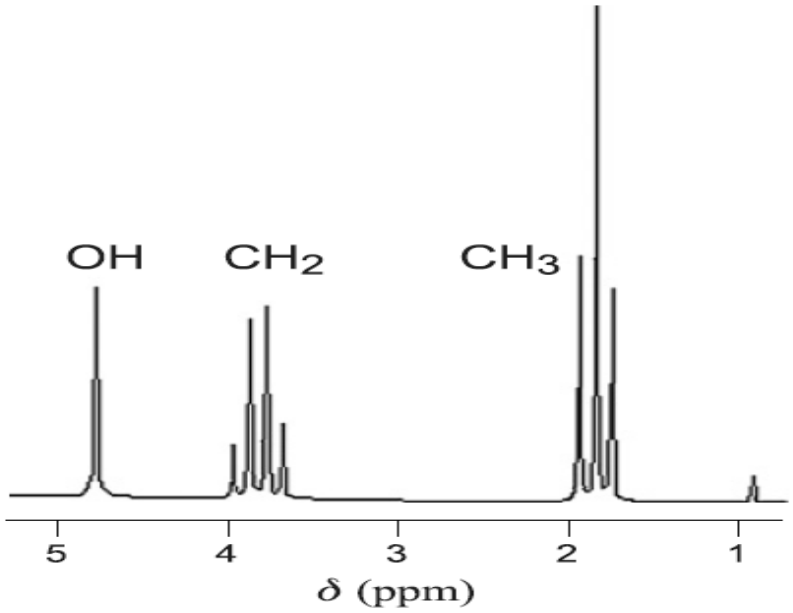

Valores típicos (^{1}H):

f_{ref} ~ 400MHz (TMS)

$f_{obs} - f_{ref}$ ~ 400-4000 Hz

$\delta \sim 10^{-6}$: partes por milhão (ppm)

Deslocamento químico em sólidos

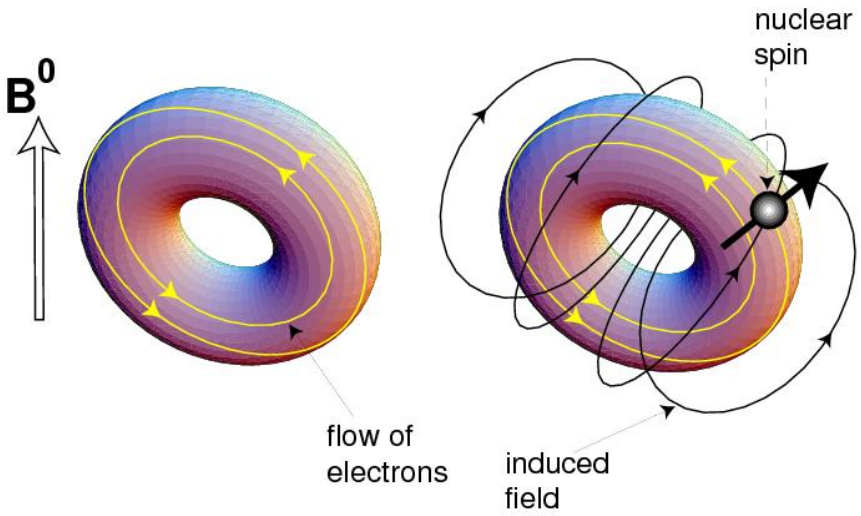

$$\vec{B}^{ind} = -\tilde{\sigma} \cdot \vec{B}_0$$

$$\begin{pmatrix} B_x^{ind} \\ B_y^{ind} \\ B_z^{ind} \end{pmatrix} = - \begin{pmatrix} \sigma_{xx} & \sigma_{xy} & \sigma_{xz} \\ \sigma_{yx} & \sigma_{yy} & \sigma_{yz} \\ \sigma_{zx} & \sigma_{zy} & \sigma_{zz} \end{pmatrix} \begin{pmatrix} 0 \\ 0 \\ B_0 \end{pmatrix}$$

$\tilde{\sigma}$: tensor de blindagem magnética ("*chemical shielding*")

$$\vec{B}^{loc} = \vec{B}_0 + \vec{B}^{ind} = (1 - \tilde{\sigma}) \cdot \vec{B}_0$$

$$H_{DQ} = -\vec{\mu} \cdot \vec{B}^{ind} = \gamma \hbar \vec{I} \cdot \tilde{\sigma} \cdot \vec{B}_0$$

"Spin dynamics", M. H. Levitt. John Wiley & Sons, 2002.

Deslocamento químico em sólidos

Sistema de laboratório:

$$\tilde{\sigma}^{SLAB} = \begin{pmatrix} \sigma_{xx} & \sigma_{xy} & \sigma_{xz} \\ \sigma_{yx} & \sigma_{yy} & \sigma_{yz} \\ \sigma_{zx} & \sigma_{zy} & \sigma_{zz} \end{pmatrix}$$

$$\left|\sigma_{ZZ} - \sigma_{iso}\right| \geq \left|\sigma_{XX} - \sigma_{iso}\right| \geq \left|\sigma_{YY} - \sigma_{iso}\right|$$

Sistema de eixos principais:
(fixo com relação à molécula)

$$\tilde{\sigma}^{SEP} = \begin{pmatrix} \sigma_{XX} & 0 & 0 \\ 0 & \sigma_{YY} & 0 \\ 0 & 0 & \sigma_{ZZ} \end{pmatrix}$$

Deslocamento químico isotrópico:

$$\sigma_{iso} = \frac{1}{3}(\sigma_{XX} + \sigma_{YY} + \sigma_{ZZ})$$

Constante de anisotropia:

$$\zeta = \sigma_{ZZ} - \sigma_{iso}$$

Parâmetro de assimetria:

$$\eta = \frac{\sigma_{YY} - \sigma_{XX}}{\zeta}$$

$$0 \leq \eta \leq 1$$

Harris et al., *Pure Appl Chem.* 2008;80:59-84

Deslocamento químico em sólidos

Frequência dependente da orientação molecular:

Alargamento inomogêneo

$$\omega(\theta,\phi) = \omega_L - \omega_L \left\{ \sigma_{iso} + \frac{\zeta}{2}\left[(3\cos^2\theta - 1) + \eta \,\mathrm{sen}^2\theta \cos 2\phi \right] \right\}$$

Monocristal

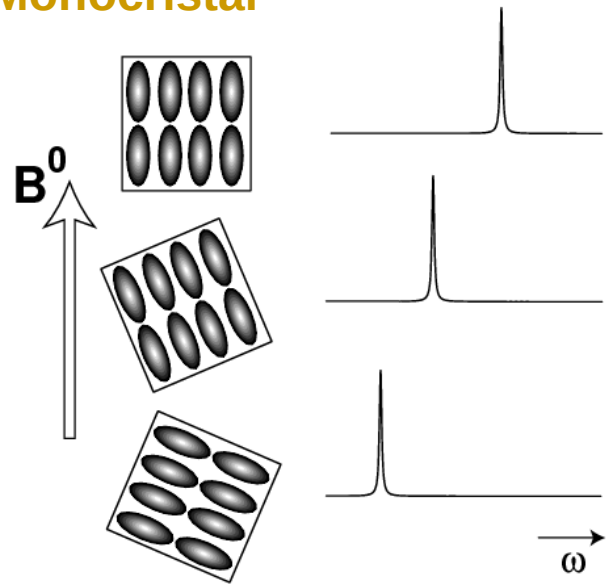

Sólido policristalino ou pó

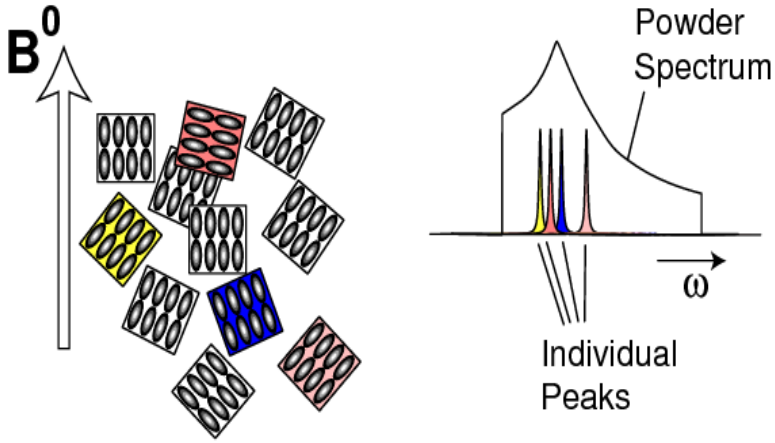

"Spin dynamics", M. H. Levitt. John Wiley & Sons, 2002.

Deslocamento químico em sólidos

Exemplos de espectros de pó:

Alargamento inomogêneo

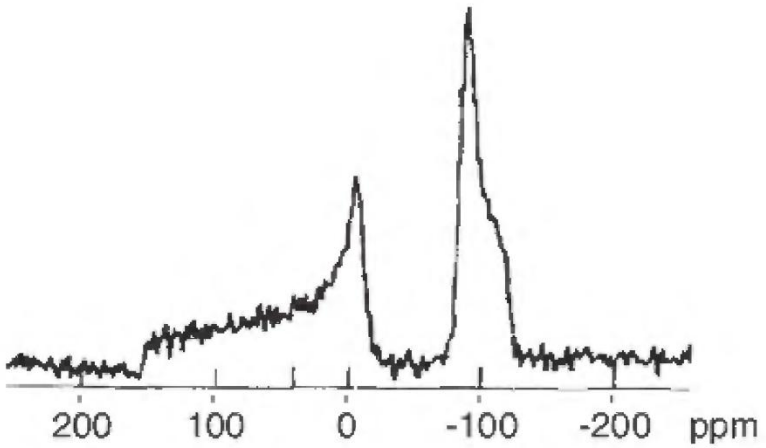

Figure 9.12 Experimental ^{1}H-decoupled ^{13}C spectrum for frozen acetic anhydride. The spectrum displays a powder pattern for each of the two chemically distinct ^{13}C sites. Both CSA tensors are almost uniaxial $\eta_j \cong 0$, but the sign and magnitude of the CSA are different. Reused from A. Pines, M. G. Gibby and J. S. Waugh, *J. Chem. Phys.* **59**, 569–590 (1973). Copyright 1973, American Institute of Physics.

"Spin dynamics", M. H. Levitt. John Wiley & Sons, 2002.

Interação dipolar internuclear

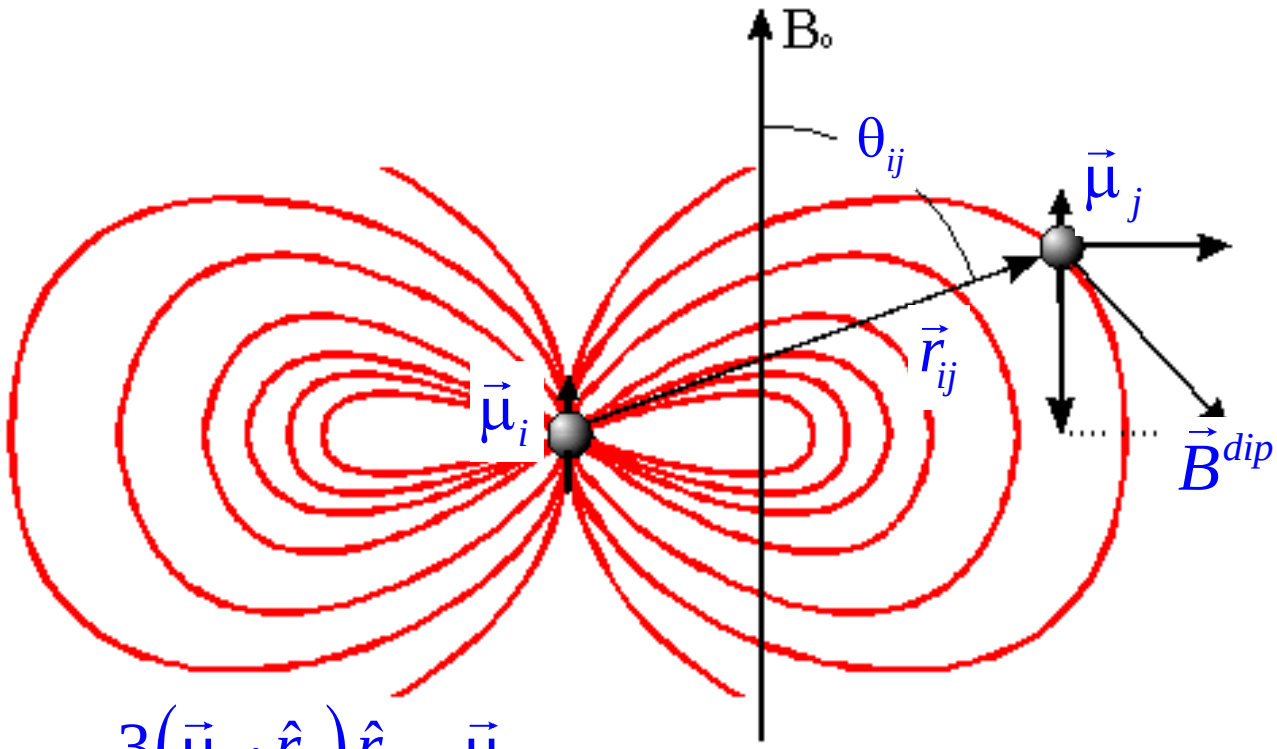

$$\vec{B}^{dip} = \frac{\mu_0}{4\pi} \frac{3\left(\vec{\mu}_i \cdot \hat{r}_{ij}\right)\hat{r}_{ij} - \vec{\mu}_i}{r_{ij}^3}$$

Interação através do espaço

Interação dipolar internuclear

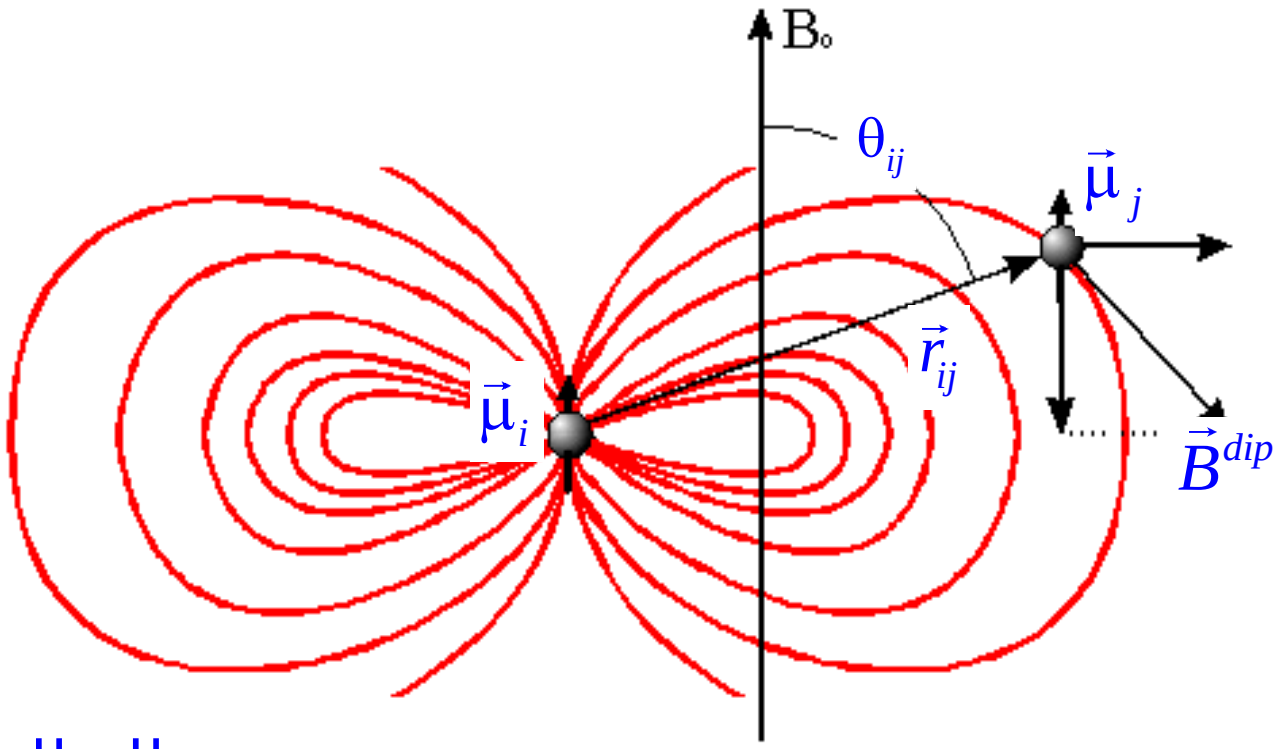

$$B_z^{dip} \cong \frac{\mu_0}{4\pi}\frac{\mu}{r_{ij}^3}(3\cos^2\theta_{ij} - 1)$$

Interação através do espaço

Interação dipolar internuclear

"Alfabeto" dipolar:

$$H_{dip} = -\vec{\mu} \cdot \vec{B}^{dip} = \frac{\mu_0}{4\pi} \gamma_I \gamma_S \hbar^2 \vec{I} \cdot \tilde{D} \cdot \vec{S}$$

$$H_{dip} = \frac{\mu_0}{4\pi} \frac{\gamma_I \gamma_S \hbar^2}{r^3} \left(A + B + C + D + E + F \right)$$

$$A = -I_z S_z (3\cos^2\theta - 1)$$

$$B = \tfrac{1}{4} (I_+ S_- + I_- S_+)(3\cos^2\theta - 1)$$

$$C = \tfrac{3}{2} (I_z S_+ + I_+ S_z) \operatorname{sen}\theta \cos\theta e^{-i\phi}$$

$$D = -\tfrac{3}{2} (I_z S_- + I_- S_z) \operatorname{sen}\theta \cos\theta e^{i\phi}$$

$$E = -\tfrac{3}{4} I_+ S_+ \operatorname{sen}^2\theta e^{-2i\phi}$$

$$E = -\tfrac{3}{4} I_- S_- \operatorname{sen}^2\theta e^{2i\phi}$$

Hamiltoniano secular – caso heteronuclear:

$$H_{dip}^{(sec)} = -\frac{\mu_0}{4\pi} \frac{\gamma_I \gamma_S \hbar^2}{r^3} I_z S_z (3\cos^2\theta - 1)$$

$$B_z^{dip} = \frac{\mu_0}{4\pi} \frac{\mu}{r_{ij}^3} (3\cos^2\theta - 1)$$

Constante de acoplamento dipolar:

$$d = \frac{\mu_0}{4\pi} \frac{\gamma_I \gamma_S \hbar}{r^3}$$

Interação dipolar em sólidos

Frequência dependente da orientação molecular (caso homonuclear):

$$\omega(\theta) = \omega_L \pm 3d\,\frac{3\cos^2\theta - 1}{4}$$

$$d = \frac{\mu_0}{4\pi}\,\frac{\gamma^2\hbar}{r^3}$$

Dubleto de Pake

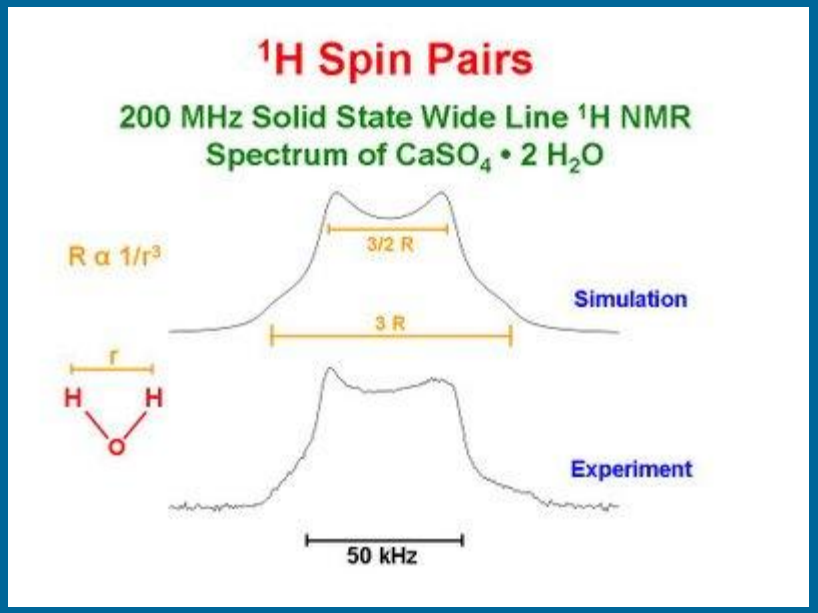

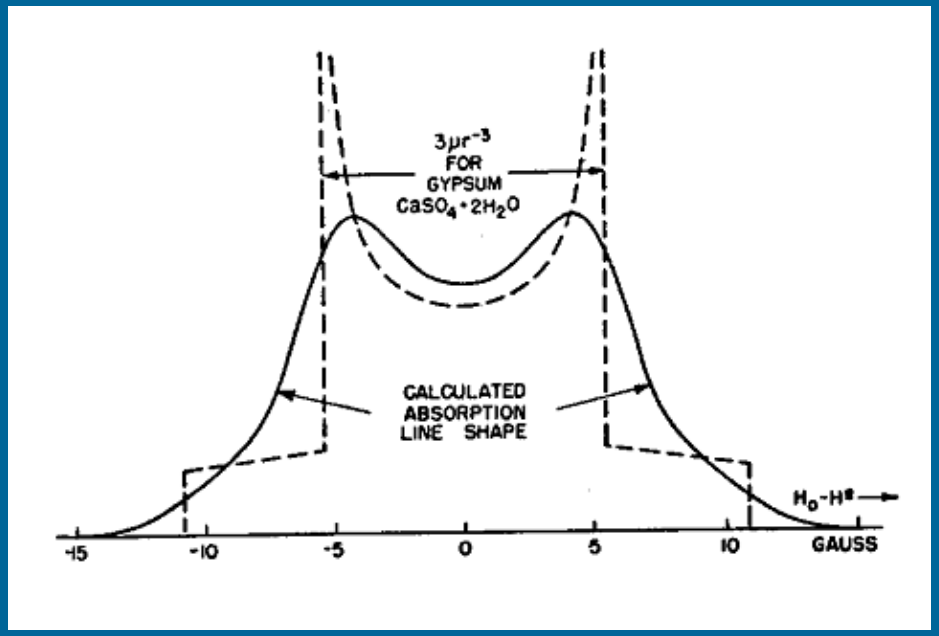

http://u-of-o-nmr-facility.blogspot.com/2008_10_01_archive.html

G. E. Pake, *J. Chem. Phys.* 1948;16:327-336.

Interação quadrupolar elétrica

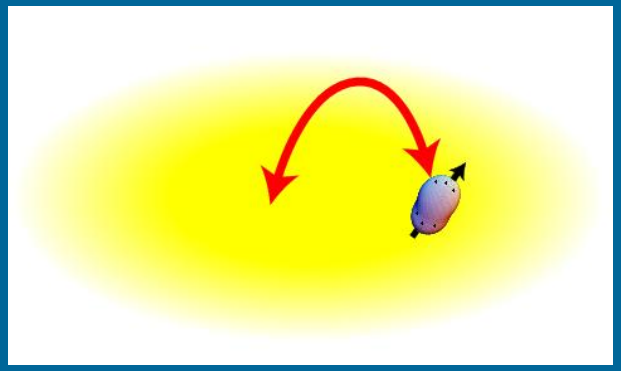

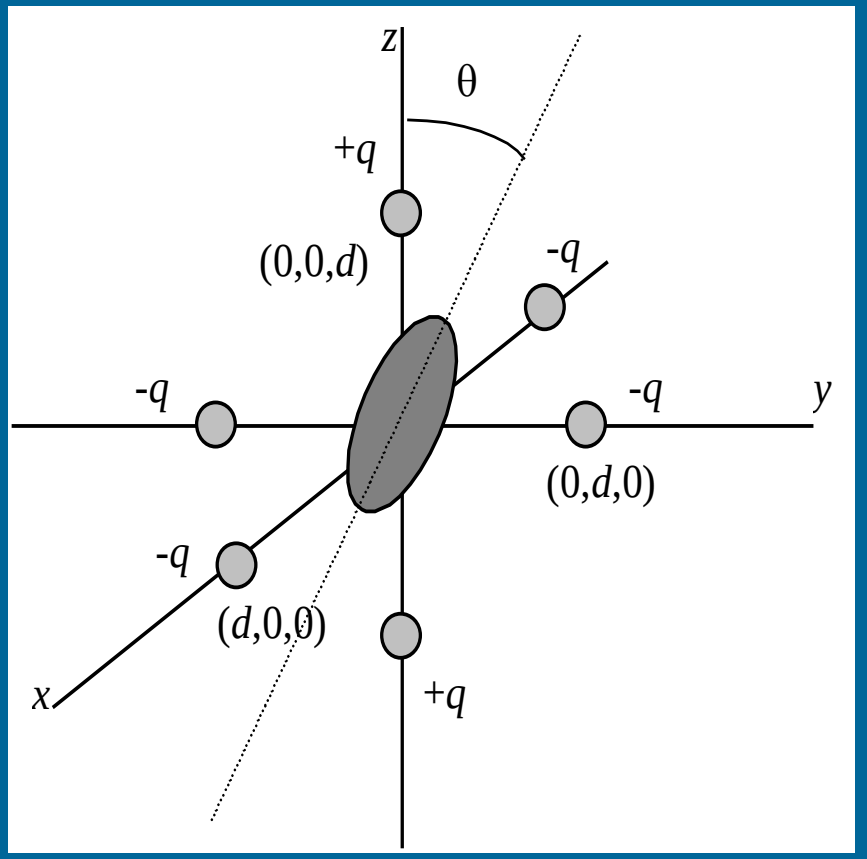

Núcleos quadrupolares (I > ½):
^{2}H, ^{23}Na, ^{25}Mg, ^{27}Al, ^{35}Cl, ^{55}Mn, ...

Gradiente de campo elétrico (EFG):

$$V_{\alpha\beta} = \left(\frac{\partial^2 V}{\partial x_\alpha \partial x_\beta}\right)_0$$

"Spin dynamics", M. H. Levitt. John Wiley & Sons, 2002.

Tensor gradiente de campo elétrico (EFG)

Sistema de laboratório:

$$\tilde{V}^{SLAB} = \begin{pmatrix} V_{xx} & V_{xy} & V_{xz} \\ V_{yx} & V_{yy} & V_{yz} \\ V_{zx} & V_{zy} & V_{zz} \end{pmatrix}$$

$$|V_{ZZ}| \geq |V_{YY}| \geq |V_{XX}|$$

Sistema de eixos principais:
(fixo com relação à molécula)

$$\tilde{V}^{SEP} = \begin{pmatrix} V_{XX} & 0 & 0 \\ 0 & V_{YY} & 0 \\ 0 & 0 & V_{ZZ} \end{pmatrix}$$

Contribuição isotrópica nula (equação de Laplace):

$$Tr(\tilde{V}) = V_{XX} + V_{YY} + V_{ZZ} = \nabla^2 V = 0$$

Anisotropia do EFG:

$$eq = V_{ZZ}$$

Parâmetro de assimetria:

$$\eta_Q = \frac{V_{XX} - V_{YY}}{V_{ZZ}}$$

$$0 \leq \eta \leq 1$$

Harris et al., *Pure Appl Chem.* 2008;80:59-84

Interação quadrupolar elétrica

Caso de simetria axial: $\eta_Q = 0$

$$\omega_Q = \frac{3e^2qQ}{2I(2I-1)\hbar}$$

Correções de primeira e segunda ordens na energia:

$$E_m^{(1)} = \frac{1}{4}\hbar\omega_Q(3\cos^2\theta - 1)\left[m^2 - \frac{1}{3}I(I+1)\right]$$

$$E_m^{(2)} = -\hbar\left(\frac{\omega_Q^{\,2}}{12\omega_L}\right)m\left\{\frac{3}{2}\cos^2\theta(1-\cos^2\theta)[8m^2 - 4I(I+1)+1] + \frac{3}{8}(1-\cos^2\theta)[-2m^2 + 2I(I+1) - 1]\right\}$$

Correções de primeira e segunda ordens nas frequências:

$$\omega_m^{(0)} = \omega_L$$

$$\omega_m^{(1)} = -\omega_Q\left(m - \frac{1}{2}\right)\frac{3\cos^2\theta - 1}{2}$$

$$\omega_{1/2}^{(2)} = -\frac{\omega_Q^{\,2}}{12\omega_L}\left[I(I+1) - \frac{3}{4}\right](1-\cos^2\theta)(9\cos^2\theta - 1)$$

Interação quadrupolar elétrica

Correções de primeira e segunda ordens – caso de simetria axial:

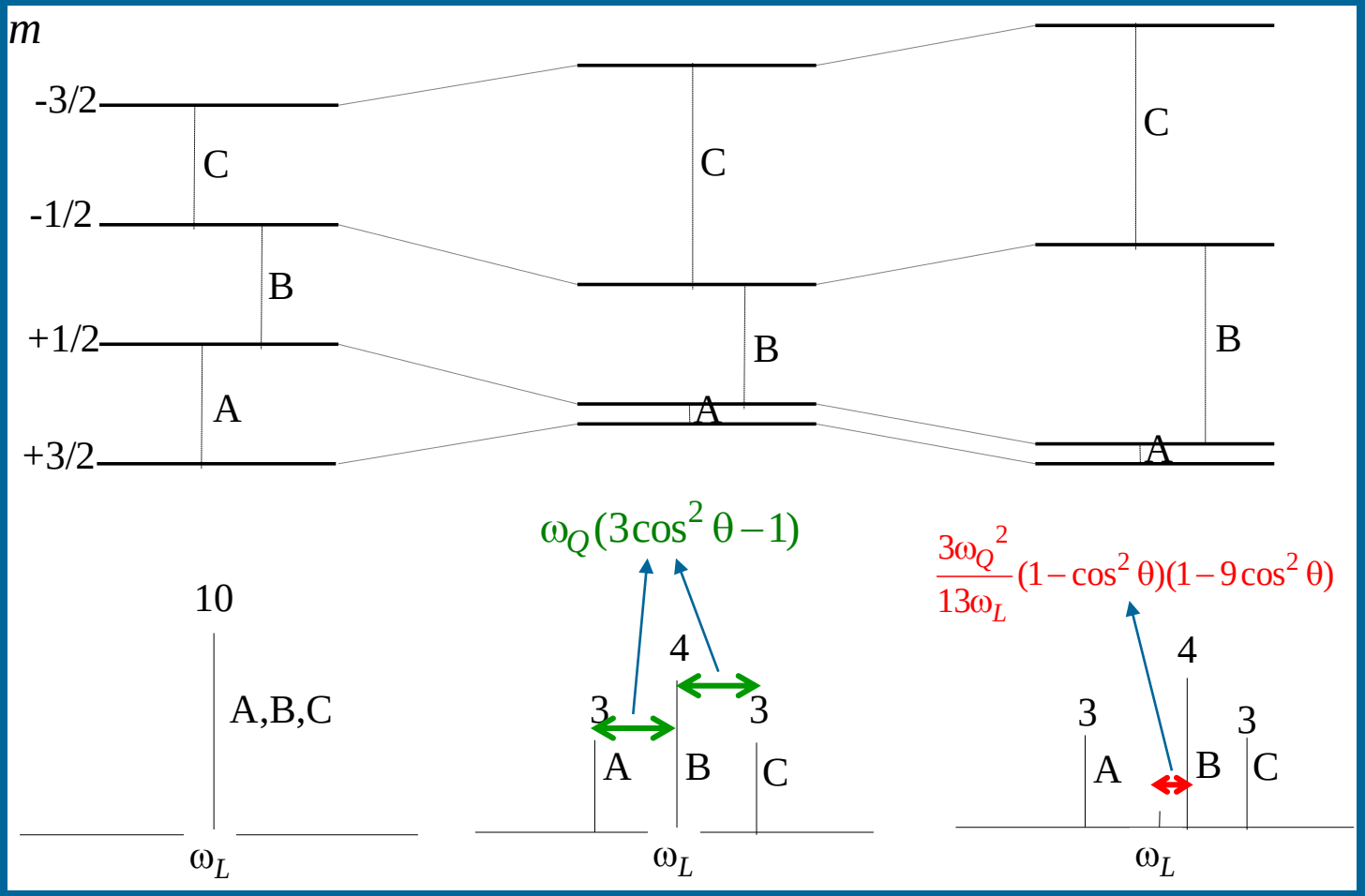

$I = 3/2$

$\eta_Q = 0$

Interação quadrupolar elétrica

Espectros de pó – núcleos com spin semi-inteiro:

Alargamento inomogêneo

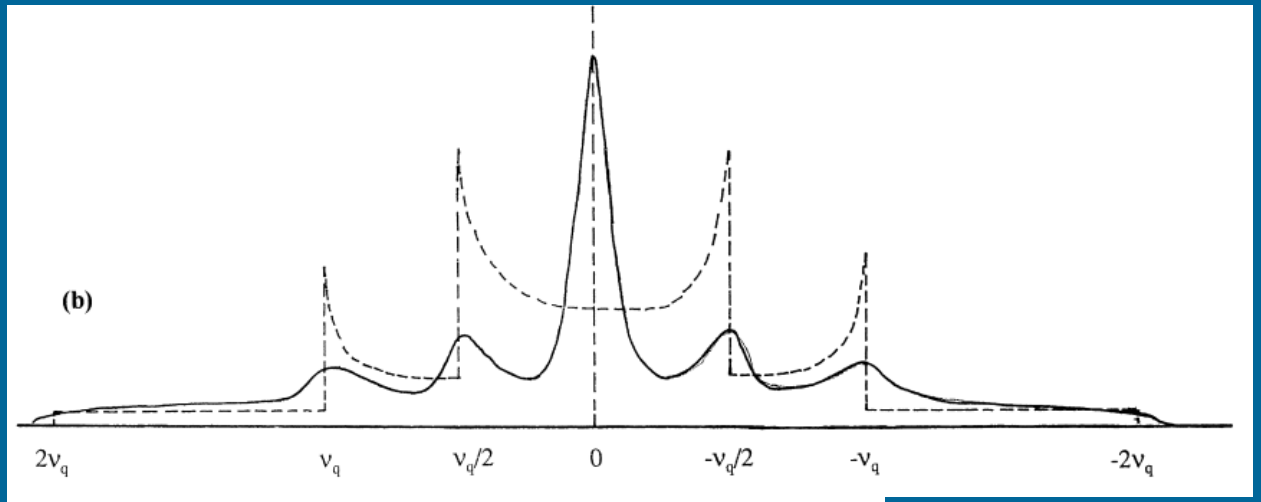

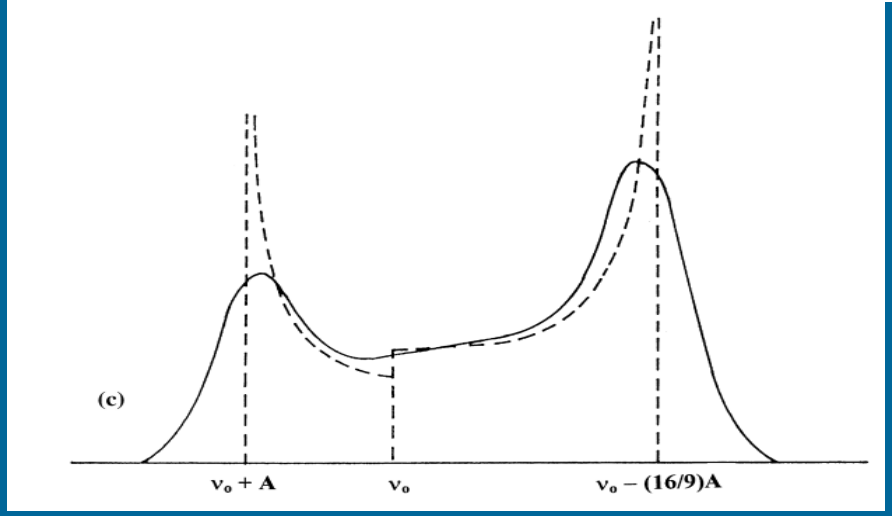

1ª ordem:

$$\nu_q = \frac{3e^2qQ}{2I(2I-1)h}$$

2ª ordem – transição central:

$$A = \left[I(I+1) - 3/4\right]\frac{\nu_q^{\,2}}{\nu_0}$$

Smith & van Eck, *Prog. Nucl. Magn. Reson. Spectr.* 1999;34:159-201

Interações de spin nuclear: resumo

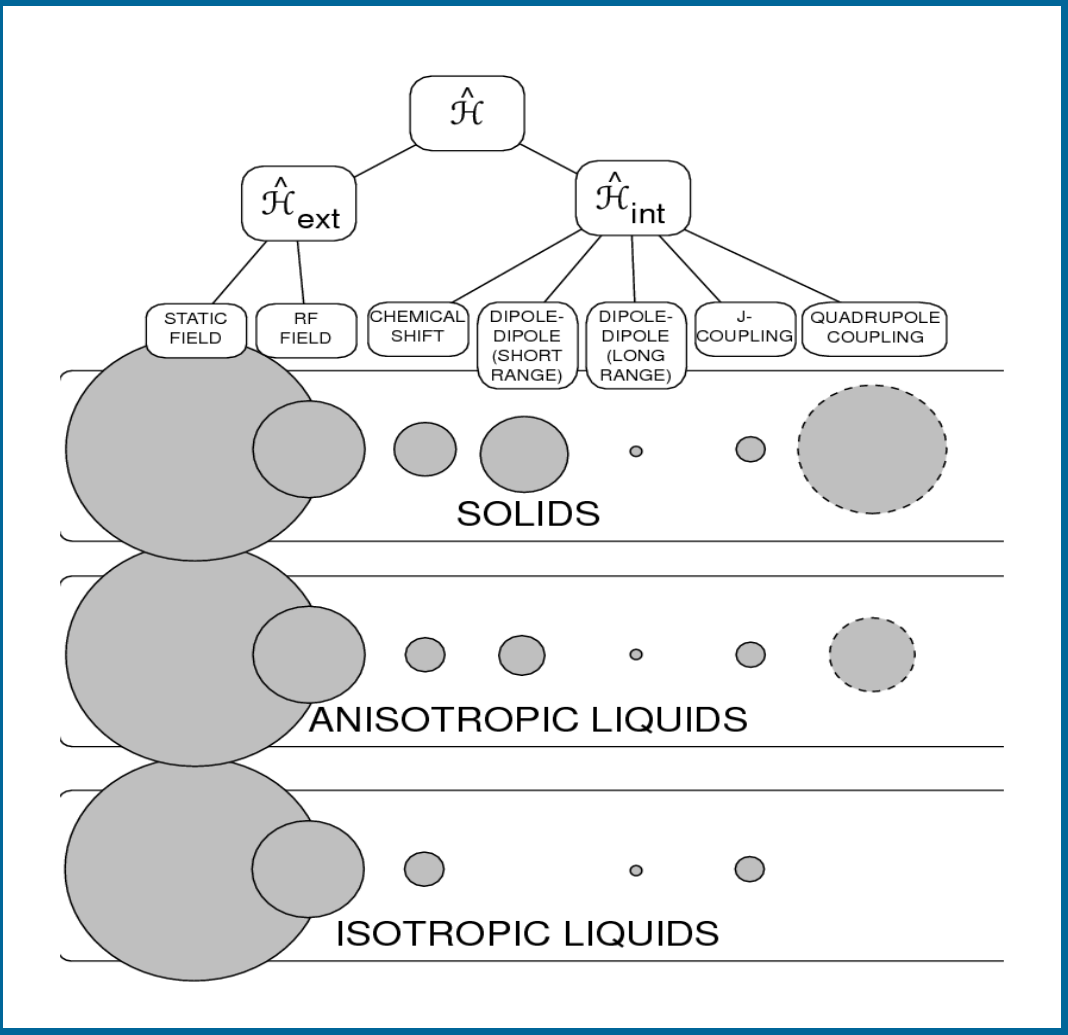

"Spin dynamics", M. H. Levitt. John Wiley & Sons, 2002.

Interações de spin nuclear: resumo

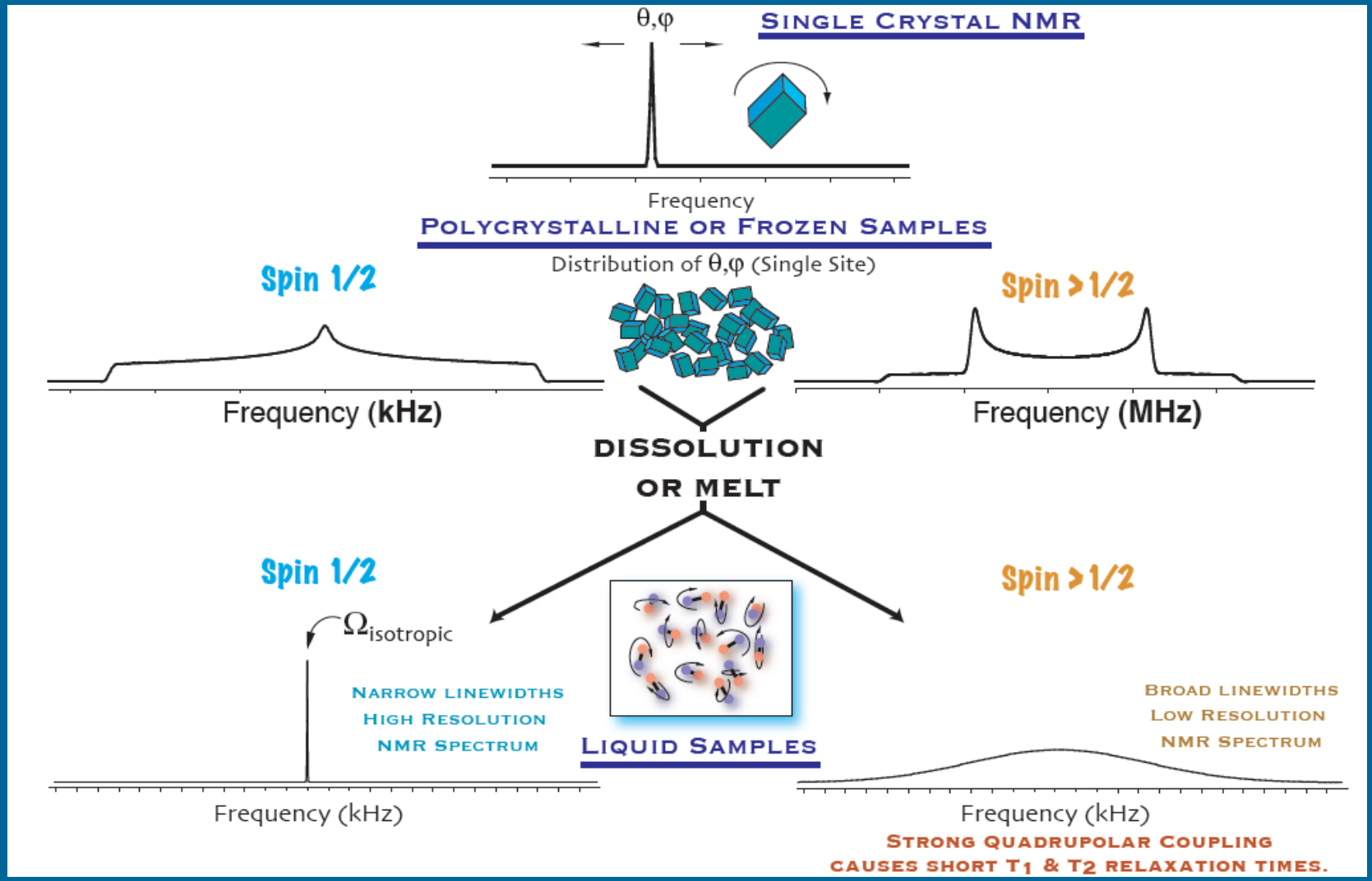

http://www.grandinetti.org/Research/NMR

RMN em sólidos policristalinos

- Alargamento inomogêneo: interações anisotrópicas.
- Algumas técnicas de alta resolução:
  - Desacoplamento dipolar .
  - Rotação em torno do ângulo mágico (MAS).
  - Polarização cruzada (CP).
- Objetivo: obtenção de espectros em sólidos com resolução similar à de líquidos, permitindo a medida de deslocamentos químicos isotrópicos.

Rotação em torno do ângulo mágico (MAS)

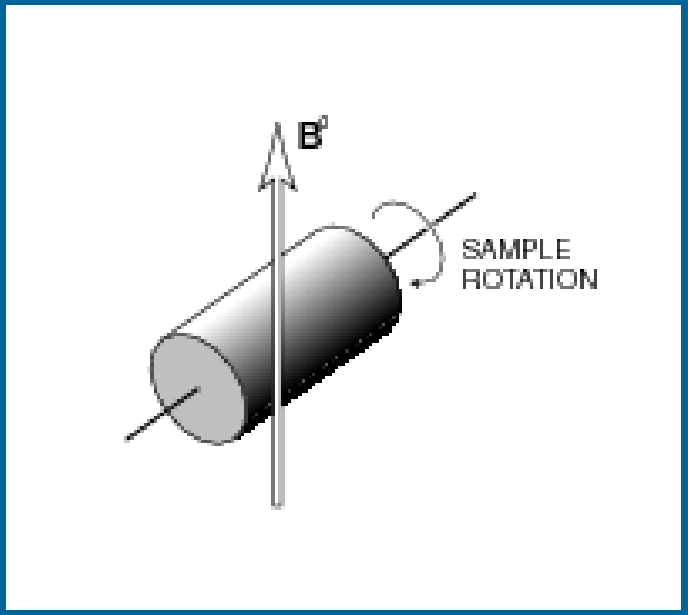

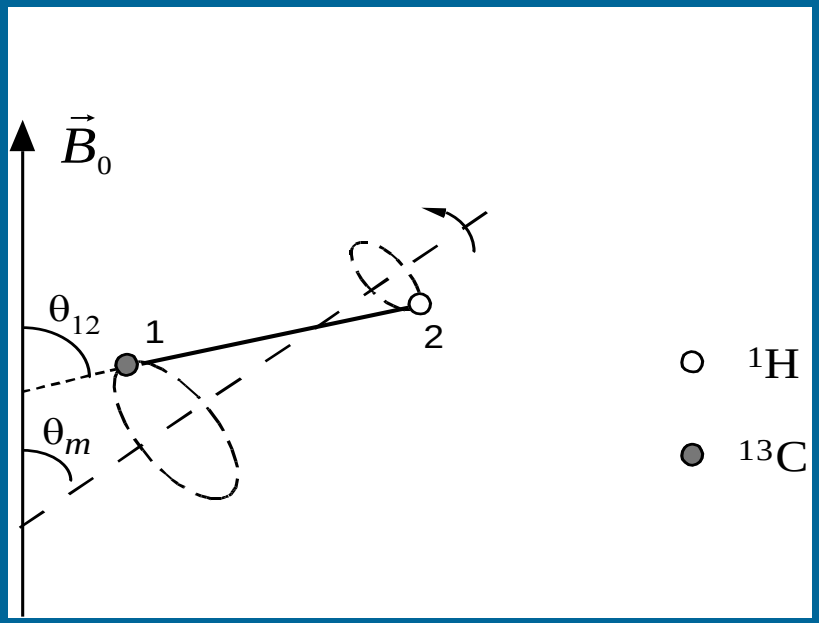

$$\left\langle 3\cos^2\theta_{12} - 1 \right\rangle \propto 3\cos^2\theta_m - 1 = 0$$

$$\theta_m = \cos^{-1}(1/\sqrt{3}) = 54{,}74^\circ$$

Andrew, *Nature* 1958;182:1659.
Lowe, *Phys. Rev. Lett.* 1959;2:285.

Rotação em torno do ângulo mágico (MAS)

RMN de ^{13}C (glicina)

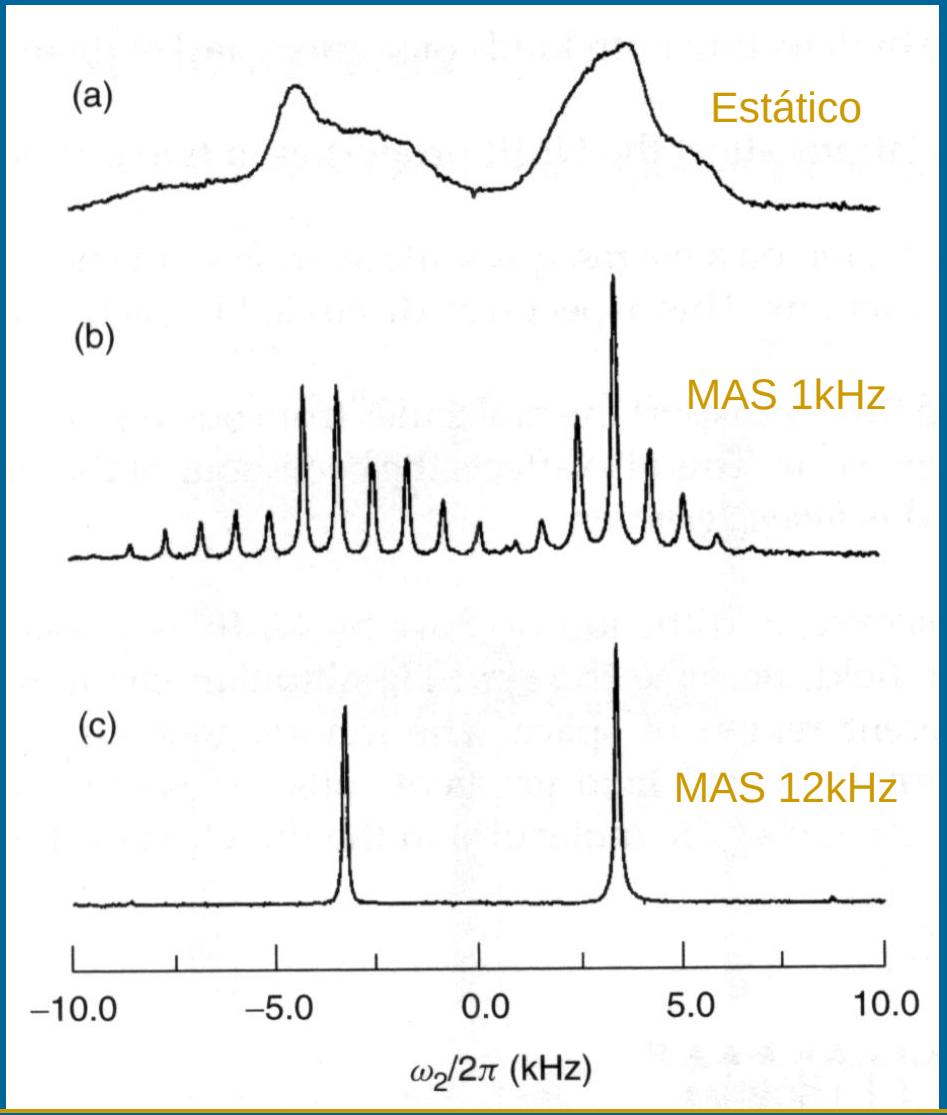

MAS e bandas laterais (ssb)

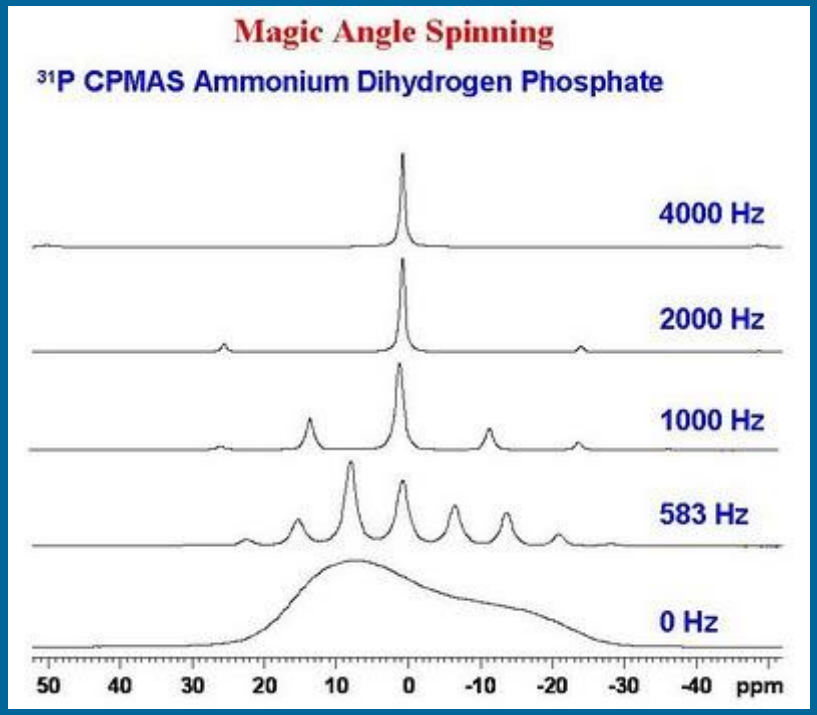

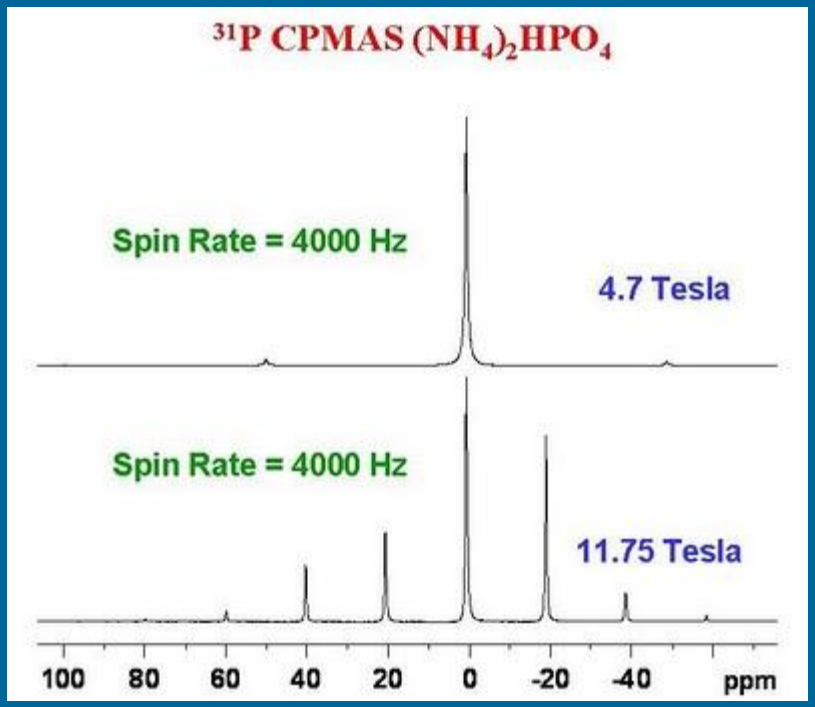

http://u-of-o-nmr-facility.blogspot.com/

Probes e rotores para experimentos com MAS

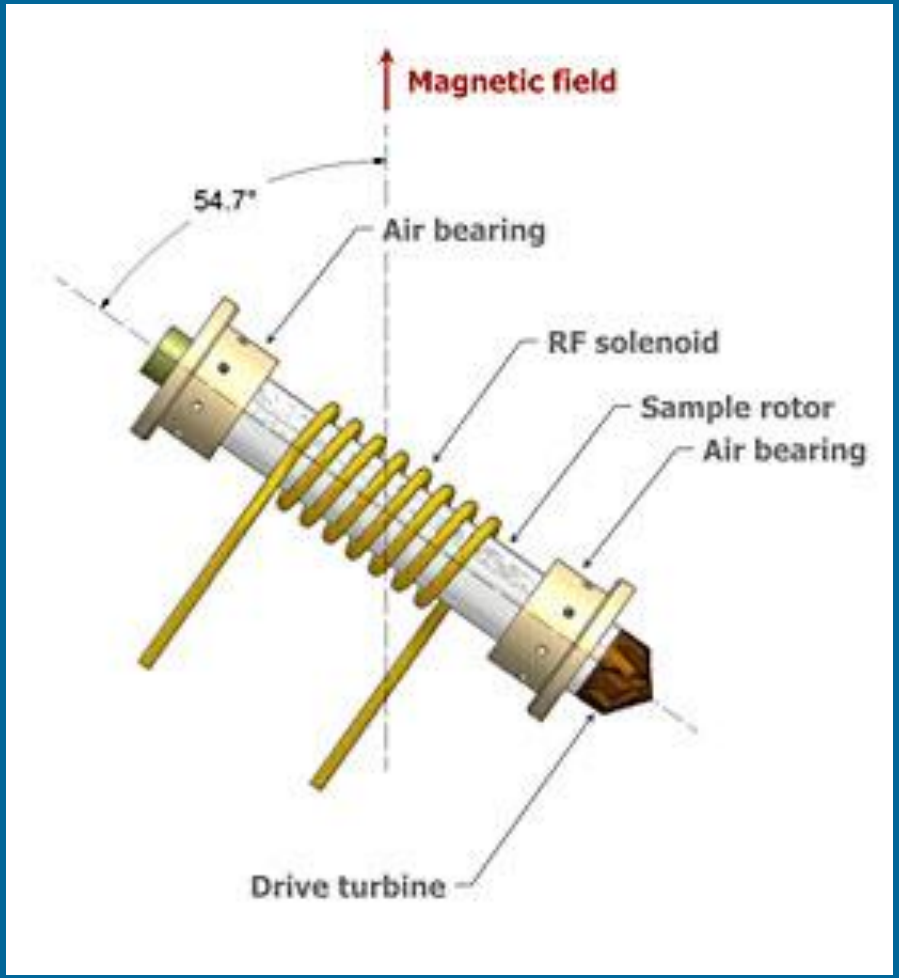

http://www.magnet.fsu.edu/education/tutorials/tools/probes/magicangle.html

Probes e rotores para experimentos com MAS

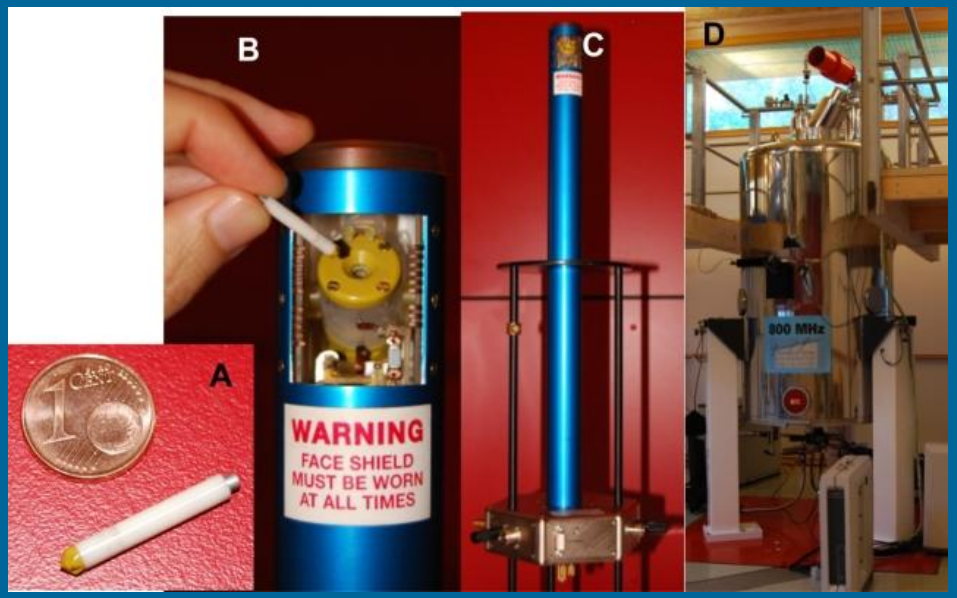

- Rotores menores:
  - ✓ Frequências de MAS maiores.
    - 7mm: f_{MAS} < 8 kHz.
    - 2,5mm: f_{MAS} < 35 kHz.
  - ✓ Menor sensibilidade.

Probes e rotores para experimentos com MAS

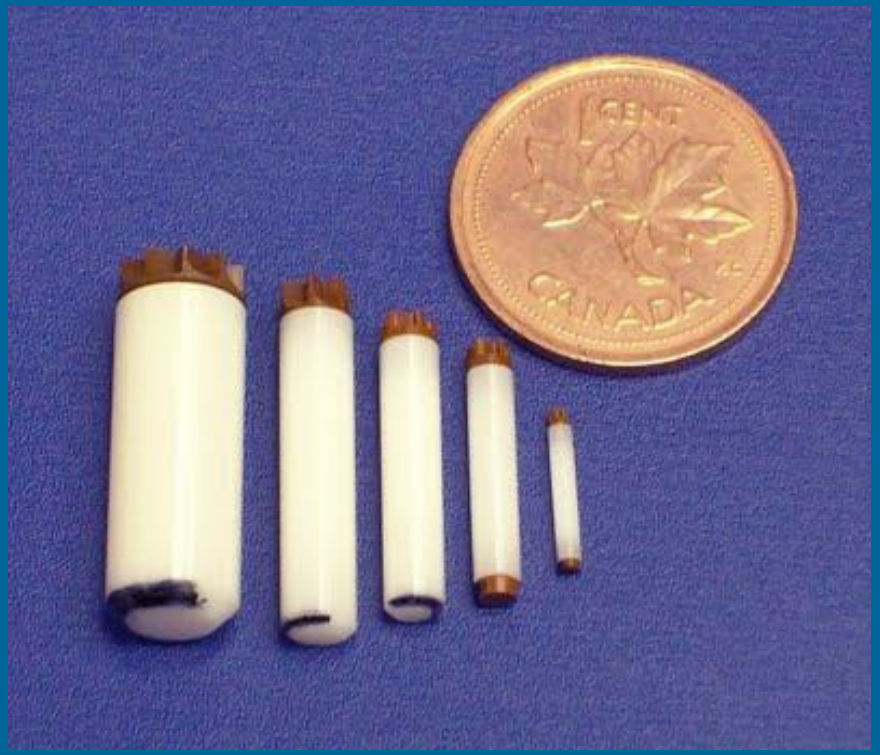

ϕ (mm): 7,0 4,0 3,2 2,5 1,3

$\nu_{rot}^{máx.}$ (kHz): 8 18 23 35 70

http://u-of-o-nmr-facility.blogspot.com/2008/04/how-much-sample-do-i-need-to-get-solid.html

Desacoplamento dipolar heteronuclear

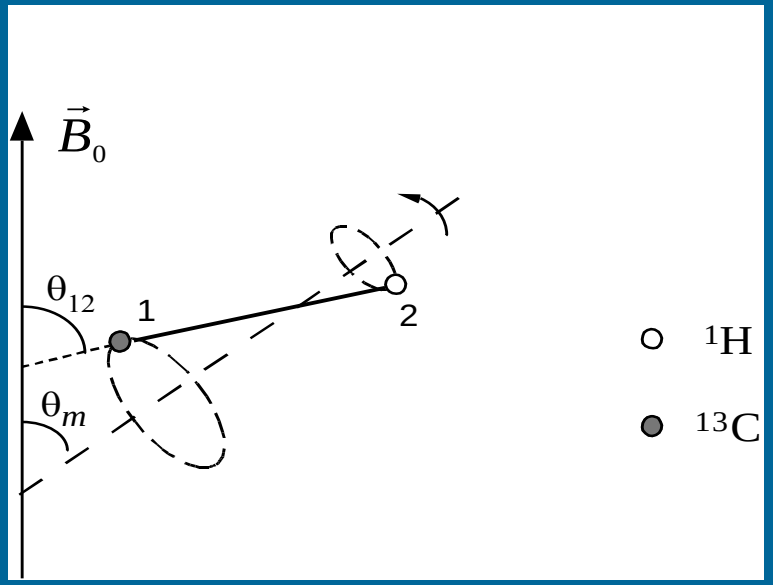

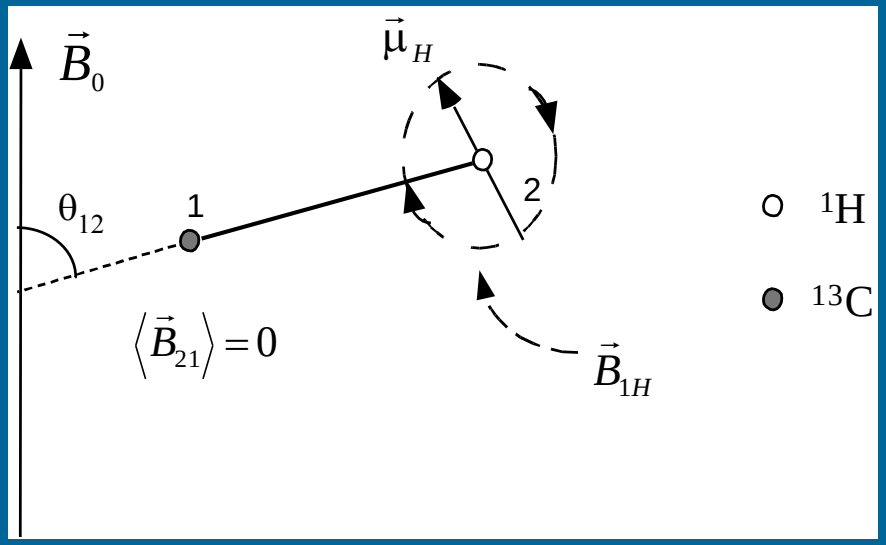

Ressonância dupla:

- Excitação de ^{1}H (f_{1H}) e de ^{13}C (f_{13C}).
- Detecção de ^{13}C (f_{13C}).

Desacoplamento dipolar heteronuclear

Eficiência do desacoplamento:

$$\gamma_H B_{1H} / 2\pi > \Delta f_{dip}$$

$$\Delta f_{dip} \sim d = \frac{\mu_0}{8\pi^2} \frac{\gamma_I \gamma_S \hbar}{r^3}$$

(alargamento devido ao acoplamento dipolar)

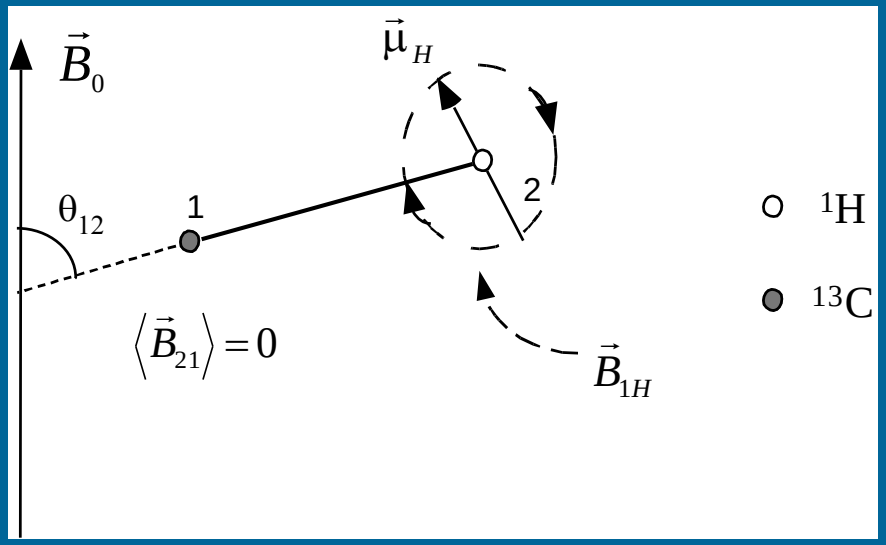

Par ^{1}H-^{13}C em grupo CH (ligação simples):

$$\Delta f_{dip} \sim 70 \text{ kHz}$$

Desacoplamento dipolar heteronuclear

Probe de ressonância dupla

Desacoplamento dipolar heteronuclear

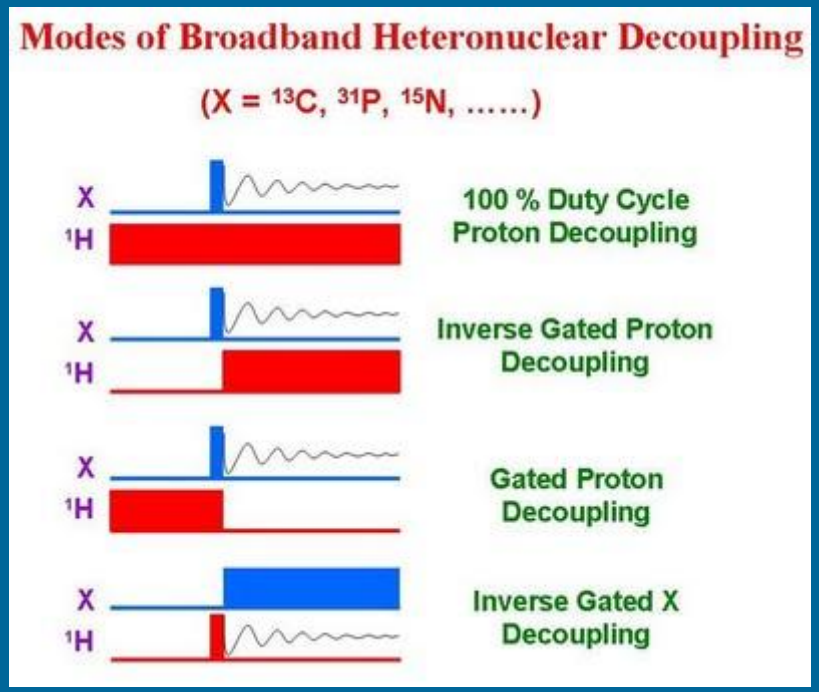

Espectros de RMN de ^{13}C com desacoplamento de ^{1}H:

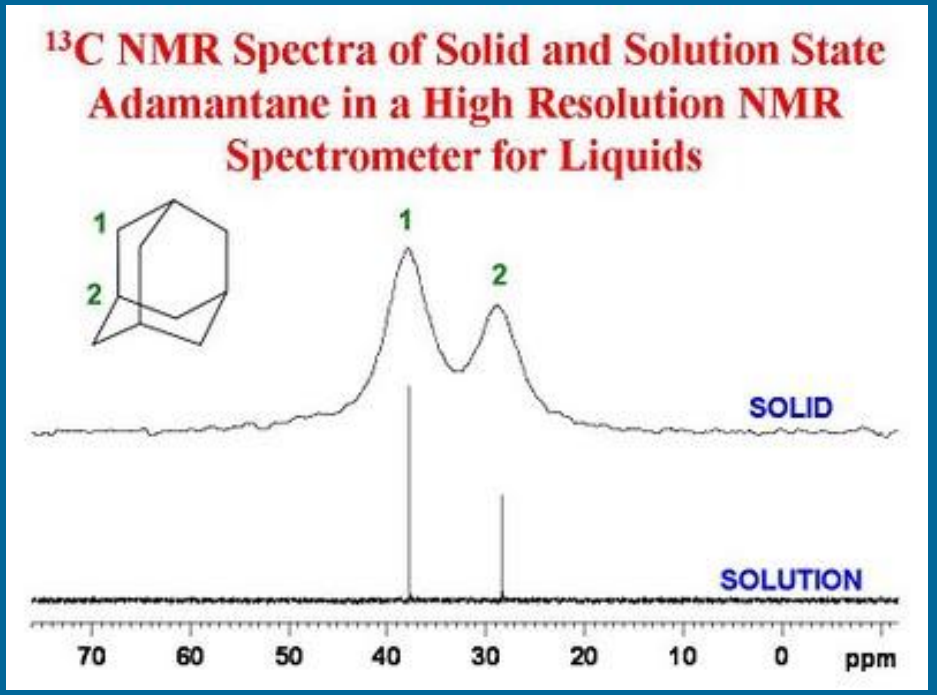

http://u-of-o-nmr-facility.blogspot.com/

MAS e desacoplamento dipolar homonuclear

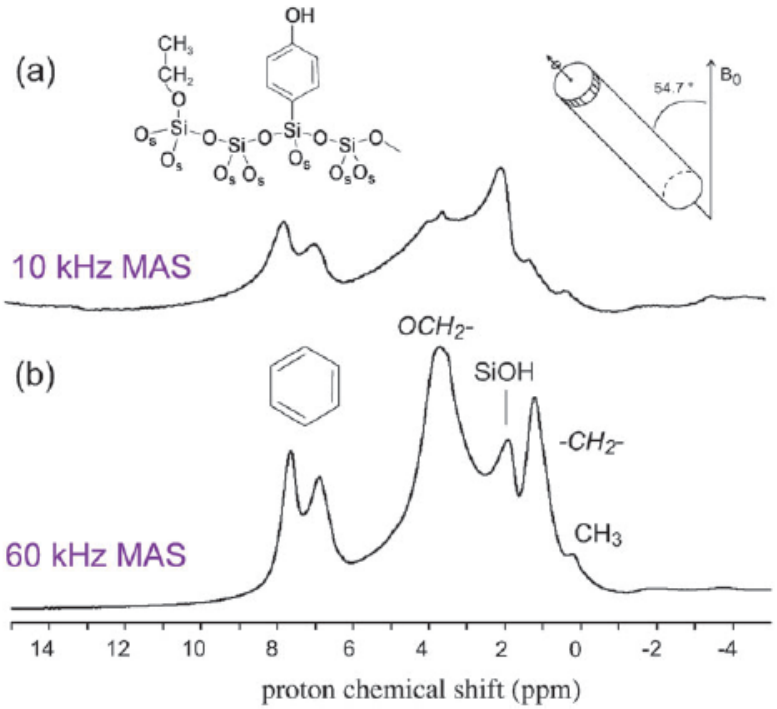

Fig. 1 One-dimensional ^{1}H spectra of an organic compound grafted inside the mesopores of a silica matrix, at 10 kHz (a) and 60 kHz MAS frequencies (resonances corresponding to surfactant chains are also observed). A total of 64 transients were recorded at a ^{1}H frequency of 900 MHz. The spectra were recorded using a 1.3 mm CPMAS probe (sample volume of 2 µL) on a Bruker Avance III spectrometer. (In collaboration with Dr C. Copéret and D. Gajan.)

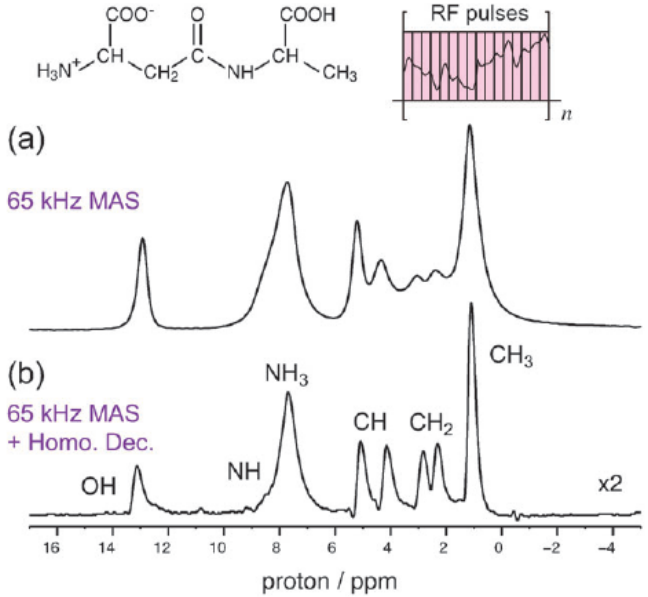

Fig. 2 One-dimensional ^{1}H spectra of the dipeptide b-L-Asp-L-Ala under MAS at 65 kHz. (a) MAS spectrum (2 transients). (b) Homonuclear-decoupled spectrum using the windowed eDUMBO-1_{22} sequence during direct acquisition (16 transients). eDUMBO-1_{22} was implemented with an RF pulse amplitude of 170 kHz. The homonuclear-decoupled spectrum shows a highly linear scaling factor (0.58) across the entire ^{1}H chemical shift range (as evaluated from the comparison between the decoupled and the MAS-only spectra). We note that windowed decoupling during acquisition compromises the overall spectral sensitivity. Reprinted from *Chem. Phys. Lett.*, 2009, **469**, E. Salager, R. S. Stein, S. Steuernagel, A. Lesage, B. Elena and L. Emsley. Enhanced sensitivity in high-resolution ^{1}H solid-state NMR spectroscopy with DUMBO dipolar decoupling under ultra-fast MAS, 336–341. Copyright 2009, with permission from Elsevier.[27]

Lesage, Phys. Chem. Chem. Phys. 2009;11:6876-6891

Polarização cruzada (CP)

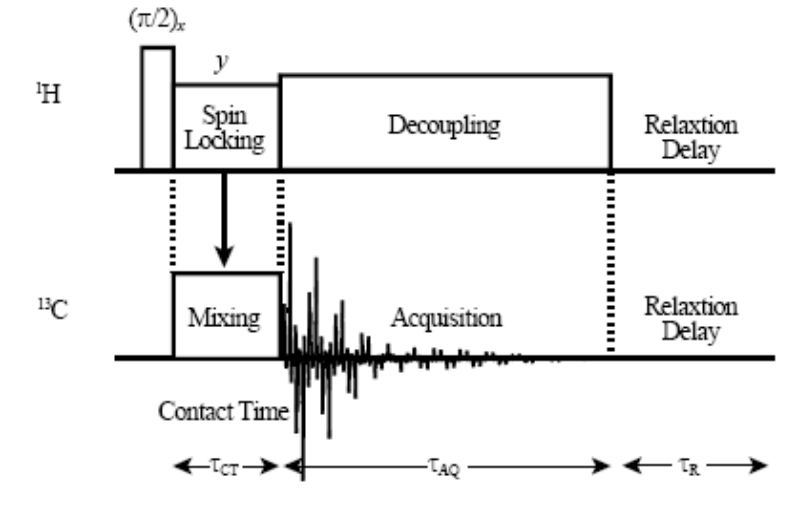

Ressonância dupla:

- Excitação de ^{1}H (f_{1H}) e de ^{13}C (f_{13C}).
- Detecção de ^{13}C (f_{13C}).
- Aumento do sinal de ^{13}C por um fator de no máximo $\gamma(^1H) / \gamma(^{13}C) \sim 4$ (por "contato").
- Redução no tempo de repetição: $T_1(^1H) < T_1(^{13}C)$.
- Detecção seletiva de grupos hidrogenados ("edição de espectros").

Polarização cruzada (CP)

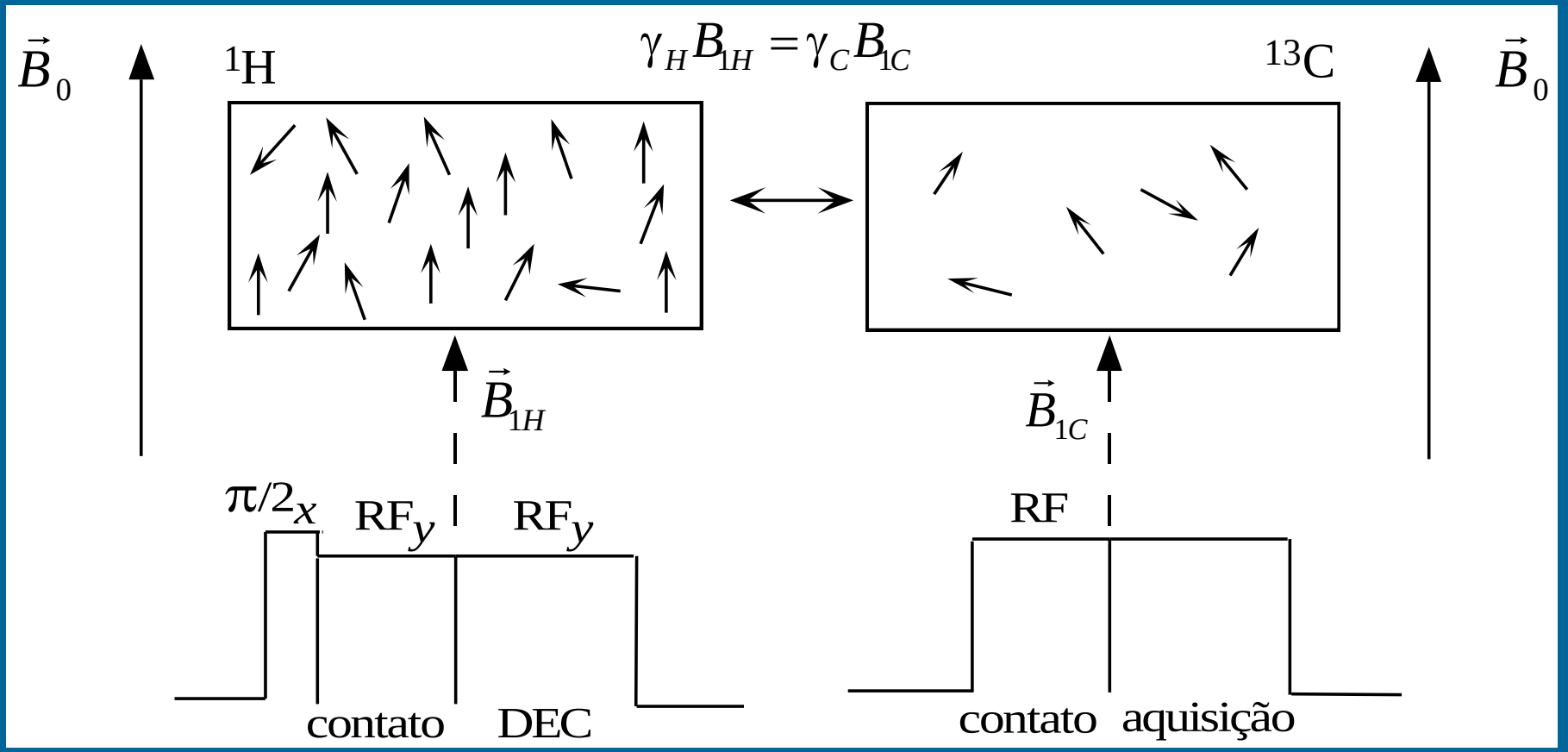

Travamento de spins
(“spin-locking”)

Experimento CP/MAS

Espectroscopia de alta resolução em sólidos por RMN:

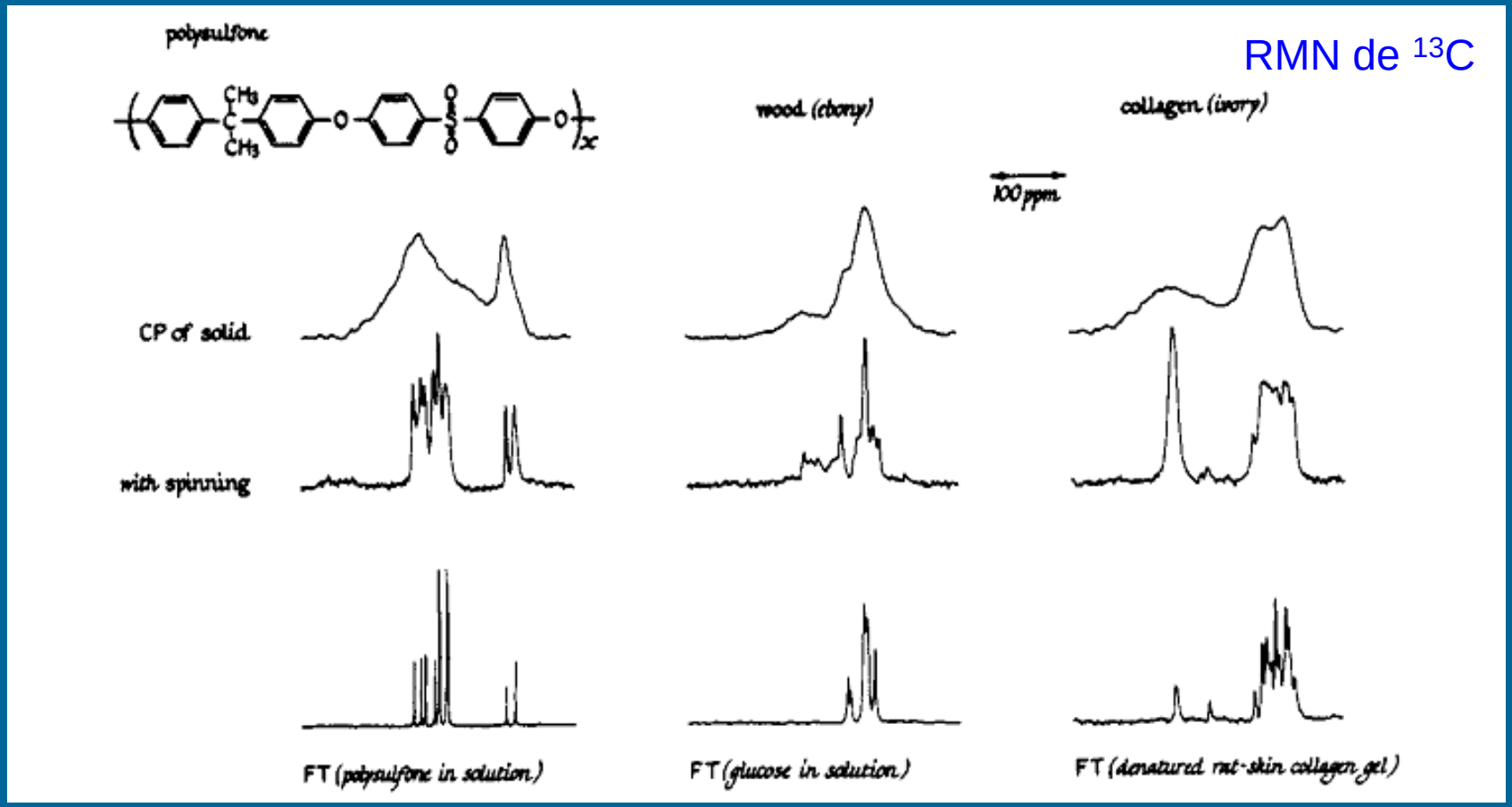

Schaefer & Stejskal, *J. Am. Chem. Soc.* 1976;98:1031

Métodos de RMN 2D em sólidos

Correlação heteronuclear (HETCOR):

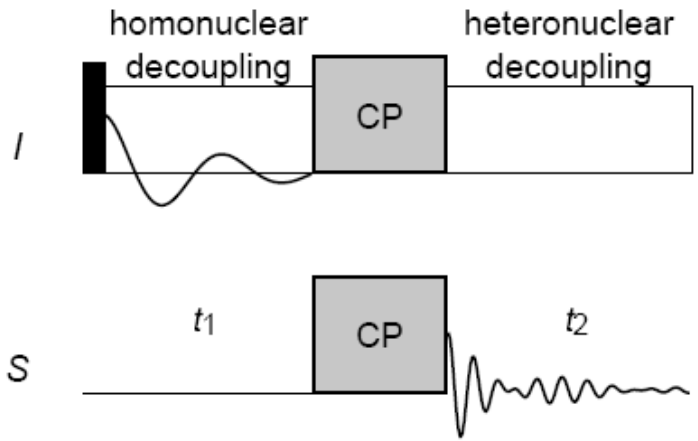

Figure 17. Principle of the HETCOR experiment: The pulse sequence is identical to that of the WISE experiment, except for the incorporation of homonuclear dipolar decoupling in the indirect dimension. Heteronuclear decoupling of the *S* spins can also be incorporated into the indirect dimension.

WISE = “wideline separation”

Jerschow et al., Angew Chem. Int. Ed. 2002;41:3096.

Sumário

- RMN em meios porosos:
  - Contraste de suscetibilidade magnética.
  - Relaxometria por RMN de ^{1}H
    - Aplicações em petrofísica.
  - Utilização de métodos de RMN de sólidos.
  - Materiais micro e mesoporosos:
    - Materiais de carbono.
    - Silicatos.
    - Estruturas metal-orgânicas (MOFs).

Contraste de suscetibilidade magnética em meios porosos

Using Internal Magnetic Fields to Obtain Pore Size Distributions of Porous Media

YI-QIAO SONG

Schlumberger-Doll Research, Old Quarry Road, Ridgefield, CT 06877

BIOGRAPHY

Yi-Qiao Song received his B.S. degree from Peking University, Beijing, China, in 1985 and Ph.D. degree in physics from Northwestern University, Evanston, IL, in 1991. He was a Miller Research Fellow at University of California, Berkeley, where he studied highly polarized xenon for nuclear magnetic resonance and magnetic resonance imaging. In 1997, he joined Schlumberger-Doll Research, Ridgefield, CT, to investigate applications of NMR technologies to the study of porous media and well logging.

Y.-Q. Song, *Concepts Magn. Reson.* 2003;18A:97-110.

Contraste de suscetibilidade magnética em meios porosos

Linhas de indução – dipolo magnético:

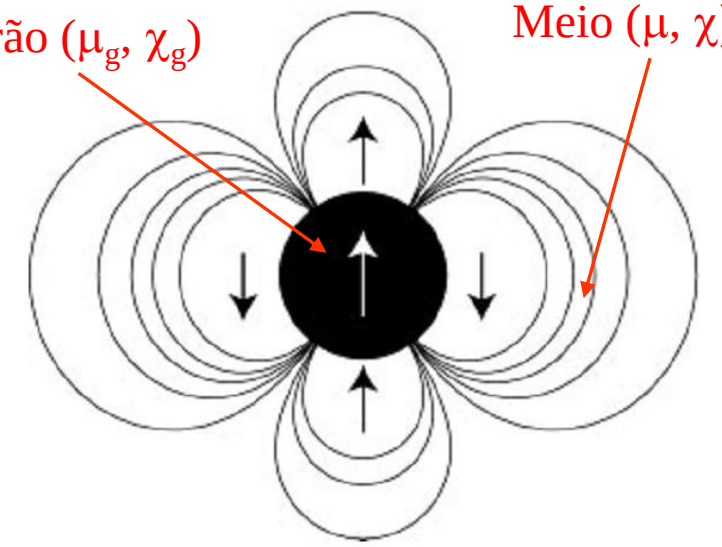

Figure 1 Contour lines of the magnetic field (z-component) from a dipole (solid circle). The external field is applied vertically. The arrow within the solid circle marks the direction of the moment and the other arrows mark the direction of the field.

$$\mathbf{B}^i(\mathbf{r}) = \frac{3(\mathbf{m}\cdot\mathbf{r})\mathbf{r} - |\mathbf{r}|^2\mathbf{m}}{|\mathbf{r}|^5}$$

$$\mathbf{m} = \frac{\mu_g - \mu}{\mu_g + 2\mu} R^3 \mathbf{B}_0$$

$$\mu_g = 1 + 4\pi\chi_g$$

$$\mu = 1 + 4\pi\chi$$

$$(\mu_g - \mu)/4\pi = \chi_g - \chi \equiv \delta\chi$$

Contraste de suscetibilidade magnética

Y.-Q. Song, *Concepts Magn. Reson.* 2003;18A:97-110.

Contraste de suscetibilidade magnética em meios porosos

Linhas de indução – dipolo magnético:

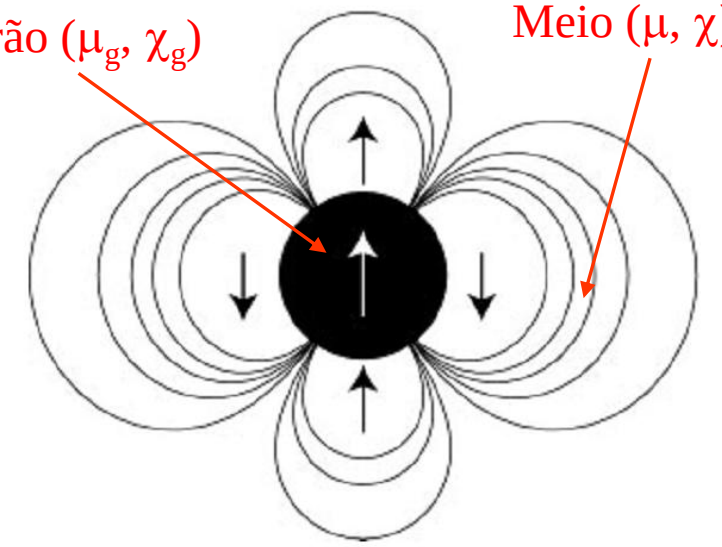

Figure 1 Contour lines of the magnetic field (z-component) from a dipole (solid circle). The external field is applied vertically. The arrow within the solid circle marks the direction of the moment and the other arrows mark the direction of the field.

$$\mathbf{m} = \frac{\mu_g - \mu}{\mu_g + 2\mu} R^3 \mathbf{B}_0$$

$$\mathbf{B}^i(\mathbf{r}) = \frac{3(\mathbf{m}\cdot\mathbf{r})\mathbf{r} - |\mathbf{r}|^2\mathbf{m}}{|\mathbf{r}|^5}$$

$$B_z^i = [3\cos^2(\theta) - 1]/|\mathbf{r}|^3$$

$$B_z^i = \sum_k B_z^i(\mathbf{r} - \mathbf{r}_k)$$

$$\Delta B_z^i \propto \delta\chi B_0$$

Y.-Q. Song, *Concepts Magn. Reson.* 2003;18A:97-110.

Contraste de suscetibilidade magnética em meios porosos

Distribuição de campo magnético (simulação):

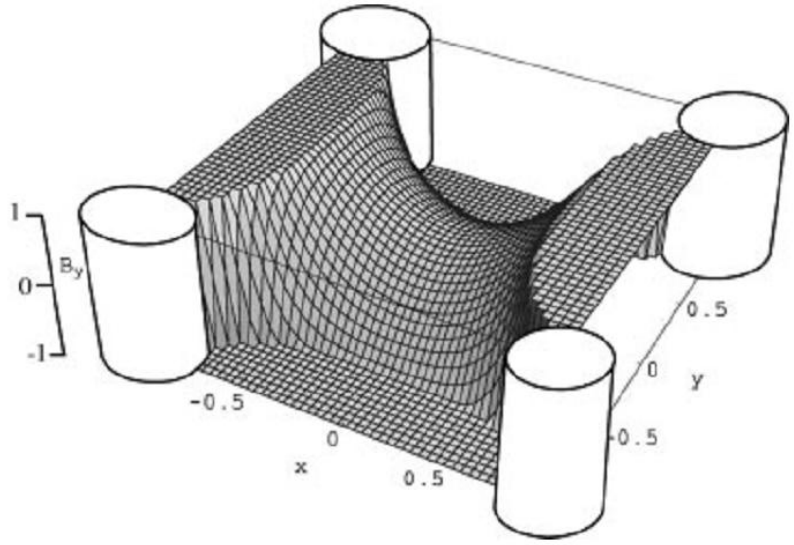

Figure 2 Internal field arising from a discrete sum over cylinders for a square array of cylinders polarized along the y axis. The center of the pore is at the origin. The plot's range of field values is restricted between ±1 for purposes of display. Remember that there are cylinders at the points (1, 1), (1, −1), (−1, 1), and (−1, −1). Modified from Ref. (*12*) with permission.

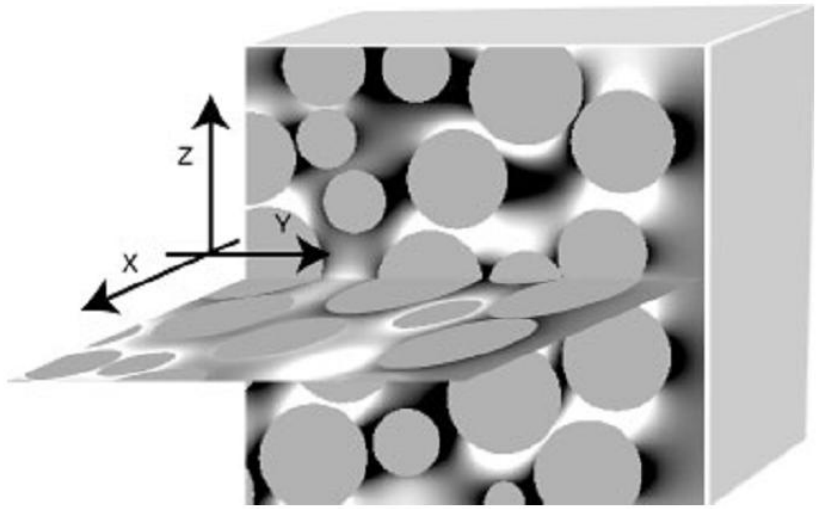

Figure 3 Internal field (z-component) in a random packing of spheres, shown along two section planes (XY and YZ). The circular and elliptical objects are the sections of the spheres and their sizes are dependent on the position of the sectioning plane to the individual spheres. The internal field is shown as the gray scale from minimum to maximum values. The external field is applied vertically.

Y.-Q. Song, *Concepts Magn. Reson.* 2003;18A:97-110.

Contraste de suscetibilidade magnética em meios porosos

Distribuição de campo magnético (simulação):

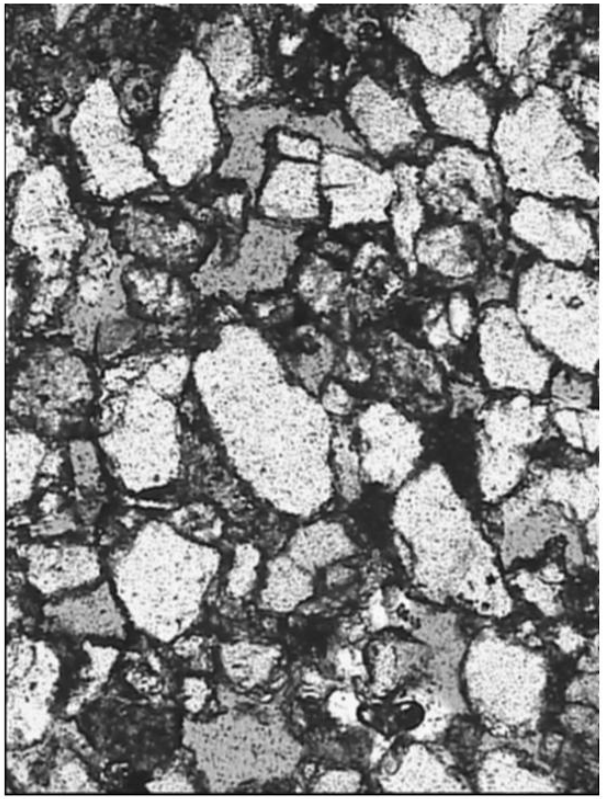

Fig. 1. An optical micrograph of a Berea sandstone thin-section, with a field of view (FOV) of 921 μm × 1228 μm. The white regions are large quartz crystals, while dark regions are small crystals and clay. The gray regions are pore space identified by the dye color of an impregnated resin.

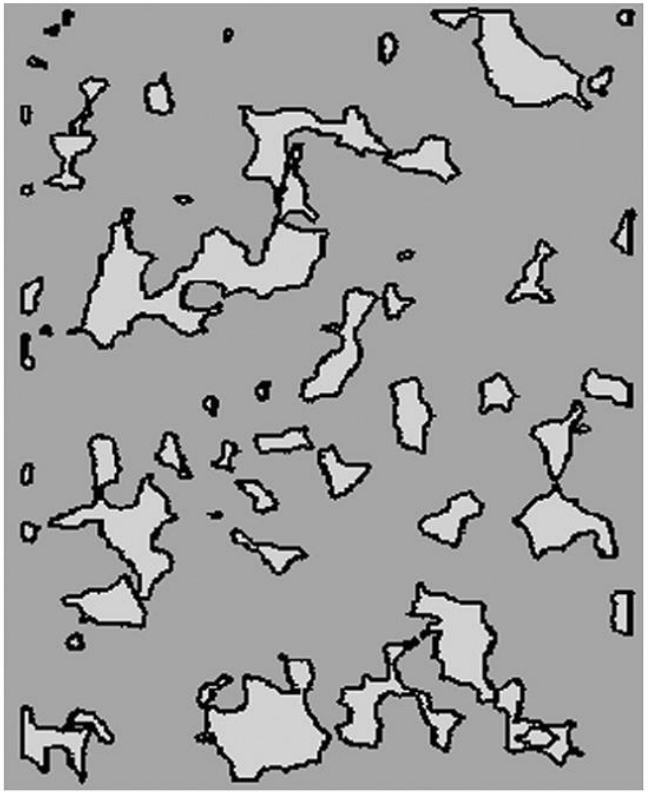

Fig. 2. A 2D simulation model for a 100% water saturated Berea sandstone, which was extracted from the thin-section images. FOV, 921 μm × 1228 μm. Gray and white represent solid matrix and water, respectively.

Chen et al., *J. Magn. Reson.* 2005;175:300-308.

Contraste de suscetibilidade magnética em meios porosos

Distribuição de campo magnético (simulação):

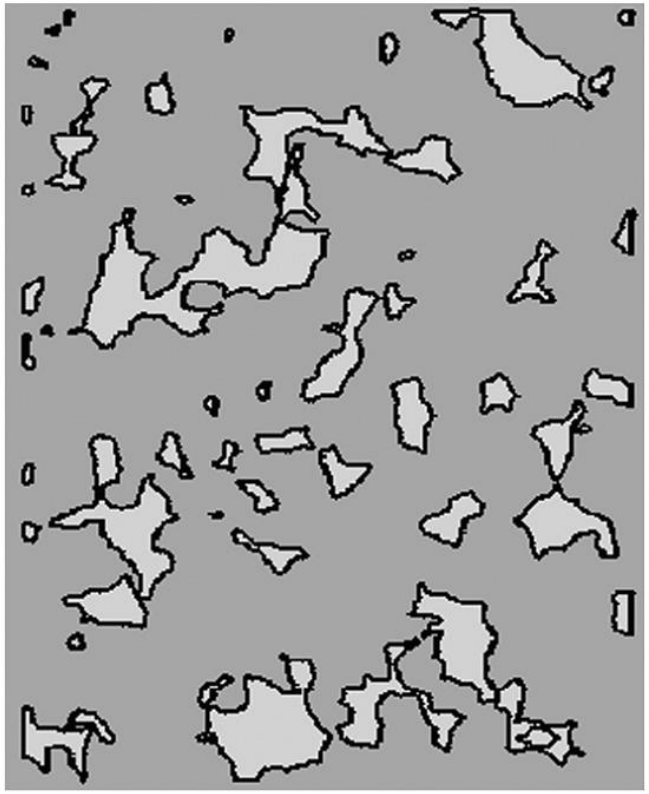

Fig. 2. A 2D simulation model for a 100% water saturated Berea sandstone, which was extracted from the thin-section images. FOV, 921 μm × 1228 μm. Gray and white represent solid matrix and water, respectively.

$$\nabla \bullet \vec{B} = 0, \qquad \nabla \times \vec{H} = 0,$$

$$\vec{B} = \mu_0 (1 + \chi(x, y))\vec{H},$$

$\chi = 89,85 \times 10^{-6}$ (arenito)

$\chi = -9,05 \times 10^{-6}$ (água)

$\chi = 0,36 \times 10^{-6}$ (ar)

Chen et al., *J. Magn. Reson.* 2005;175:300-308.

Contraste de suscetibilidade magnética em meios porosos

Distribuição de campo magnético (simulação):

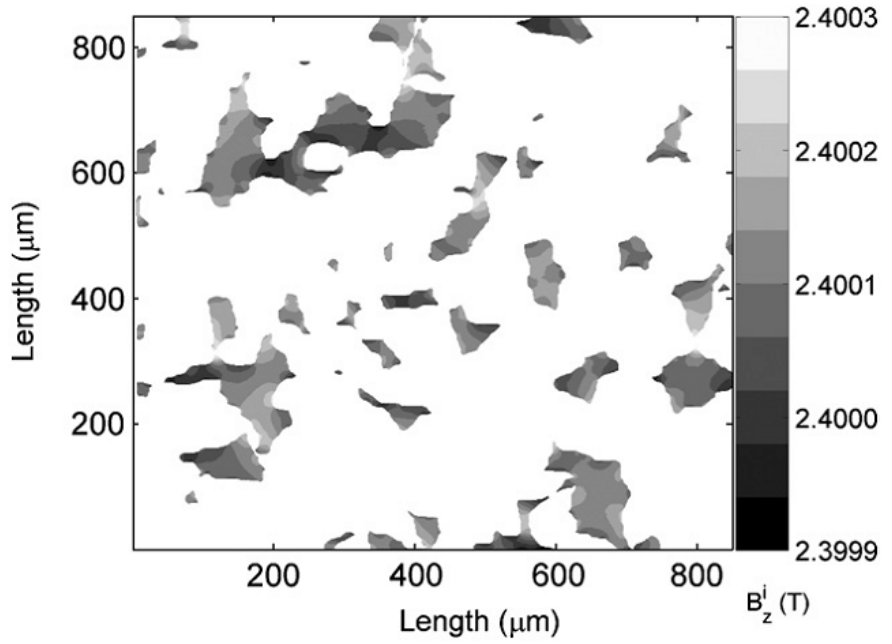

Fig. 4. Internal magnetic field (B_z^i) distribution in the water phase for Berea saturated with water, determined through simulation. FOV, 850 μm × 850 μm and spatial resolution, 1.1 μm. The external field ($B_0 = 2.4$ T) is applied in the horizontal (z) direction, from left to right. The grayscale bar on the righthand side of the figure indicates the magnitude of the internal field.

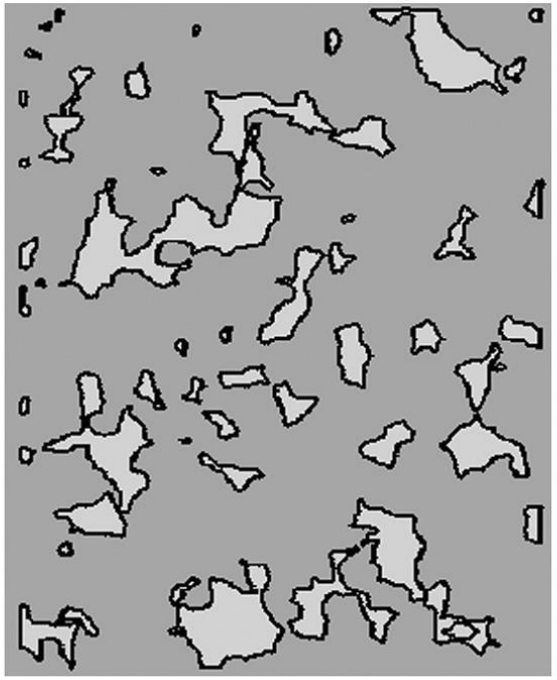

Fig. 2. A 2D simulation model for a 100% water saturated Berea sandstone, which was extracted from the thin-section images. FOV, 921 μm × 1228 μm. Gray and white represent solid matrix and water, respectively.

Chen et al., *J. Magn. Reson.* 2005;175:300-308.

Contraste de suscetibilidade magnética em meios porosos

Distribuição de campo magnético (simulação):

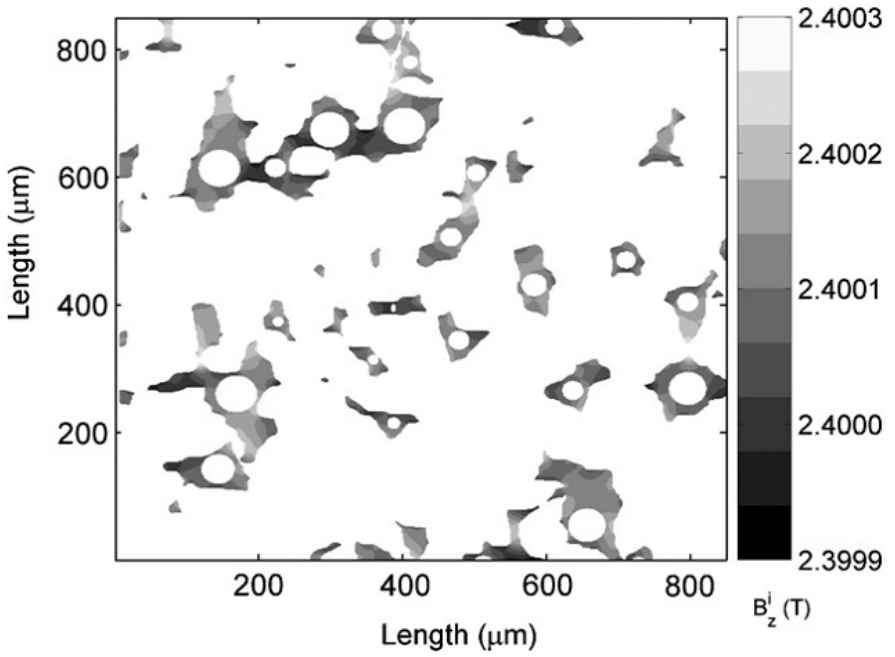

Fig. 5. Internal magnetic field (B_z^i) distribution in the water phase for Berea saturated with water and air, determined through simulation. FOV, 850 μm × 850 μm and spatial resolution, 1.1 μm. The external field ($B_0 = 2.4$ T) is applied in the horizontal (z) direction, from left to right. The grayscale bar on the righthand side of the figure indicates the magnitude of the internal field.

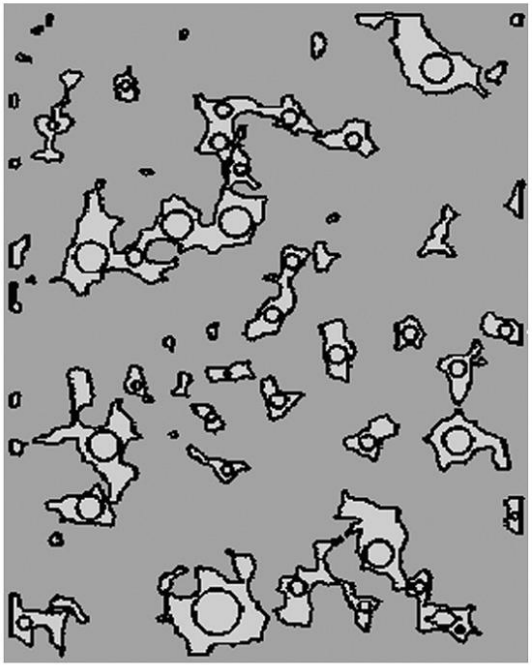

Fig. 3. A 2D simulation model for a Berea sandstone saturated with water and air, where the water spreads on the surface of the pore space, while the air occupies the pore center, due to the effect of wettability. FOV, 921 μm × 1228 μm. Gray and white represent solid matrix and water, respectively. The circles represent air bubbles.

Chen et al., *J. Magn. Reson.* 2005;175:300-308.

Contraste de suscetibilidade magnética em meios porosos

Distribuição de campo magnético (simulação):

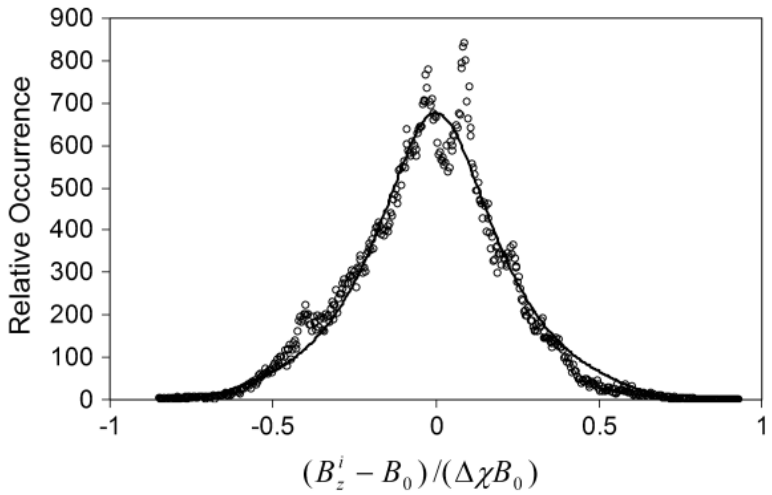

Fig. 6. Histogram plot of the internal magnetic field $(B_z^i, \circ)$ distribution (scaled with dimensionless form: $(B_z^i - B_0)/\Delta\chi B_0)$ in the water phase for a fully water saturated Berea sandstone, determined through simulation, with a linewidth (FWHM) of 0.3. The best fit line is a Lorentzian function, with R^2 of 0.97.

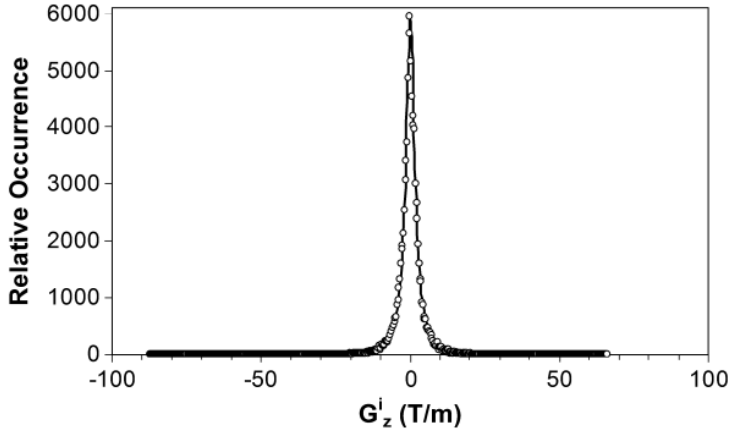

Fig. 12. Histogram plot of the internal magnetic field gradient $(G_z^i, \circ)$ distribution in the water phase for a water saturated Berea sample, determined through simulation, with a linewidth of 3.5 T/m, B_0 of 2.4 T. The best fit line is a Lorentzian function with zero-mean and R^2 of 0.992.

Chen et al., *J. Magn. Reson.* 2005;175:300-308.

Contraste de suscetibilidade magnética em meios porosos

Espectro (FT) e decaimento (FID):

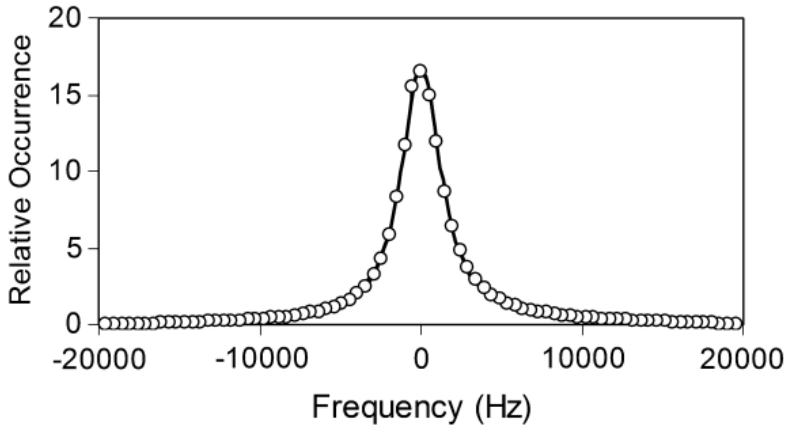

Fig. 8. MR absorption lineshape for a water saturated Berea sandstone obtained by FID measurement (○) with a static magnetic field (B_0) of 2.4 T. The best fit line is a Lorentzian function, with R^2 of 0.999.

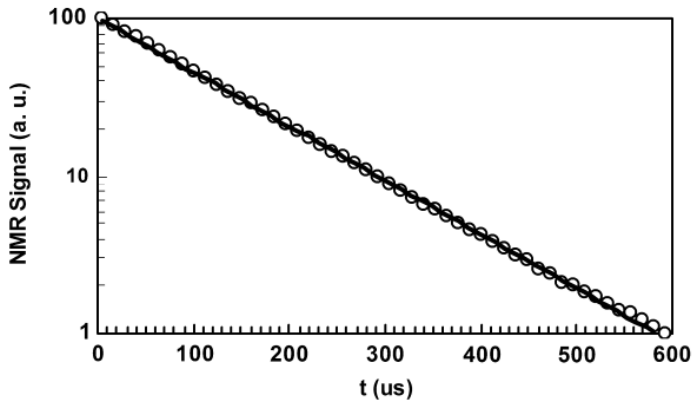

Fig. 15. A FID decay measurement for a water saturated Berea sandstone at a static magnetic field (B_0) of 2.4 T. The single exponential best fit line has a decay time constant T_2^* of 127 μs. The single exponential T_2^* decay behavior is very general for sedimentary rocks and concretes, with different fluid saturations, at different magnetic field strengths.

$$\Delta\nu \propto \Delta\chi \cdot B_0$$

$$\frac{1}{T_2^*} \propto \Delta\chi \cdot B_0$$

Chen et al., *J. Magn. Reson.* 2005;175:300-308.

Contraste de suscetibilidade magnética em meios porosos

Alargamento para diferentes campos magnéticos aplicados:

$$\Delta\nu \propto \Delta\chi \cdot B_0$$

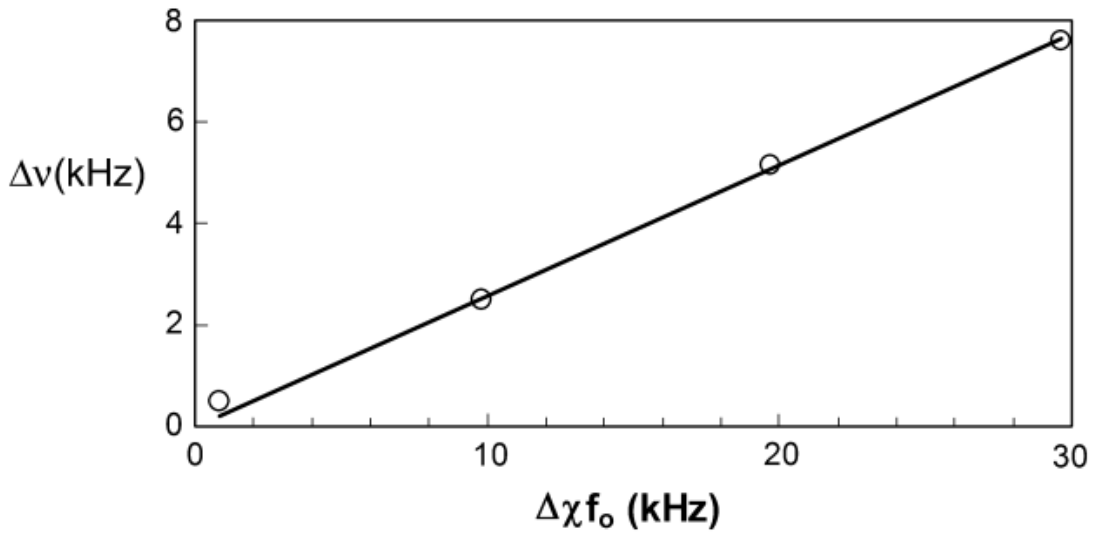

Fig. 16. NMR linewidth measured at four different magnetic fields (B_0) (7.0, 4.7, 2.4, and 0.2 T) for a water saturated Berea sandstone. There is a linear relationship between the linewidth ($\Delta\nu$) and the product of the susceptibility difference ($\Delta\chi$) and Larmor frequency (f_0). The best fit line is given by $\Delta\nu = 0.26\Delta\chi f_0$.

Chen et al., *J. Magn. Reson.* 2005;175:300-308.

Relaxometria por RMN de ^{1}H

RMN em baixo campo – aplicações em petrofísica:

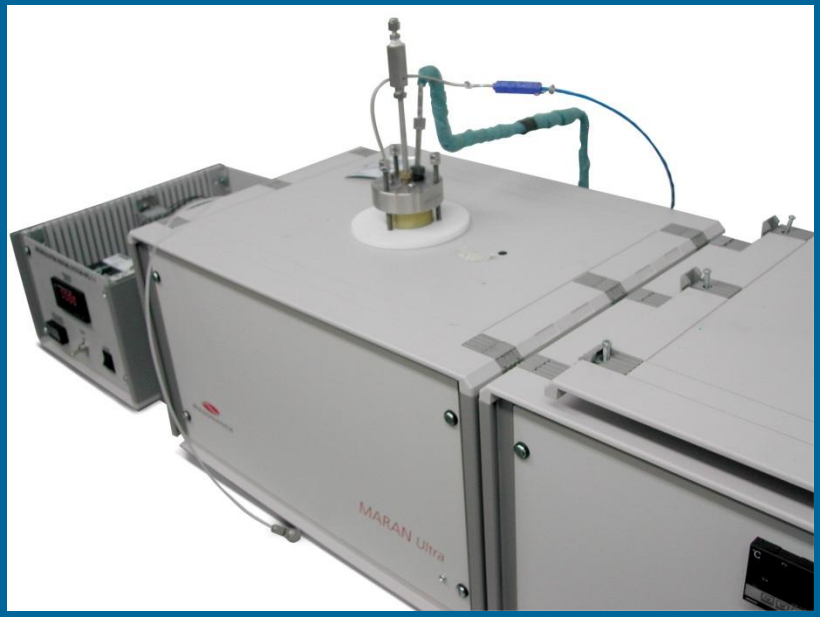

Relaxometria por RMN de ^{1}H

Sequência CPMG:

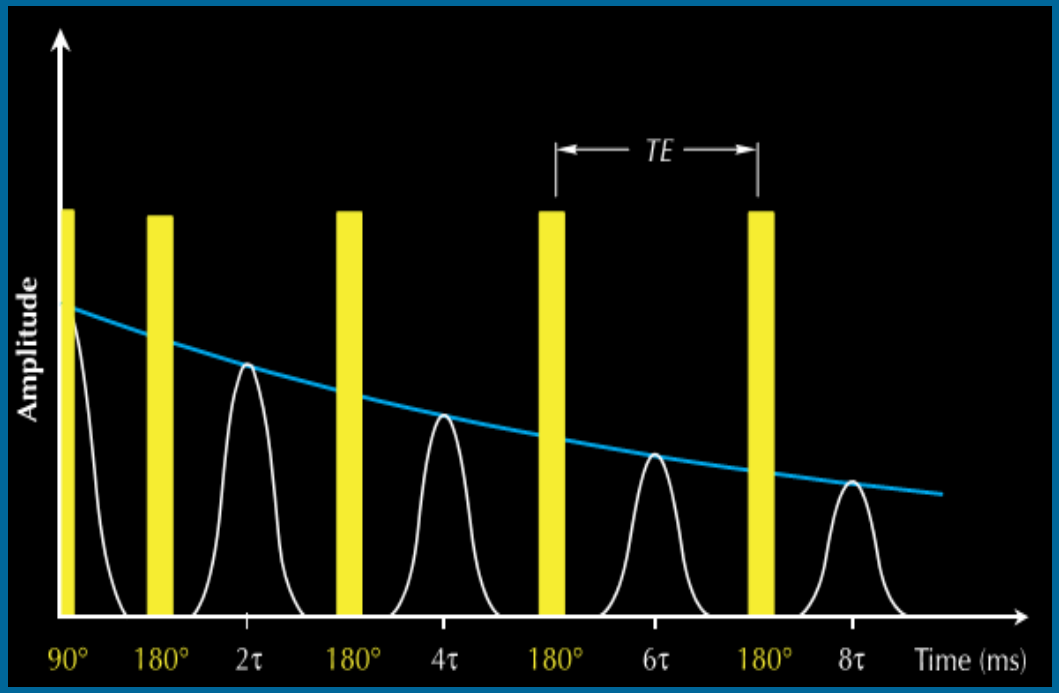

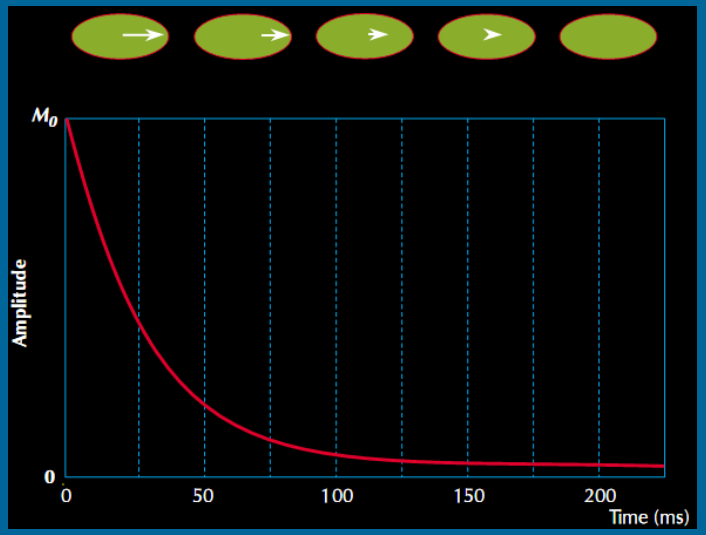

"**NMR Logging: Principles and Applications**". G. Coates, L. Xiao,M. G. Prammer, Halliburton Energy Services, 1999

Distribuição de tempos de relaxação

Transformada de Laplace Inversa (ILT):

$$M(t) = \sum_{k=1}^{N} A(T_{2k}) e^{-t/T_{2k}}$$

$$M(t) \xrightarrow{\text{ILT}} A(T_2)$$

Algoritmo de regularização: CONTIN

Aplicações: fluidos complexos (petróleo), meios porosos, alimentos, etc.

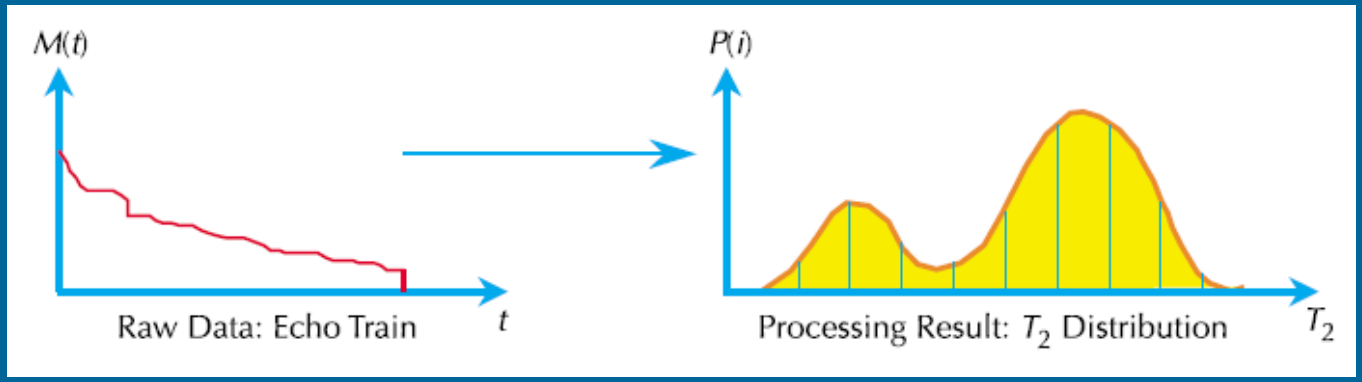

"**NMR Logging: Principles and Applications**". G. Coates, L. Xiao,M. G. Prammer, Halliburton Energy Services, 1999

Relaxometria por RMN de ^1H

Halliburton Energy Services

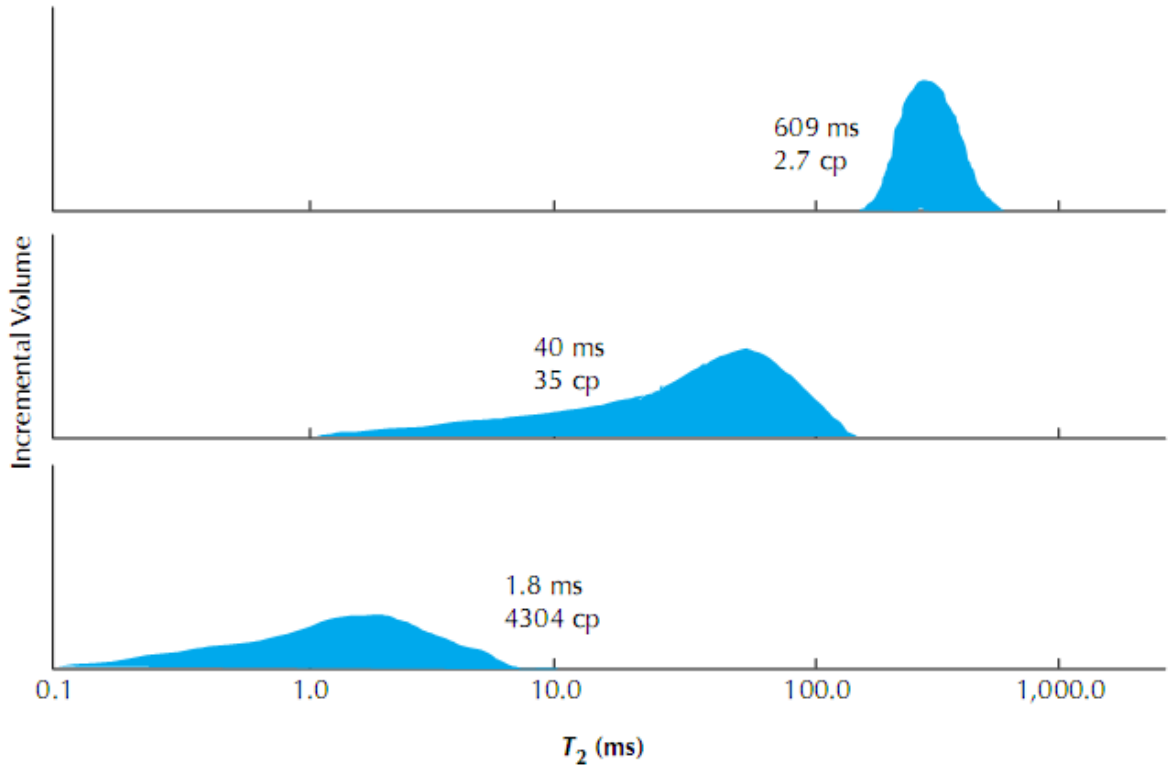

om000866

Figure 4.1—The T_2 of crude oil varies with viscosity, as shown in these T_2 distributions for three oil samples. For the light oil (top), which has a viscosity of 2.7 cp, the measured T_2 values are clustered tightly about a single value, namely, 609 ms. For the medium-viscosity oil (middle), which has a viscosity of 35 cp, the measured T_2 values form a broad distribution with a lower-end tail and a geometric mean of 40 ms. For a much heavier crude oil (bottom), which has a viscosity of 4304 cp, the measured T_2 values also form a broad distribution with a lower-end tail but with a geometric mean of only 1.8 ms.

"**NMR Logging: Principles and Applications**". G. Coates, L. Xiao,M. G. Prammer, Halliburton Energy Services, 1999

RMN de ^{1}H em petróleo pesado

Relaxometria: 2,0 MHz

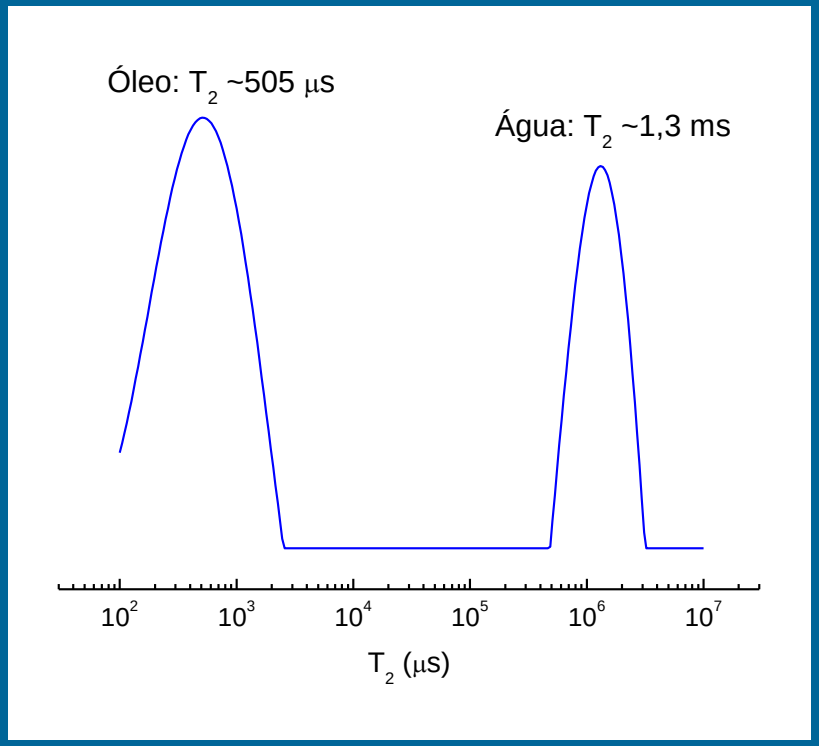

Espectroscopia: 400 MHz

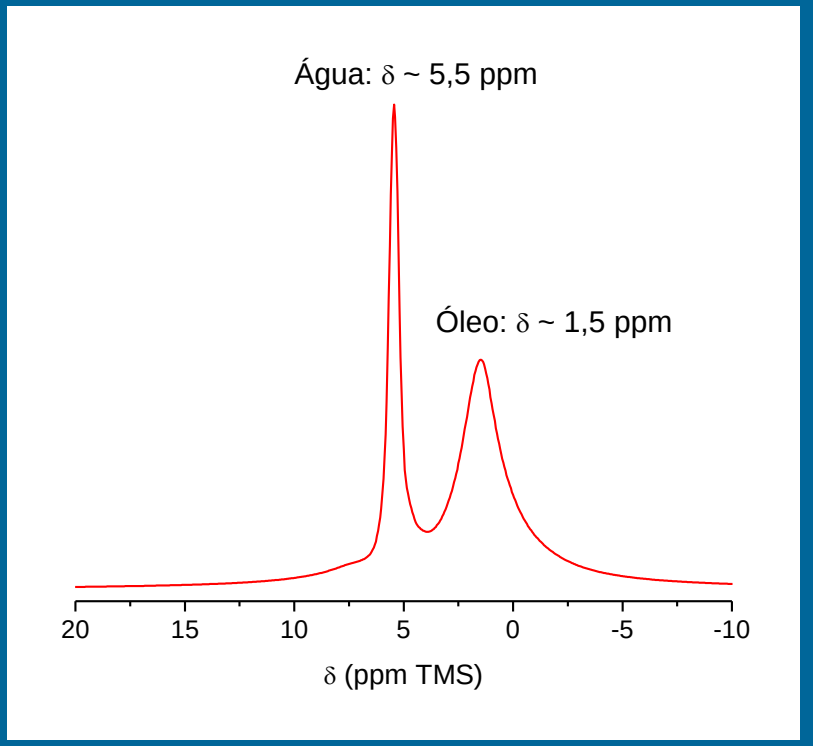

Aplicações em petrofísica

Figure 3.1—The relaxation of pore fluids is due to bulk, surface, and diffusion mechanisms.

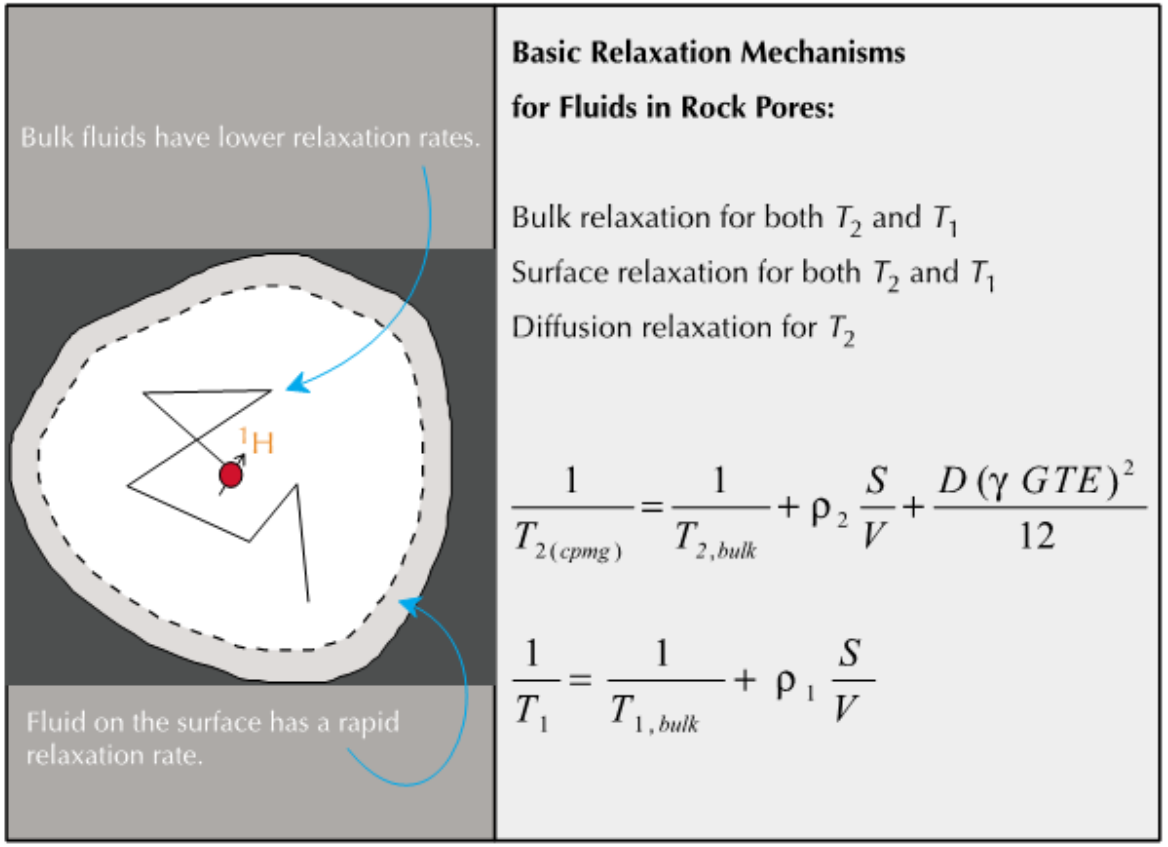

"**NMR Logging: Principles and Applications**". G. Coates, L. Xiao,M. G. Prammer, Halliburton Energy Services, 1999

Aplicações em petrofísica

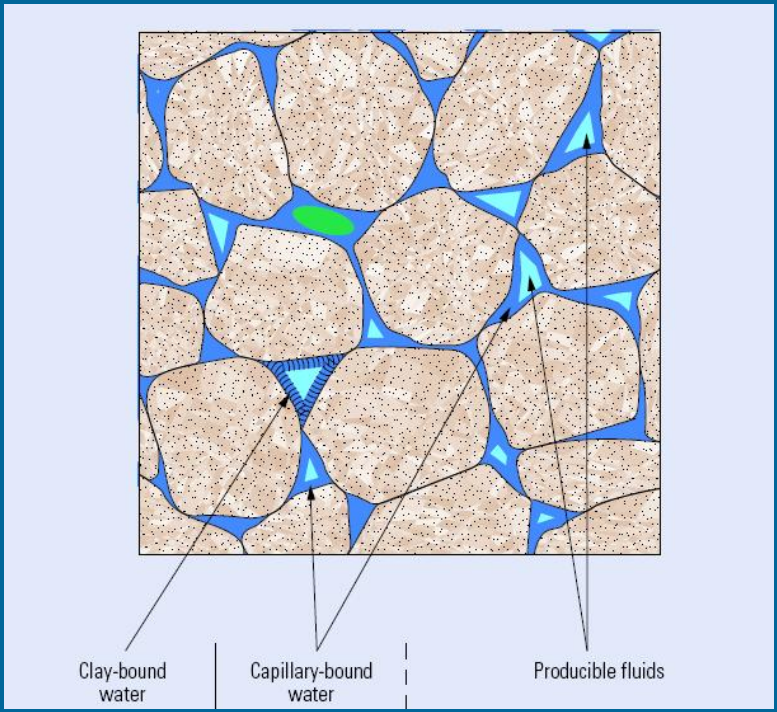

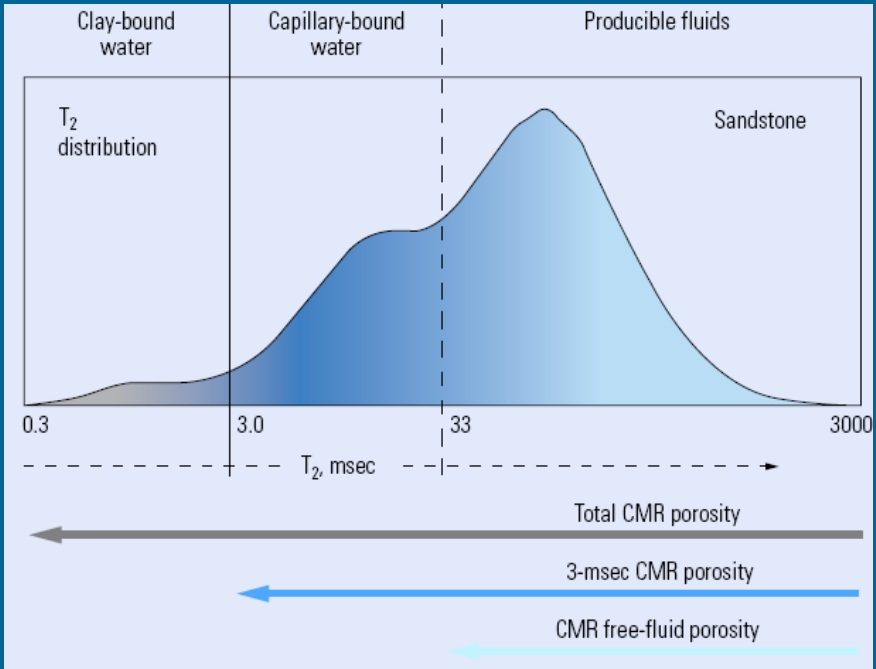

"**NMR Logging: Principles and Applications**". G. Coates, L. Xiao,M. G. Prammer, Halliburton Energy Services, 1999

Aplicações em petrofísica

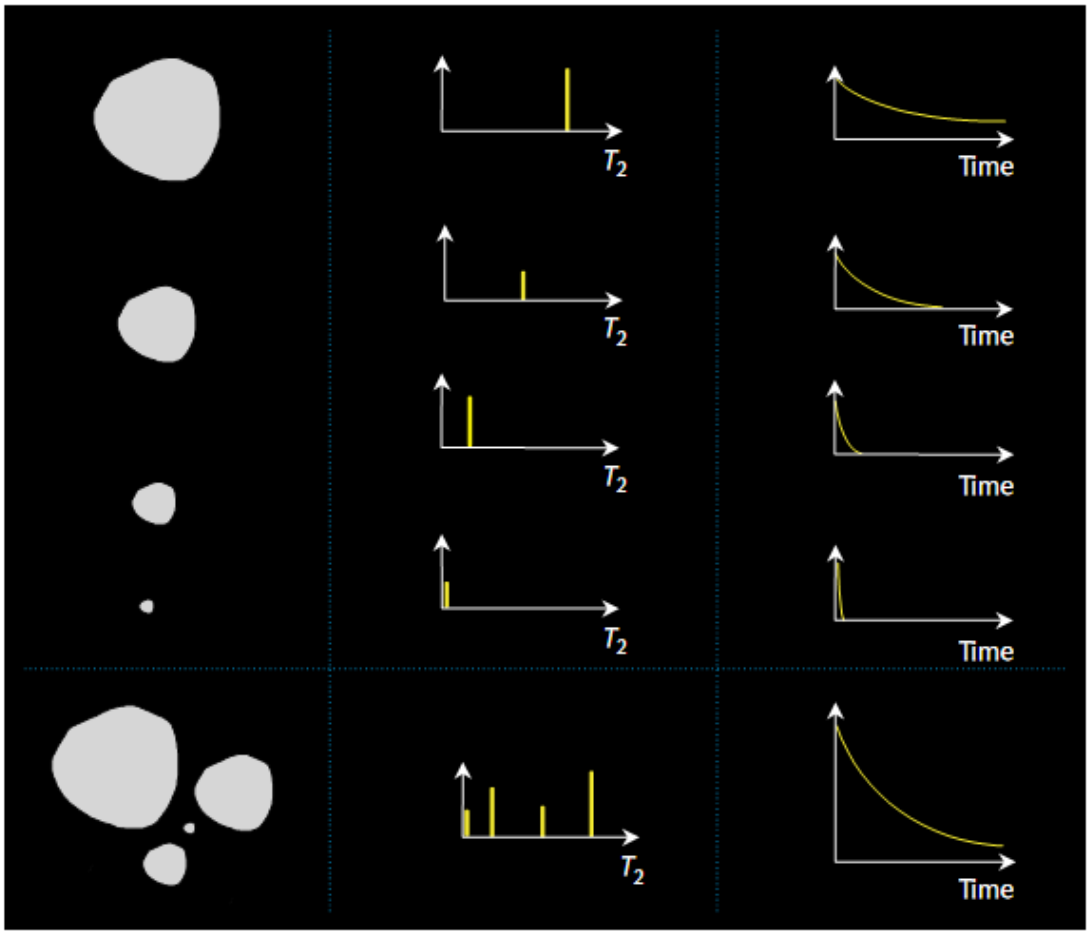

Figure 3.2—A 100% water-saturated pore (upper left) has a single T_2 value (upper center) that depends on pore size, and thus its spin-echo train exhibits a single-exponential decay (upper right) that also depends on pore size. Multiple pores at 100% water saturation (bottom left) have multiple T_2 values (bottom center) that depend on the pore sizes, and thus their composite spin-echo train exhibits multi-exponential decay (bottom right) that also depends on the pore sizes.

"**NMR Logging: Principles and Applications**". G. Coates, L. Xiao,M. G. Prammer, Halliburton Energy Services, 1999

Distribuição de T_2 e de tamanhos de poros

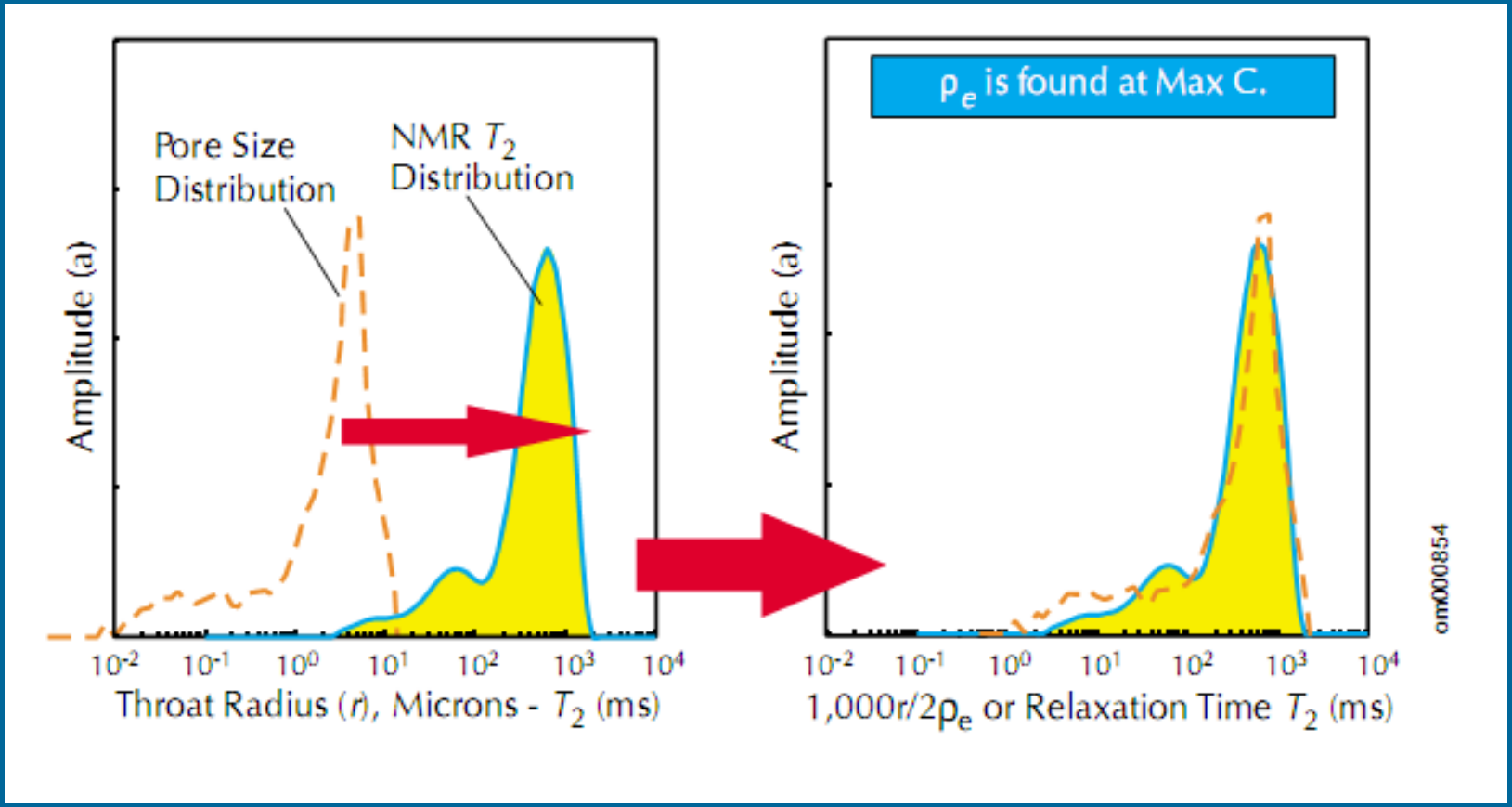

"**NMR Logging: Principles and Applications**". G. Coates, L. Xiao,M. G. Prammer, Halliburton Energy Services, 1999

Distribuição de T_2 e de tamanhos de poros

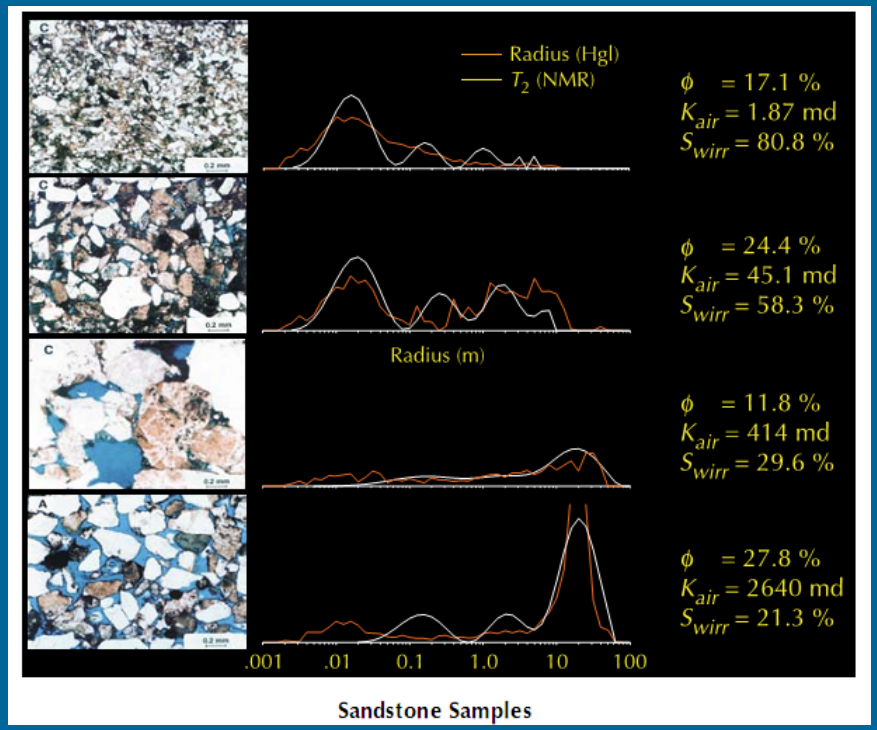

Sandstone Samples

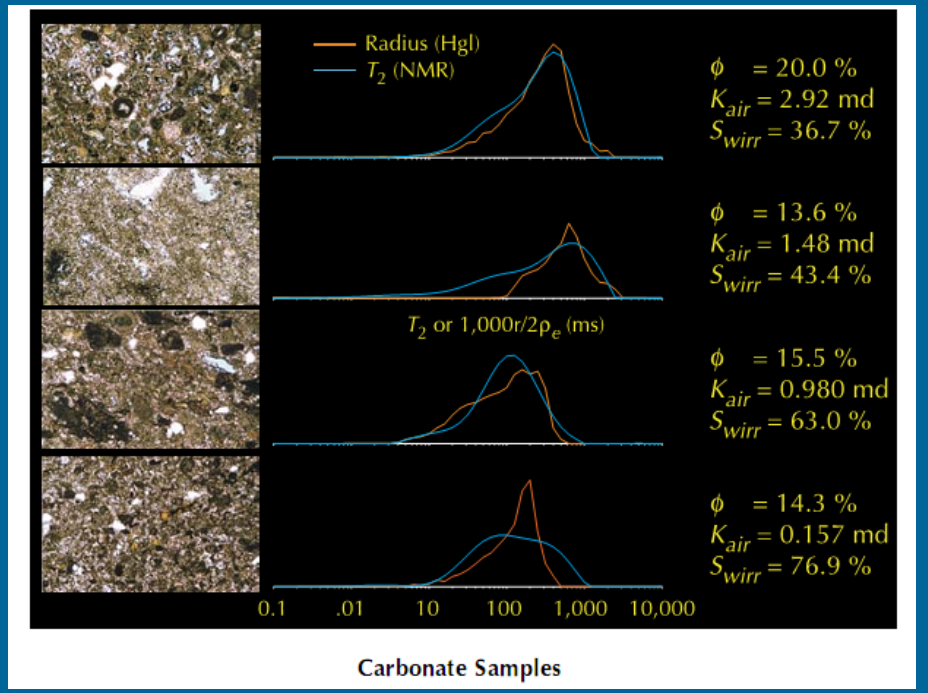

Carbonate Samples

"**NMR Logging: Principles and Applications**". G. Coates, L. Xiao,M. G. Prammer, Halliburton Energy Services, 1999

Relaxometria por RMN de ^1H

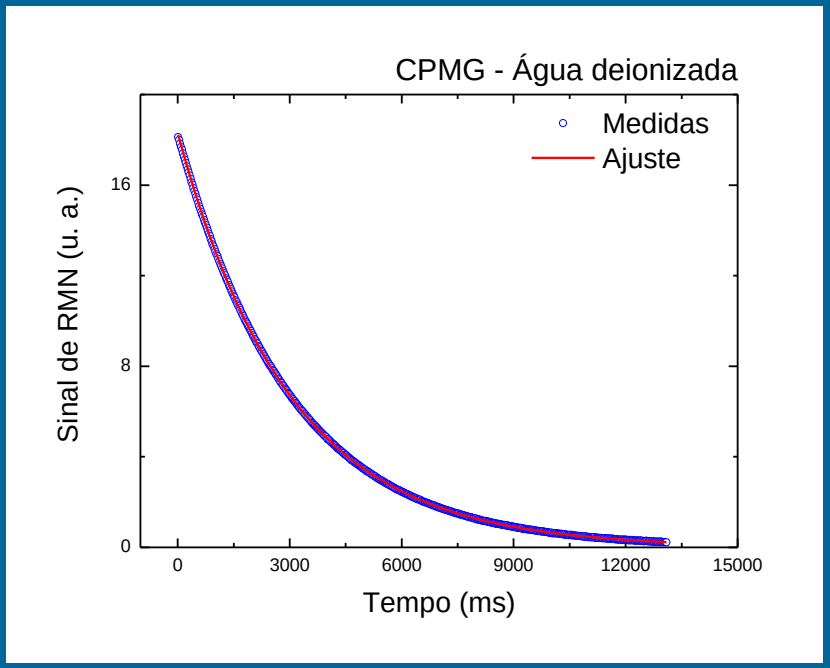

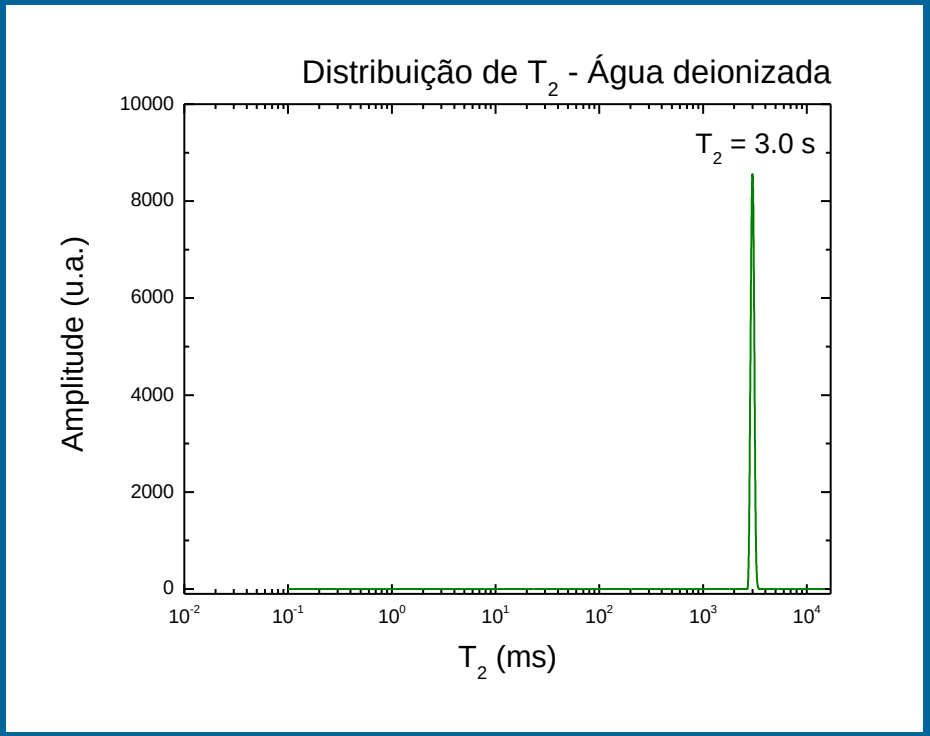

f_L = 2,0 MHz; B_0 = 47mT

Relaxometria por RMN de ^1H

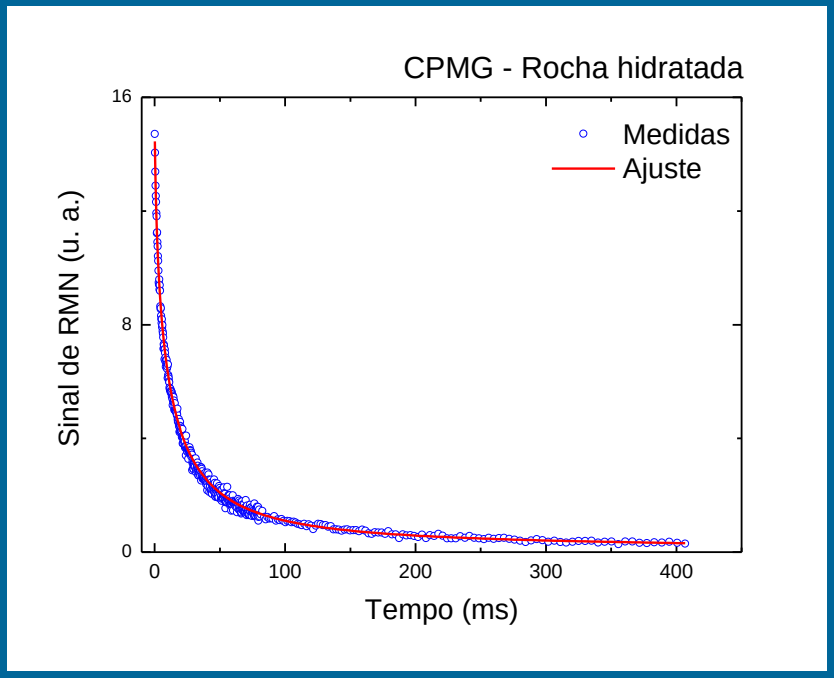

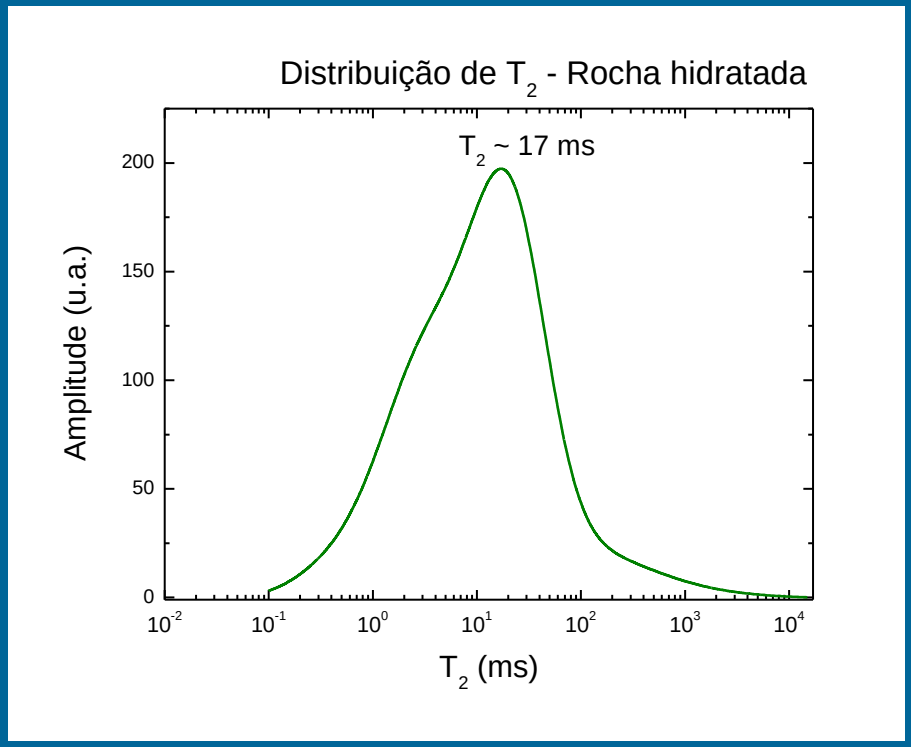

f_L = 2,0 MHz; B_0 = 47mT

Relaxometria por RMN de ^{1}H

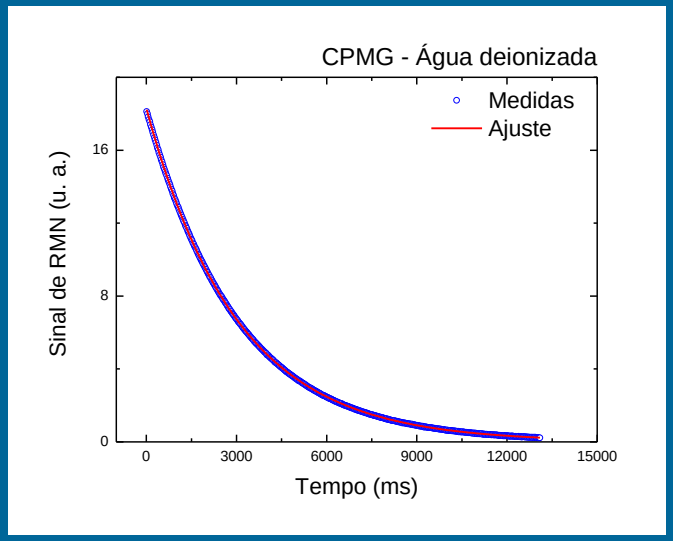

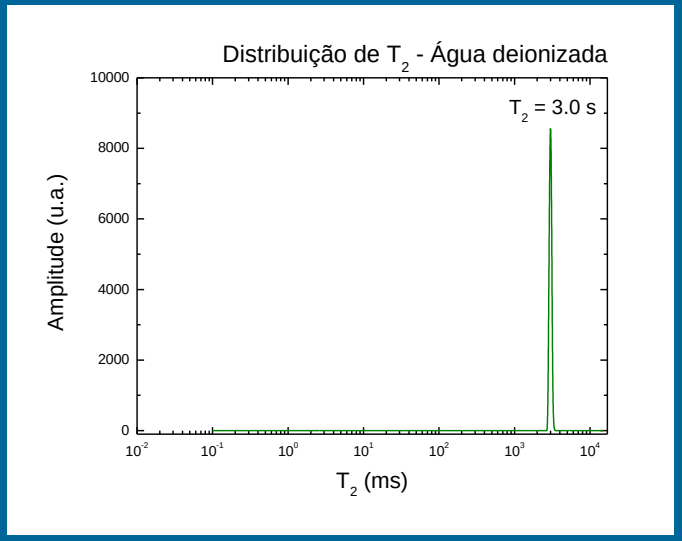

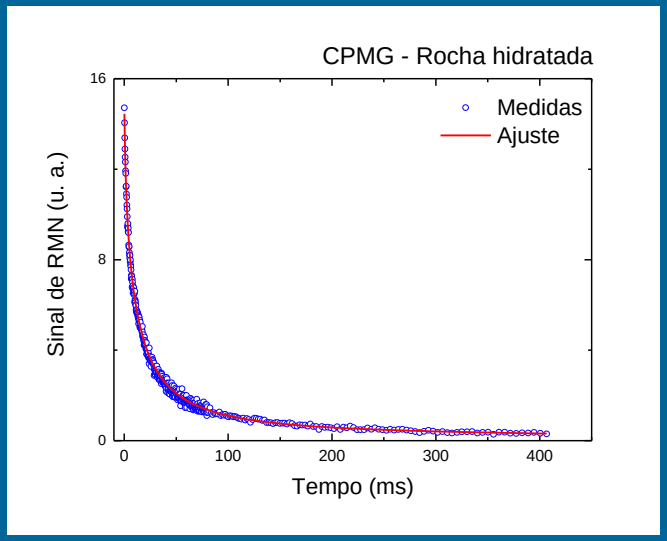

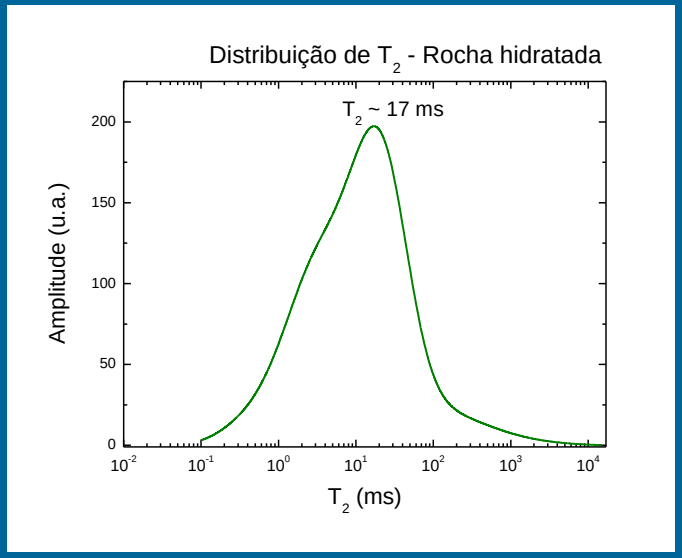

Aplicações em petrofísica

Figure 1.4—The decay of a spin-echo train, which is a function of the amount and distribution of hydrogen present in fluids, is measured by recording the decrease in amplitude of the spin echoes over time. Petrophysicists can use decay-rate information to establish pore-fluid types and pore-size distributions. In this example, the spin echoes are recorded at 1-ms inter-echo spacing. The discrete points in this figure represent the raw data, and the solid curve is a fit to that data.

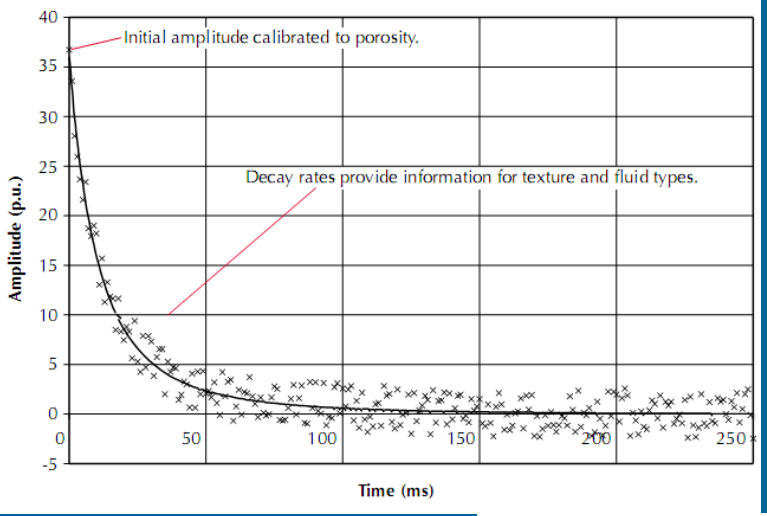

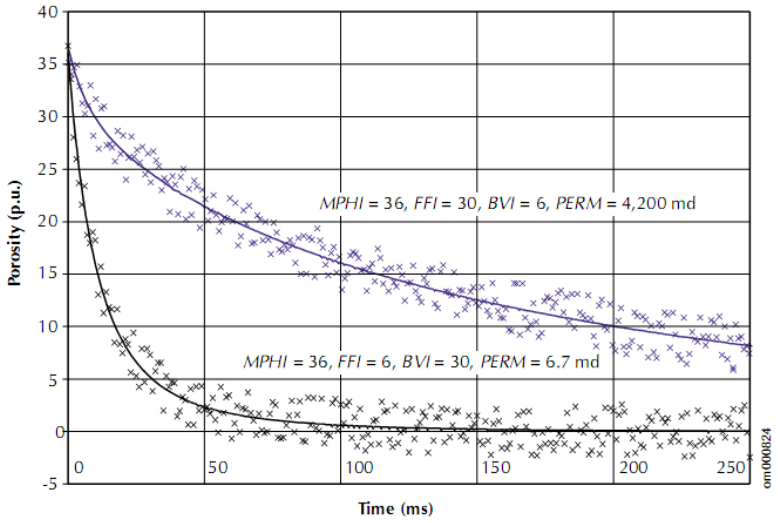

Figure 1.10—Two echo trains were obtained from formations with different permeability. Both formations have the same porosity but different pore sizes. This difference leads to shifted T_2 distributions, and therefore to different values of the ratio of *MFFI* to *BVI*. The permeabilities computed from the Coates model {$k = [(MPHI/C)^2(MFFI/BVI)]^2$, where k is formation permeability and C is a constant that depends on the formation} also are indicated in the figure.

"**NMR Logging: Principles and Applications**". G. Coates, L. Xiao,M. G. Prammer, Halliburton Energy Services, 1999

Estudo de meios porosos – métodos de RMN de sólidos

Contraste de suscetibilidade magnética – *alargamento inomogêneo*:

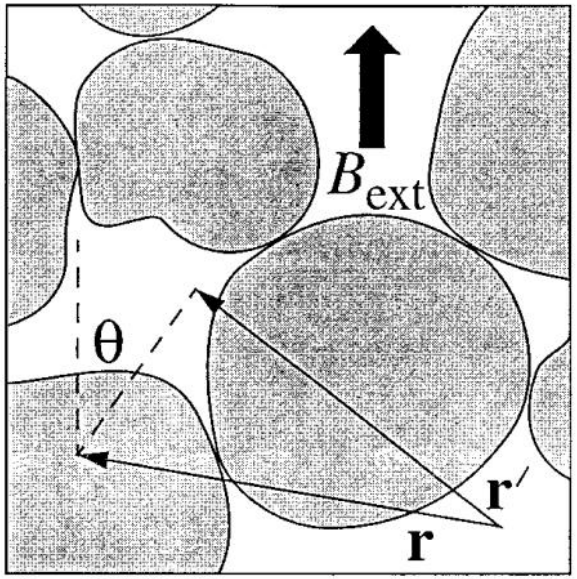

FIG. 1. Sketch of sandstone showing the geometric parameters in Eq. [1].

$$\mathbf{B}_{\mathrm{dip}}(\mathbf{r}') \cdot \hat{z} = \frac{B_{\mathrm{ext}}}{4\pi} \int \chi(\mathbf{r}) \frac{(3\cos^2\theta - 1)}{|\mathbf{r}' - \mathbf{r}|^3} d\mathbf{r},$$

Pines et al., *J. Magn. Reson.* 1998;133:385-387.

Estudo de meios porosos – métodos de RMN de sólidos

RMN de ^{1}H com MAS :

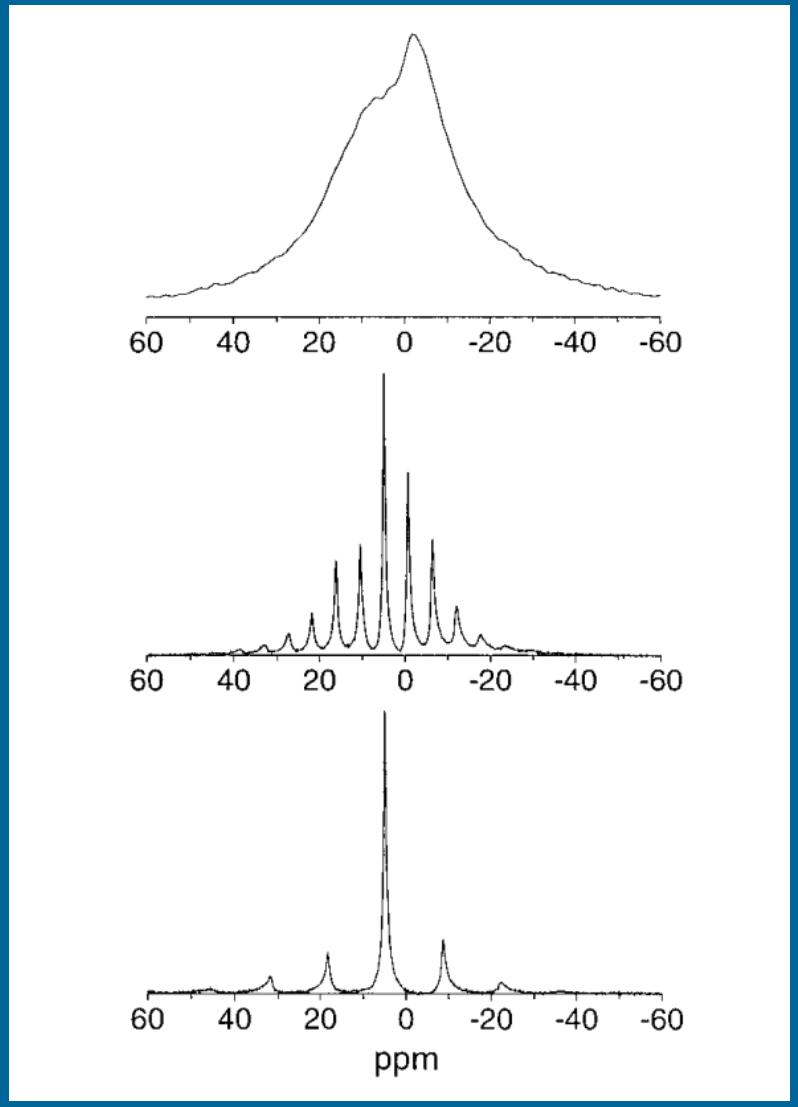

FIG. 2. The effect of MAS on ^{1}H NMR spectra of Berea sandstone saturated with water. The spectra from top to bottom are the results of spinning the sample at 0 Hz, 1 kHz, and 2.5 kHz, respectively. Spectra were recorded at 300 K on a Chemagnetics Infinity spectrometer operating at 4.2 T, using a home-built MAS probe. The rock samples were saturated with fluid under vacuum and sealed into vespel capsules with an epoxy putty. The vespel signal has been subtracted from all spectra. The capsules were machined to fit precisely into 7-mm zirconia rotors. Typical 90° pulse lengths were 5 μs. The chemical shift is referred to tetramethylsilane at 0 ppm.

Pines et al., *J. Magn. Reson.* 1998;133:385-387.

Estudo de meios porosos – métodos de RMN de sólidos

RMN de ^{1}H com MAS :

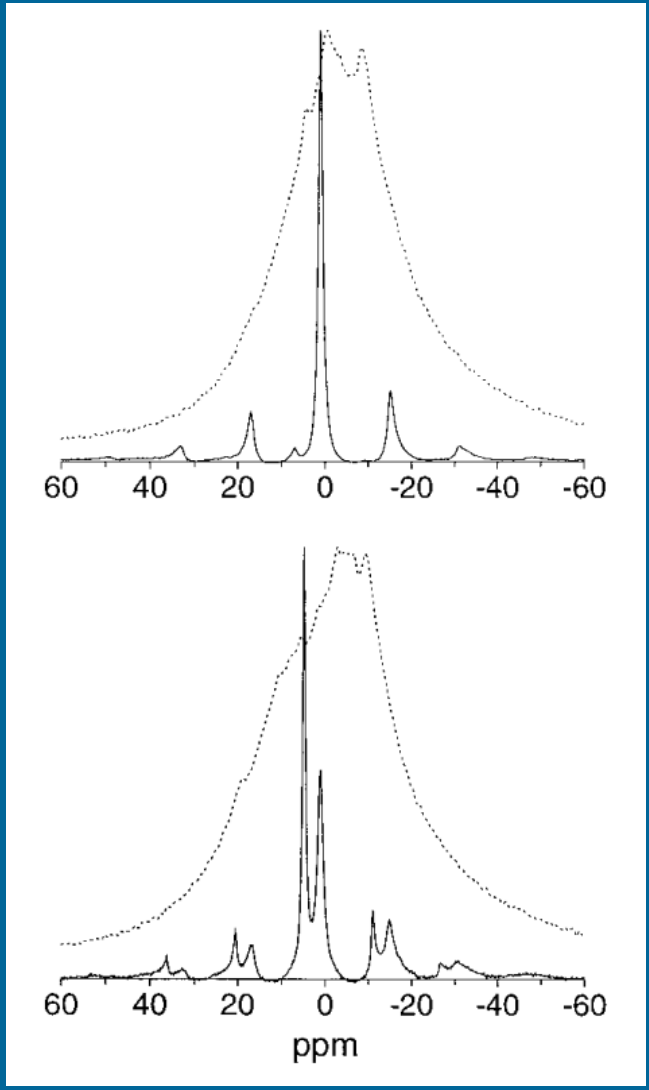

FIG. 3. ^{1}H MAS–NMR spectra of Berea sandstone saturated with a light crude oil (top), and a mixture of crude and water (bottom). The spinning speed was 2 kHz in both cases. The dotted line shows the spectra with a static sample in each case. Other experimental conditions are as in Fig. 2.

Pines et al., *J. Magn. Reson.* 1998;133:385-387.

Estudo de meios porosos – métodos de RMN de sólidos

RMN de ^{1}H – Sequência T1-MAS-2D:

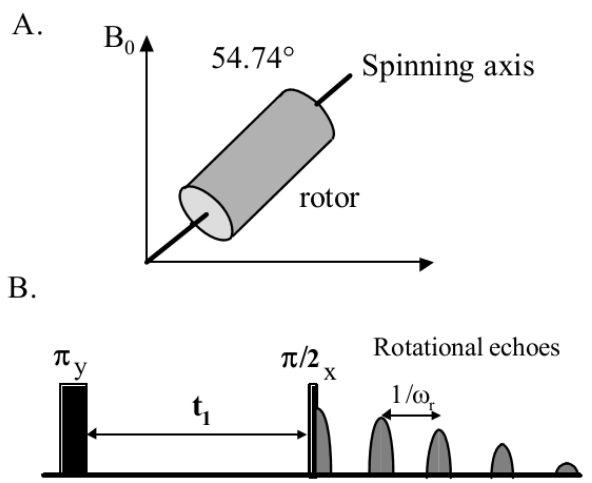

Figure 1. Diagram of T1-MAS 2D pulse sequence. (A) The magic angle spinning of rock samples. The rotor size is 4 mm in OD and 20mm in length. It holds about 170 mg of crushed rock sample and rotates at speed (ω_r) of 10 kHz. (B) The inversion recovery pulse sequence for T_1 measure-ment. The time t_1 varies from 0.2 ms to 2 seconds unevenly.

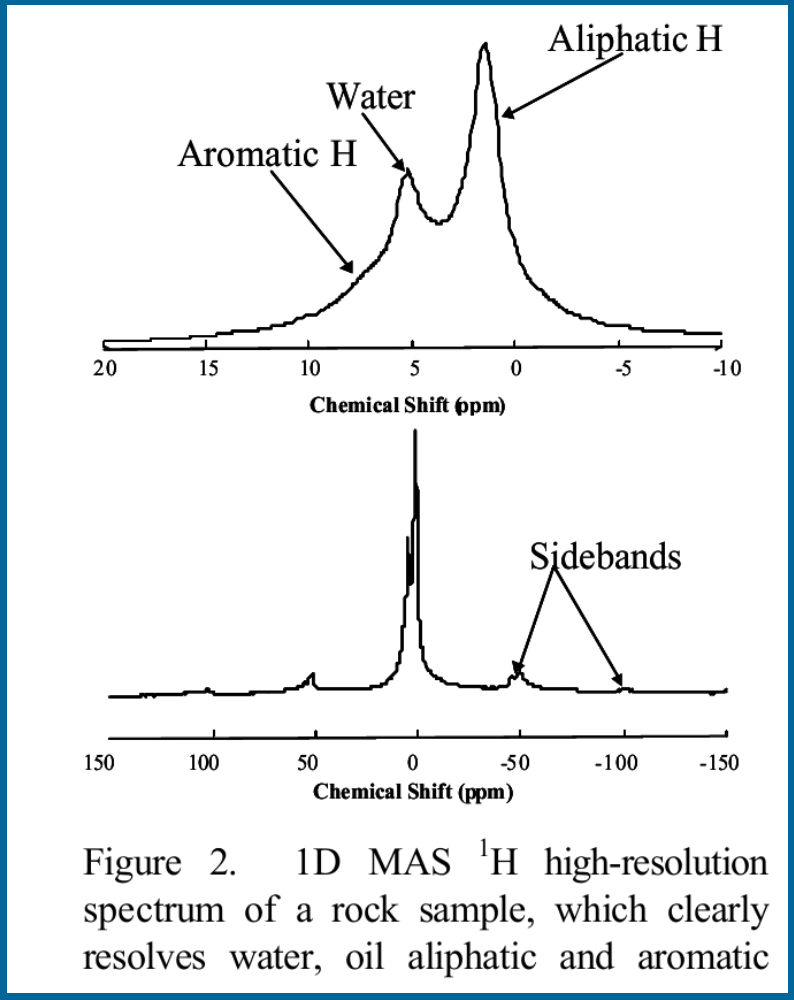

Figure 2. 1D MAS ^{1}H high-resolution spectrum of a rock sample, which clearly resolves water, oil aliphatic and aromatic

B. Sun, K.-J. Dunn, Symposium of Society of Core Analysts, Paper 38 (2002).

Estudo de meios porosos – métodos de RMN de sólidos

RMN de ^{1}H – Sequência T1-MAS-2D:

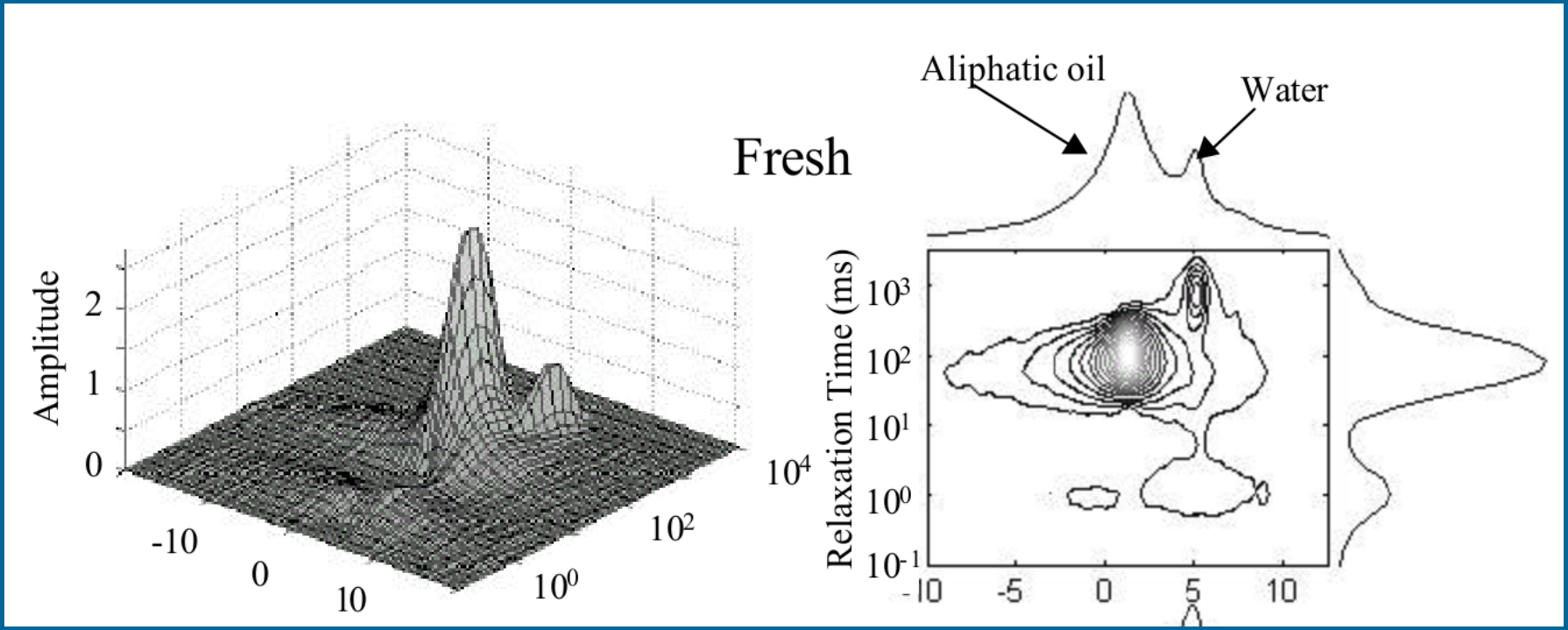

B. Sun, K.-J. Dunn, Symposium of Society of Core Analysts, Paper 38 (2002).

Estudo de meios porosos – métodos de RMN de sólidos

RMN de ^{1}H – Sequência T1-MAS-2D:

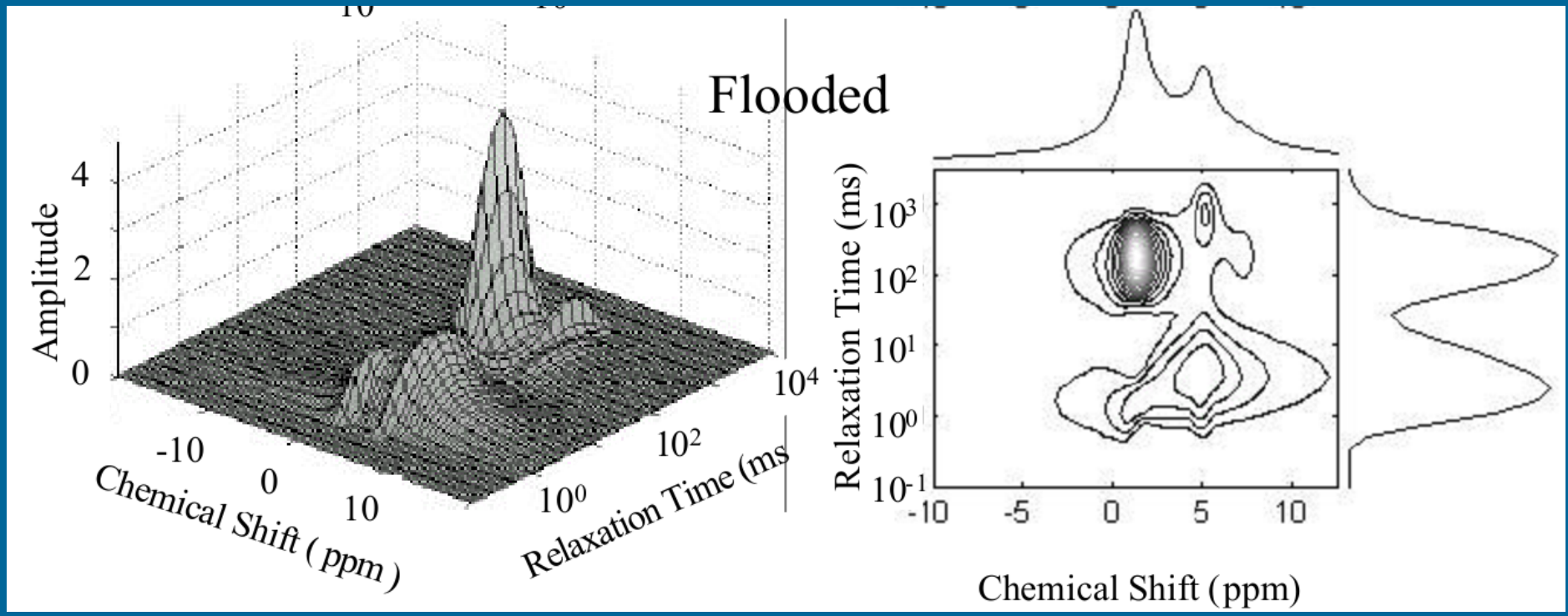

B. Sun, K.-J. Dunn, Symposium of Society of Core Analysts, Paper 38 (2002).

Materiais de carbono micro e mesoporosos

Carvões ativados:

- Sólidos estruturalmente desordenados com rede de poros irregular.
- Distribuiçoes de macroporos, mesoporos e microporos.
- Applicações: suporte de catalisadores, tratamento de água, armazenamento de gases, ...
- Composição básica: C, H, O (majoritários), N, S, ...
- Matéria mineral (cinzas): depende do precursor e da preparação.

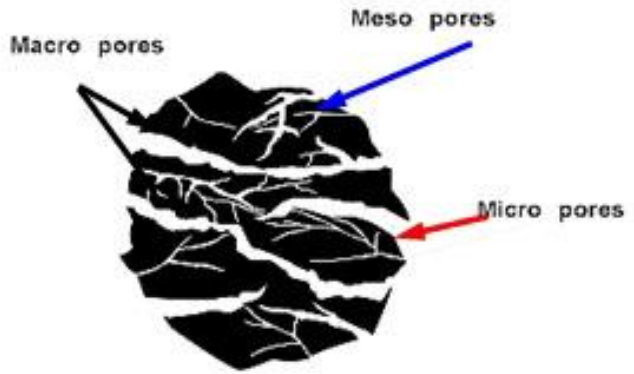

Figure 1: Activated carbon structure - schematic.

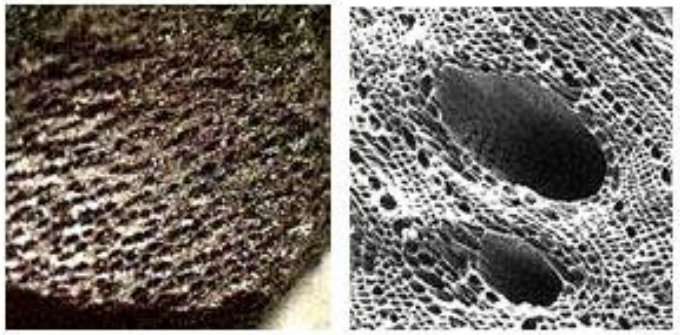

Figure 2: Activated carbon structure – SEM pictures.

http://www.afssociety.org/education/0209oneminute.html

Materiais de carbono micro e mesoporosos

Carvões ativados:

- Sólidos estruturalmente desordenados com rede de poros irregular.
- Distribuiçoes de macroporos, mesoporos e microporos.
- Applicações: suporte de catalisadores, tratamento de água, armazenamento de gases, ...
- Composição básica: C, H, O (majoritários), N, S, ...
- Matéria mineral (cinzas): depende do precursor e da preparação.

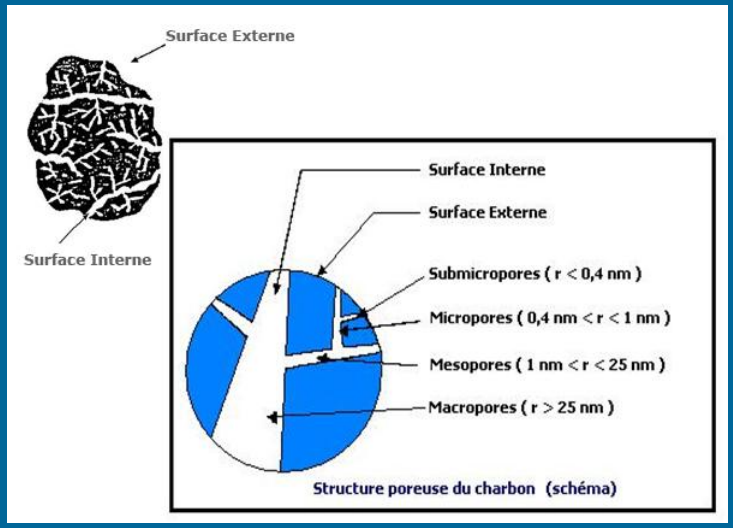

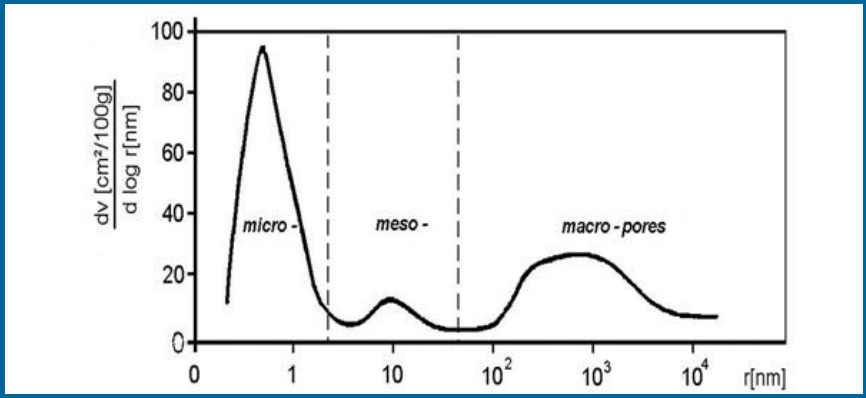

http://www.asseau.com/en/03-9.html

Materiais de carbono micro e mesoporosos

Carvões ativados:

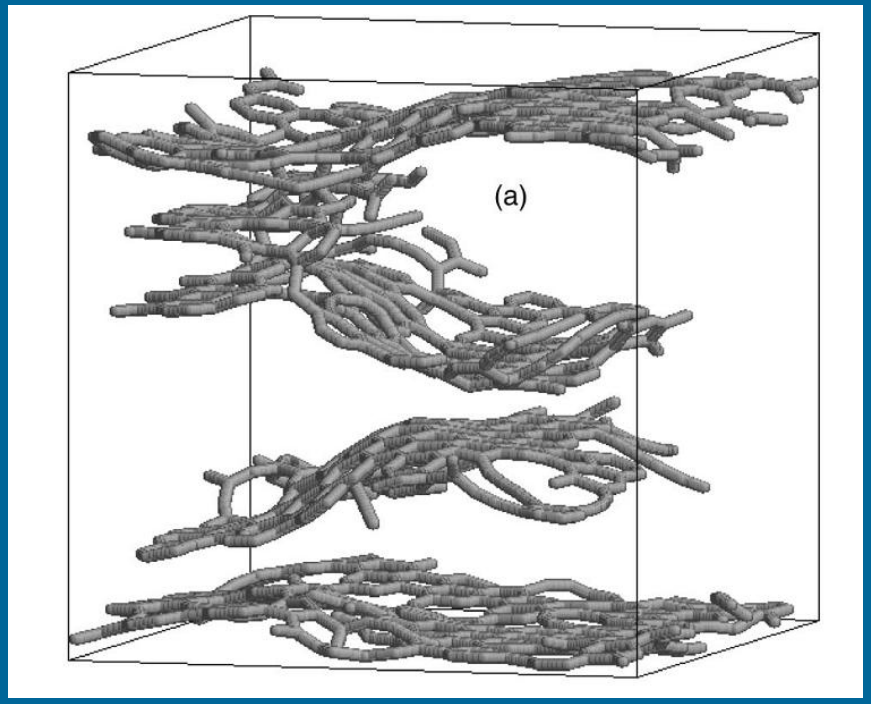

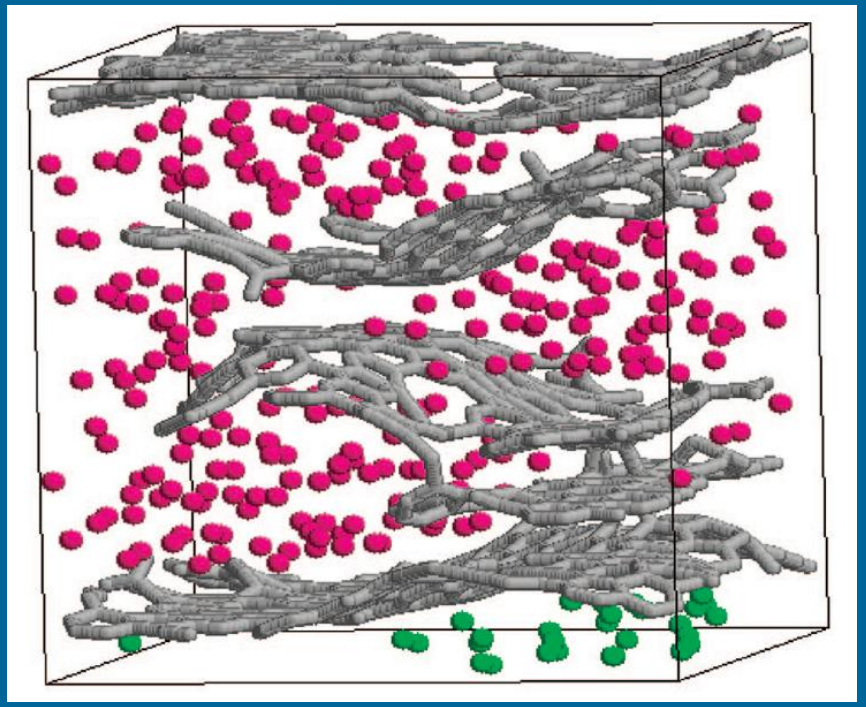

Nguyen et al., *Langmuir* 2008;24:7912-7922.

Alargamento homogêneo e inomogêneo em sólidos

RMN de ^{23}Na – carvões ativados quimicamente (NaOH):

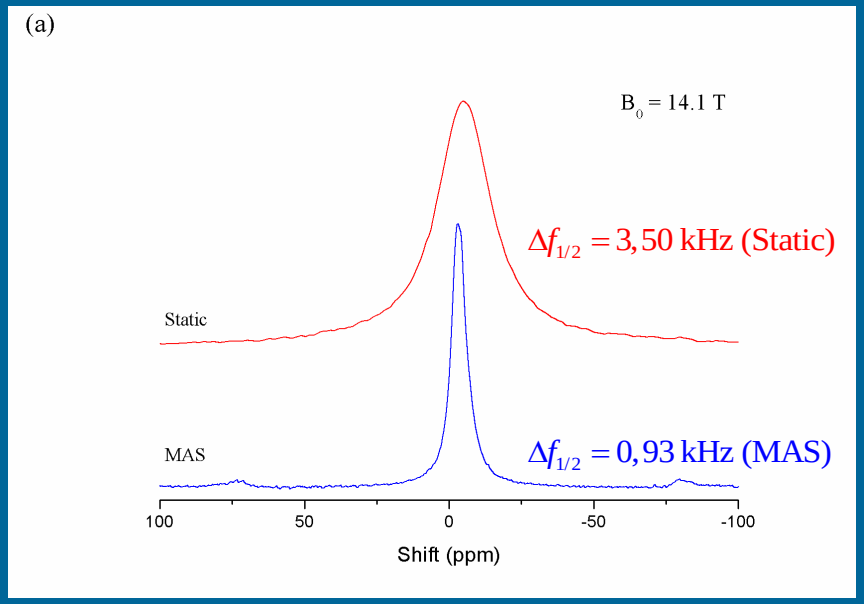

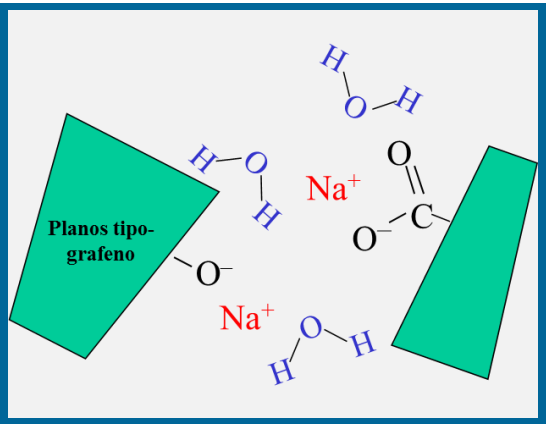

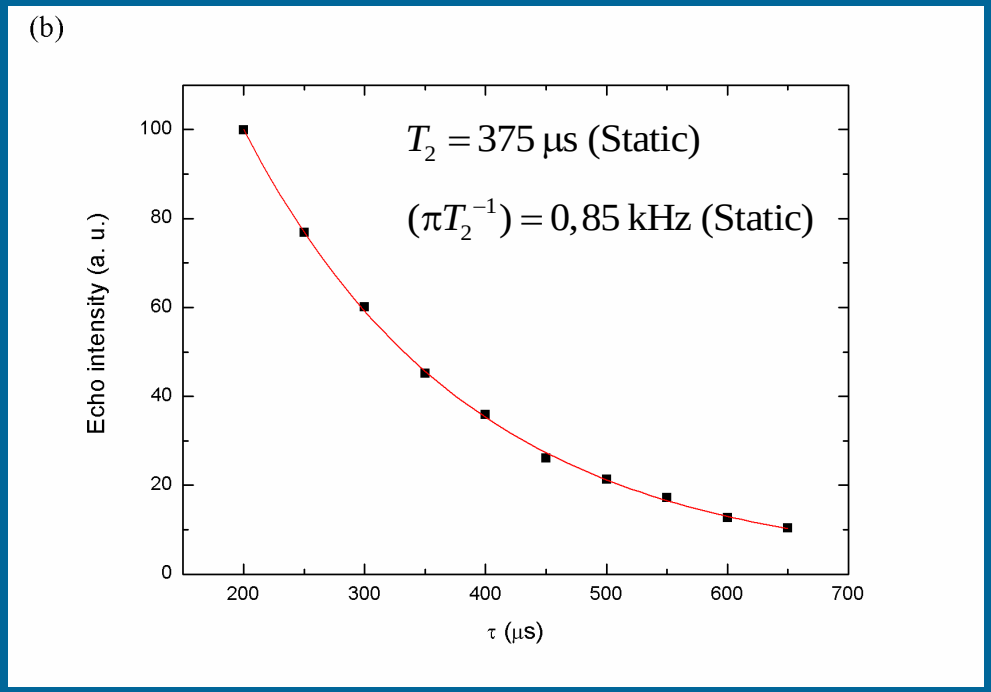

Freitas et al., *Solid State Nucl. Magn. Reson.* 2007;32:109-117.

Espécies adsorvidas em carvões ativados

RMN de ^{1}H :

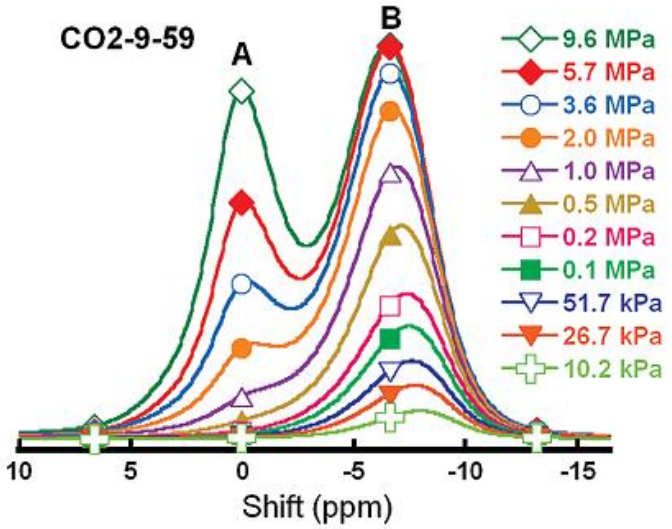

Figure 1. Evolution of the NMR spectra as a function of pressure for CO2-9-59 at 100 K. Peak A on the left evolves linearly with pressure and does not have a significant contribution at low pressures, while peak B is present even at the lowest pressure and approaches saturation at higher pressures.

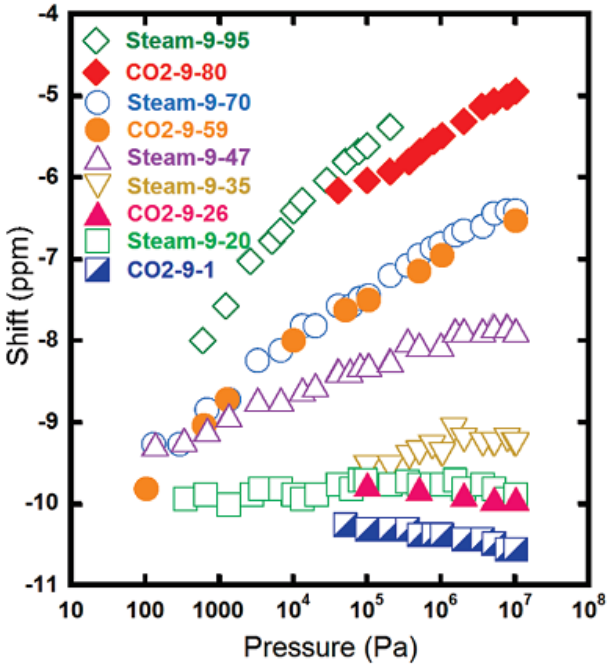

Figure 3. Chemical shift of the micropore peak versus pressure at 100 K. A noticeable change in shift with varied pressure is expected only in samples whose average pore size is larger than ~1.2 nm. All nine samples appear to have the same low-pressure limit of about −10 ppm, indicating little variation in the degree of graphitization of the adsorbent surface. The error of the shift is approximately ±0.2 ppm and is represented by the size of the data points.

Anderson et al., *J. Amer. Chem. Soc.* 2010;132:8618-8626

Espécies adsorvidas em carvões ativados

RMN de ^{1}H :

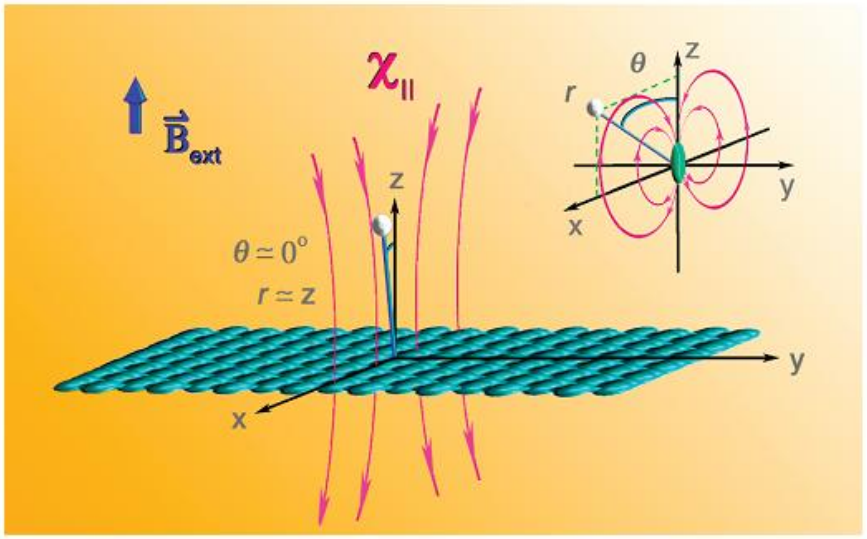

Figure 4. Upper right: Normally, a molecular grouping with an axially symmetric susceptibility tensor has tensor components which are dependent on r, the radial distance of the probe molecule from the center of the grouping; θ, which is the angle between the z-axis and the location of the probe molecule in the $x-z$ plane; and $\chi_{\perp}$ and $\chi_{\parallel}$, which are the molar magnetic susceptibilities of the grouping perpendicular and parallel to the z-axis, respectively ($\chi_{\parallel}$ shown here). Center: For a H_2 molecule adsorbed above a graphene plane and experiencing a local field due to the locally induced dipoles in the plane, $\theta \approx 0°$ and $r \approx z$, corresponding to the vertical distance from the plane.

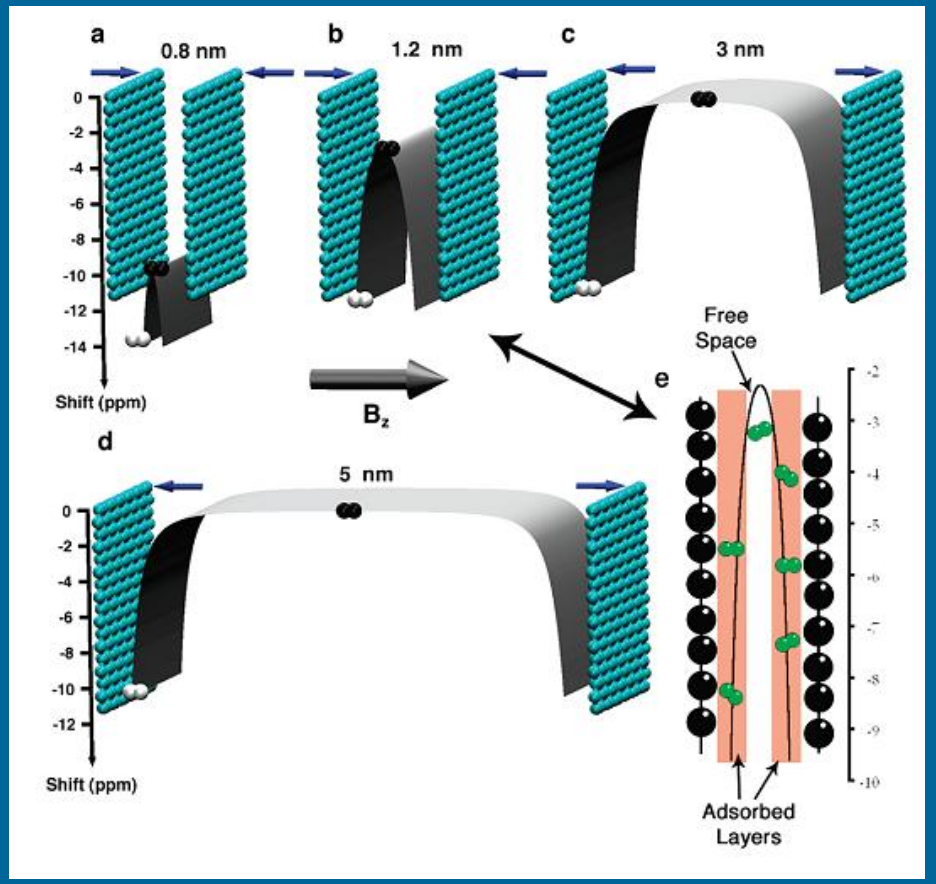

Anderson et al., *J. Amer. Chem. Soc.* 2010;132:8618-8626

Outros materiais de carbono porosos

Carbonos derivados de carbetos (CDCs):

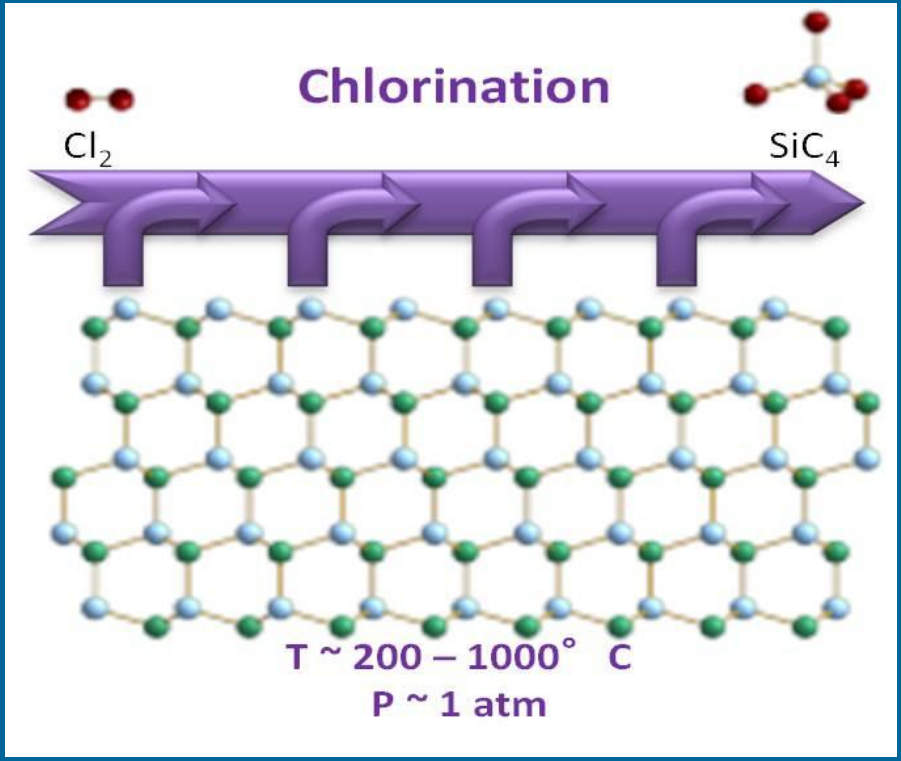

http://en.wikipedia.org/wiki/Carbide-derived_carbon

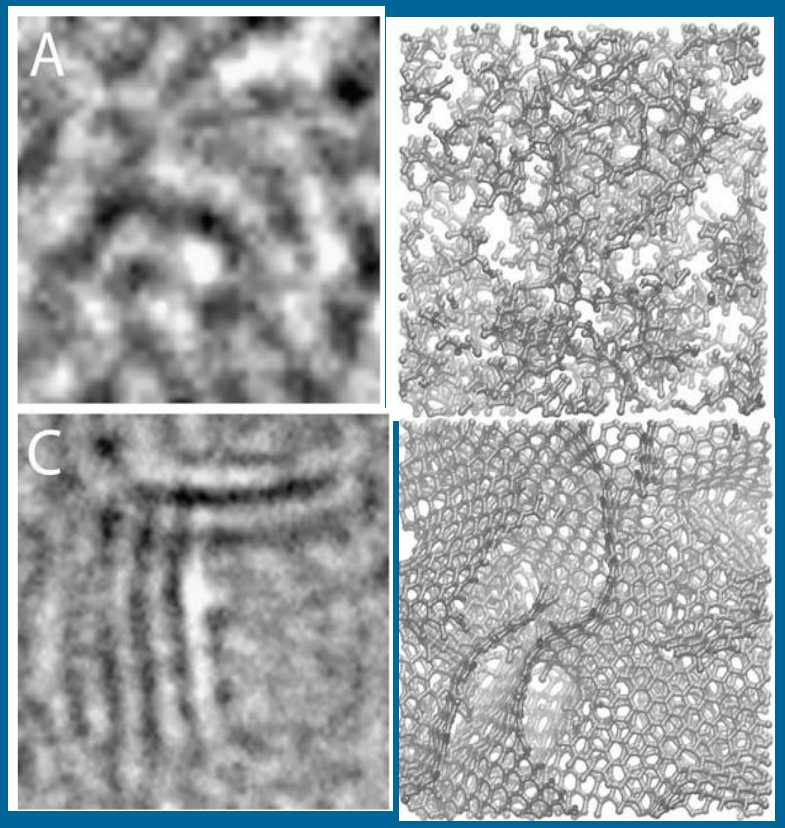

Forse et al., *J. Phys. Chem. C* 2014;118:7508-7514

Outros materiais de carbono porosos

Carbonos derivados de carbetos (CDCs):

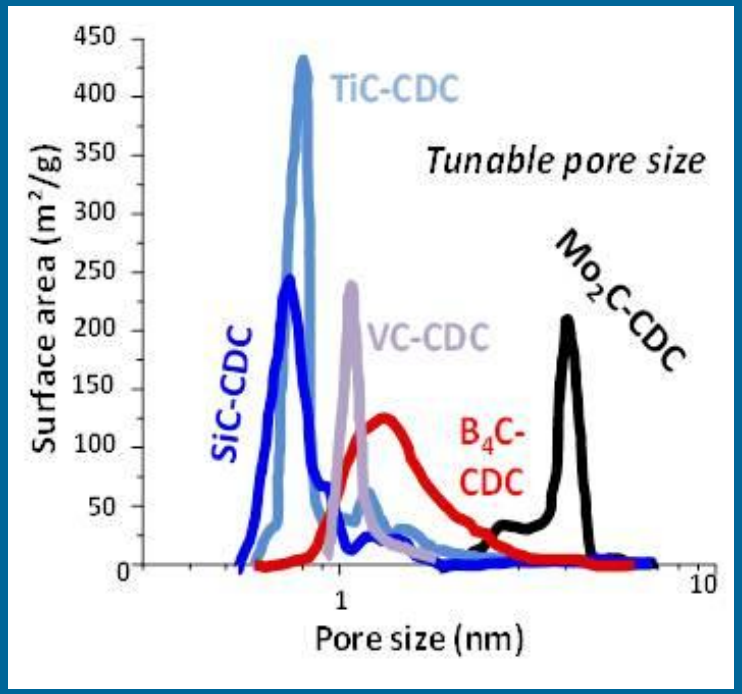

http://en.wikipedia.org/wiki/Carbide-derived_carbon

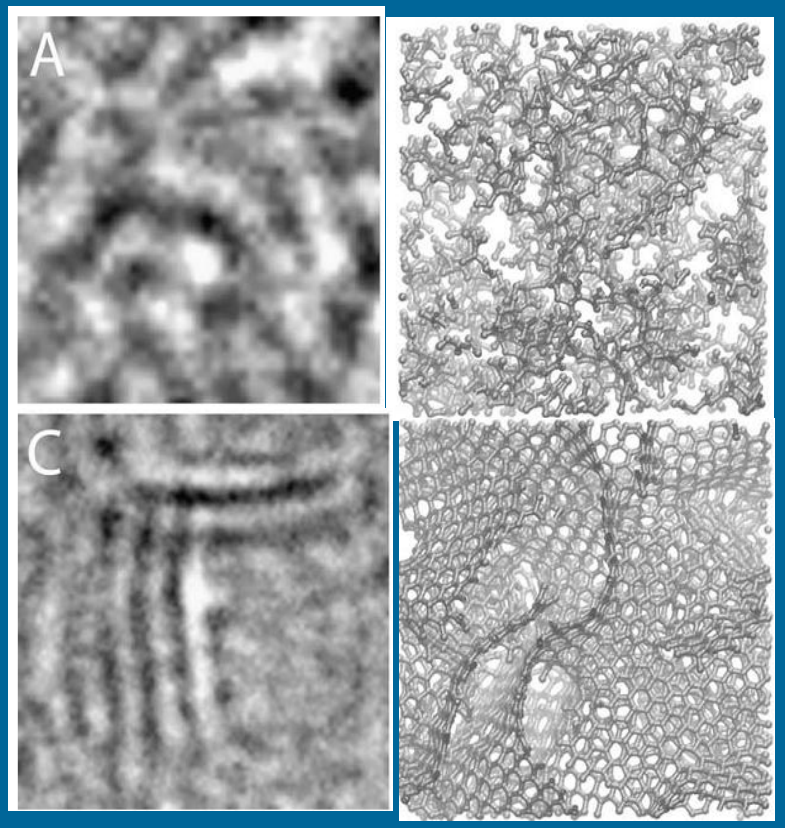

Forse et al., *J. Phys. Chem. C* 2014;118:7508-7514

Outros materiais de carbono porosos

Espécies adsorvidas em CDCs - RMN de ^{19}F:

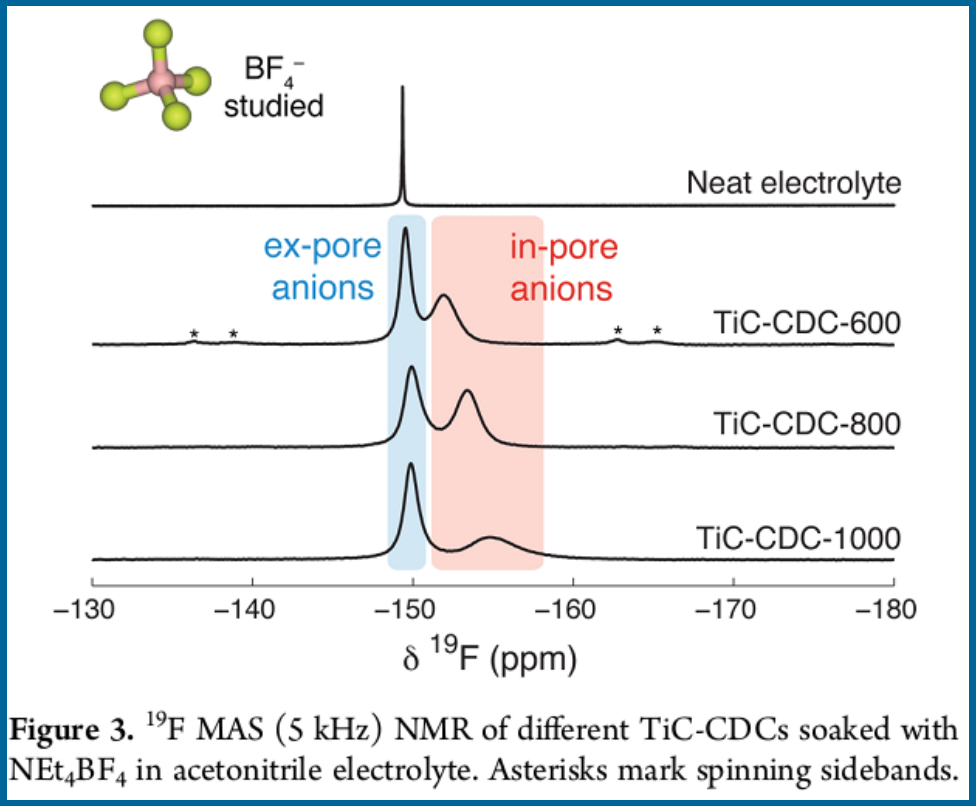

Figure 3. ^{19}F MAS (5 kHz) NMR of different TiC-CDCs soaked with NEt_4BF_4 in acetonitrile electrolyte. Asterisks mark spinning sidebands.

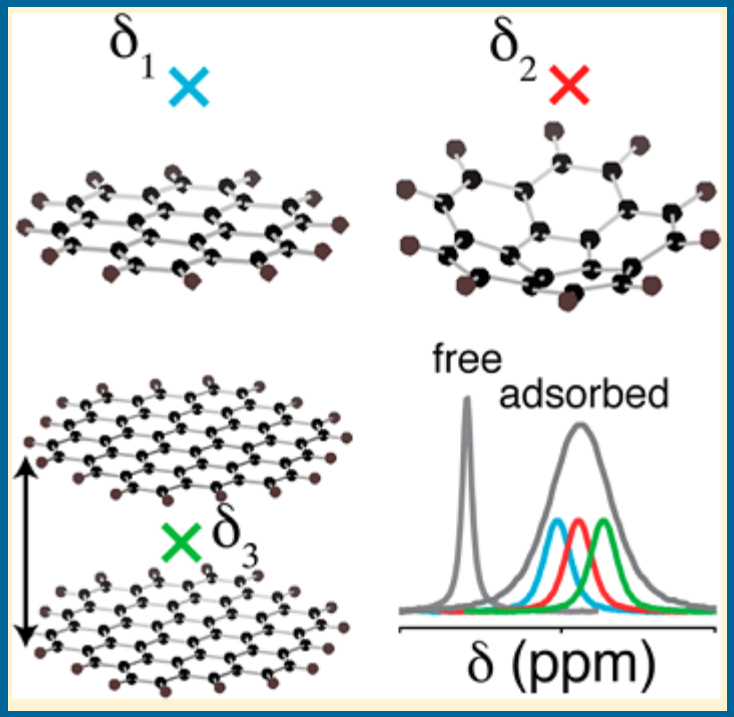

Forse et al., *J. Phys. Chem. C* 2014;118:7508-7514

Outros materiais de carbono porosos

Carbonos mesoporosos:

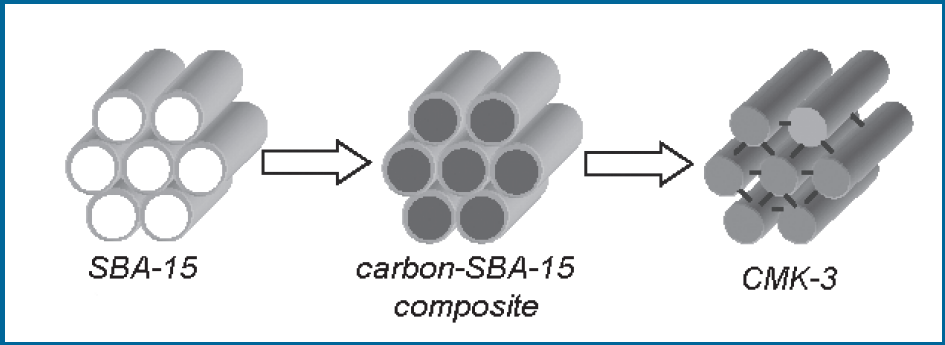

Pastore et al., *J. Braz. Chem. Soc.* 2006;17:16-29

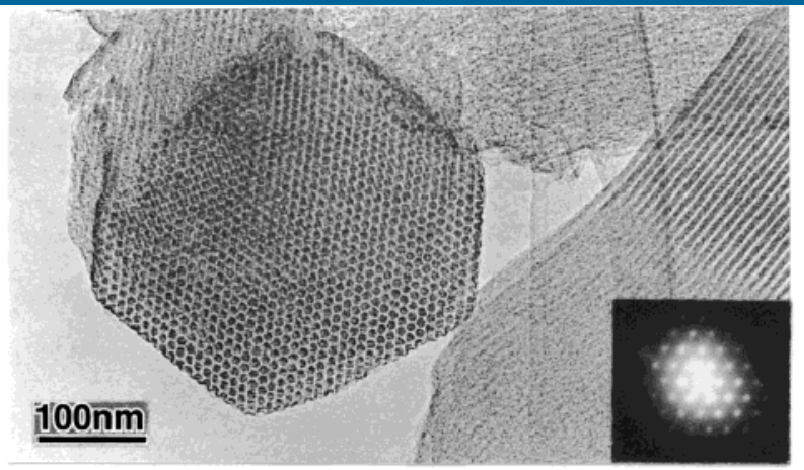

Figure 1. Typical TEM images of the ordered mesoporous carbon molecular sieve, CMK-3. This carbon was synthesized using sucrose as a carbon source and SBA-15 silica as a template. The TEM images were obtained with a JEM-4000 EX operated at 400 kV from the carbon material after silica template was completely removed with HF solution.

Jun et al., *J. Am. Chem. Soc.* 2000;122:10712-10713

Outros materiais de carbono porosos

RMN de ^{129}Xe em carbonos mesoporosos (CMK-3):

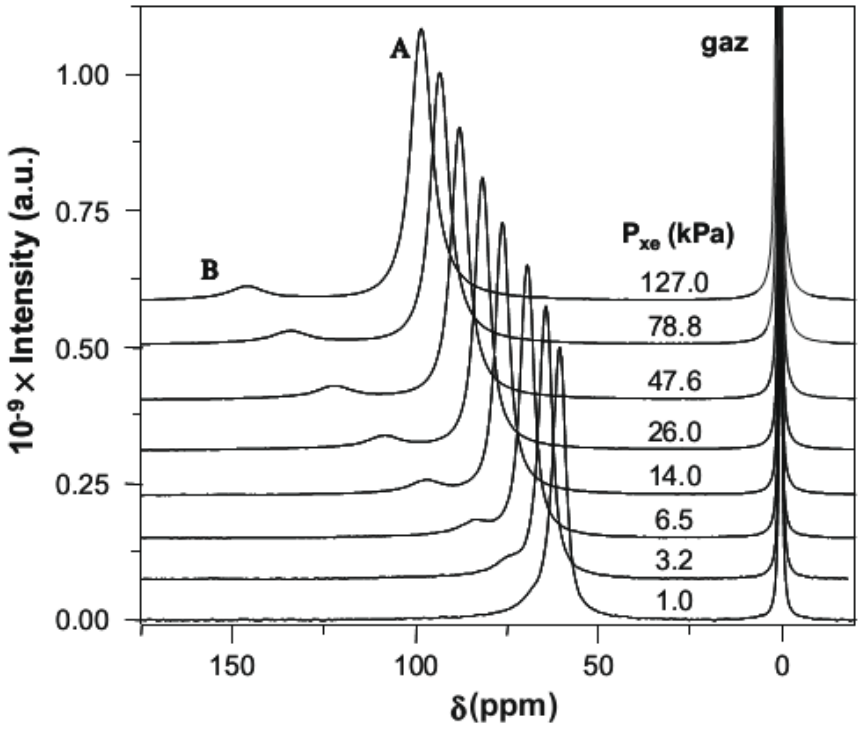

Fig. 3 – Influence of the Xe pressure on NMR spectra of optically polarized ^{129}Xe in CMK-3.

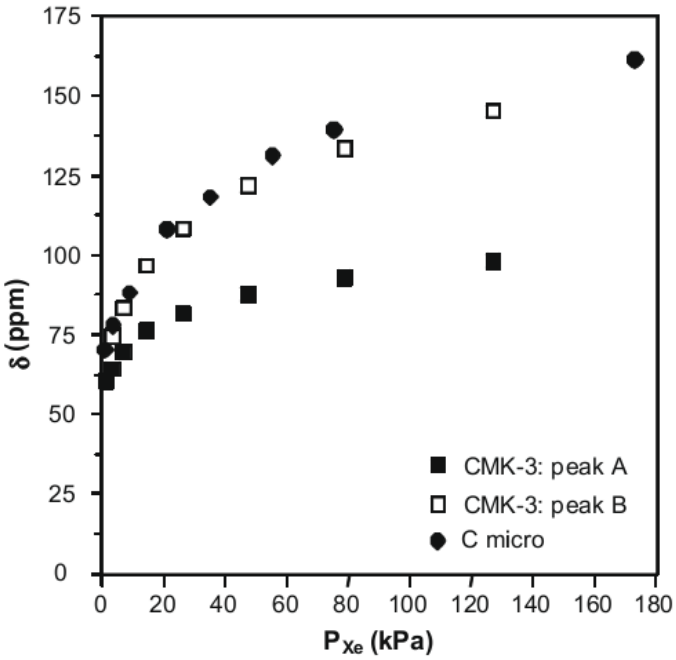

Fig. 4 – ^{129}Xe NMR chemical shift of Xe adsorbed on CMK-3 (■ and □) and C-micro (●) at room temperature.

Onfroy et al., *Carbon* 2009;47:2352-2357

Outros materiais de carbono porosos

RMN de ^{129}Xe em carbonos mesoporosos (CMK-3) – Método *2D Exchange*:

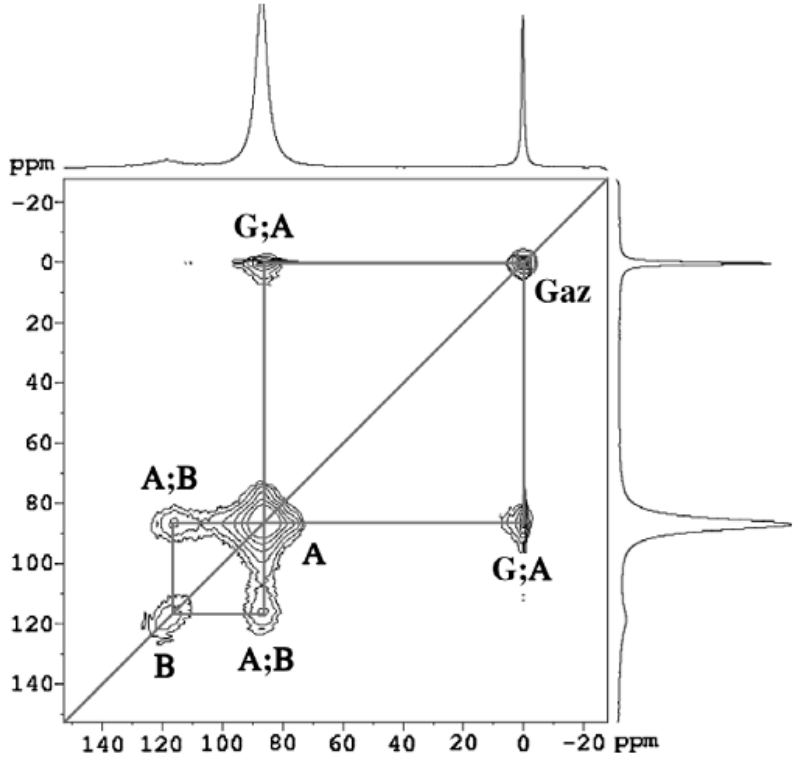

Fig. 6 – ^{129}Xe 2D-EXSY map obtained on CMK-3 at 295 K (P_{Xe} = 53 kPa; mixing time = 50 ms).

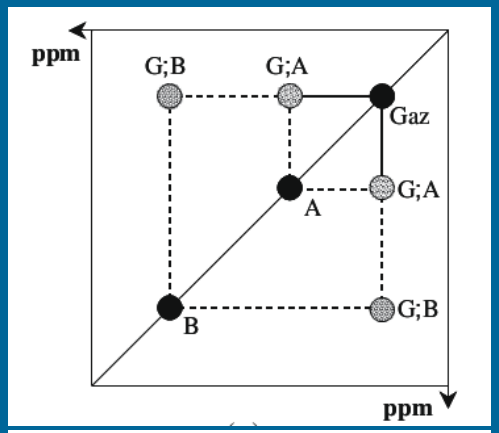

Micro e mesoporos separados

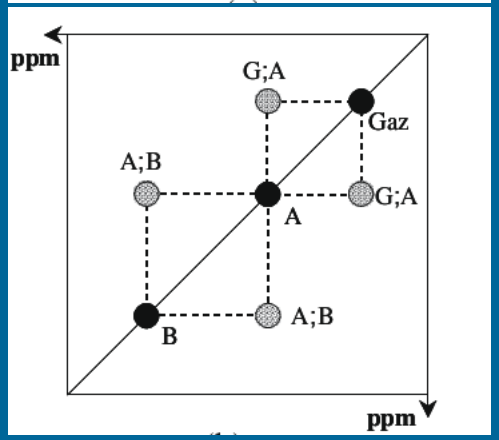

Micro e mesoporos interconectados

Onfroy et al., *Carbon* 2009;47:2352-2357

Outros materiais porosos

Grupos superficiais em sílica mesoporosa:

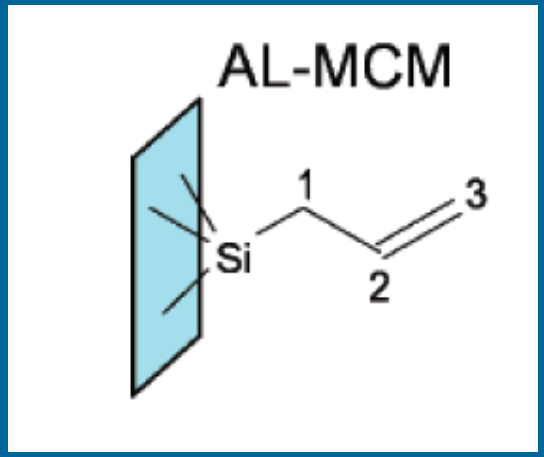

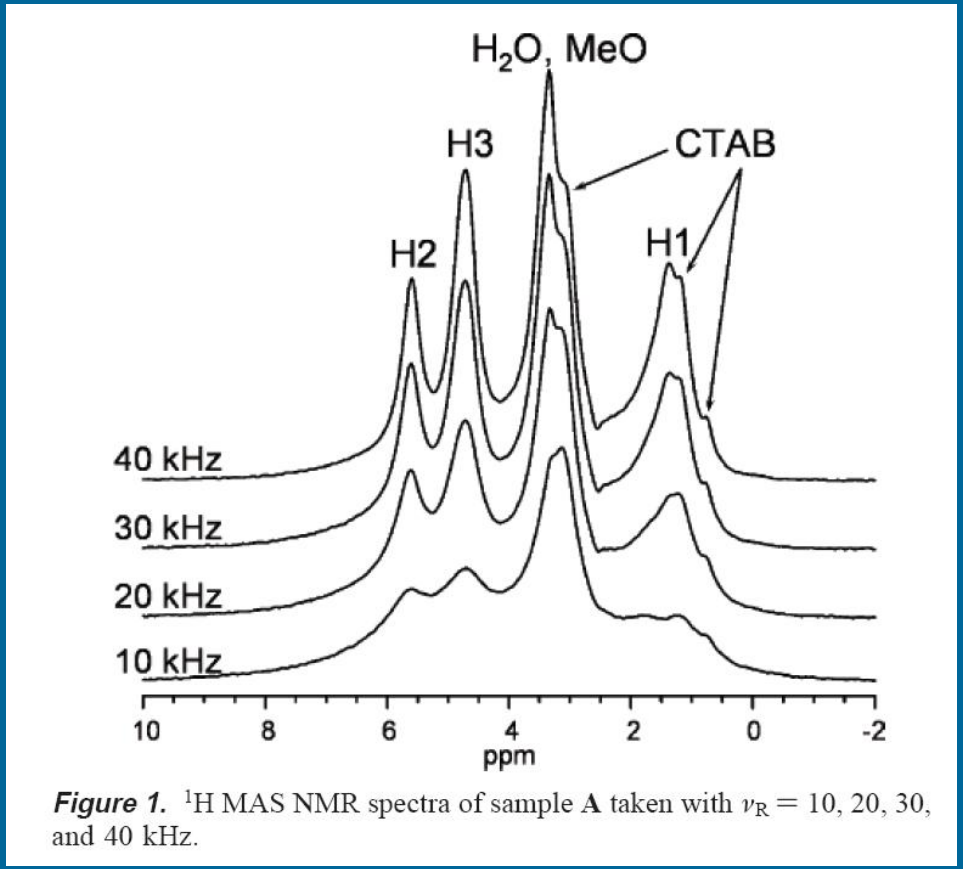

Figure 1. ^{1}H MAS NMR spectra of sample **A** taken with ν_R = 10, 20, 30, and 40 kHz.

Trebosc et al., *J. Am. Chem. Soc.* 2005;127:7587.

Outros materiais porosos

Correlação heteronuclear (^{1}H-^{13}C HETCOR):

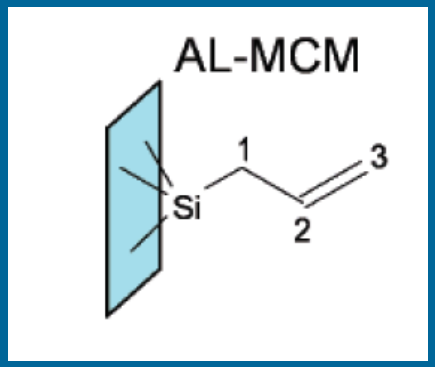

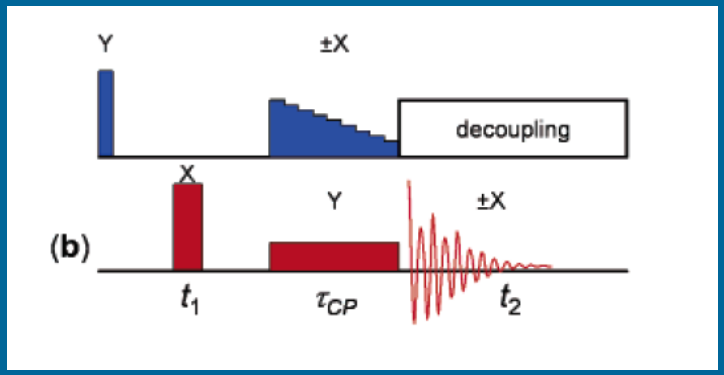

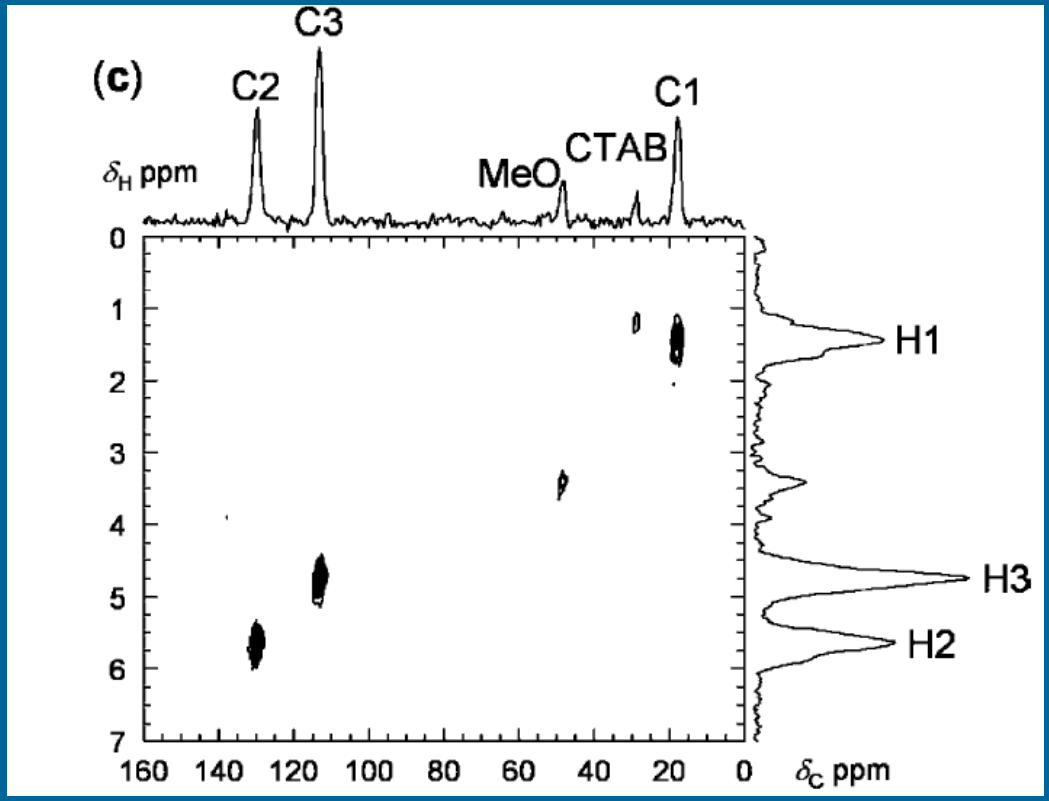

Trebosc et al., *J. Am. Chem. Soc.* 2005;127:7587.

Outros materiais porosos

Detecção de grupos superficiais – uso de *polarização dinâmica nuclear* (DNP) :

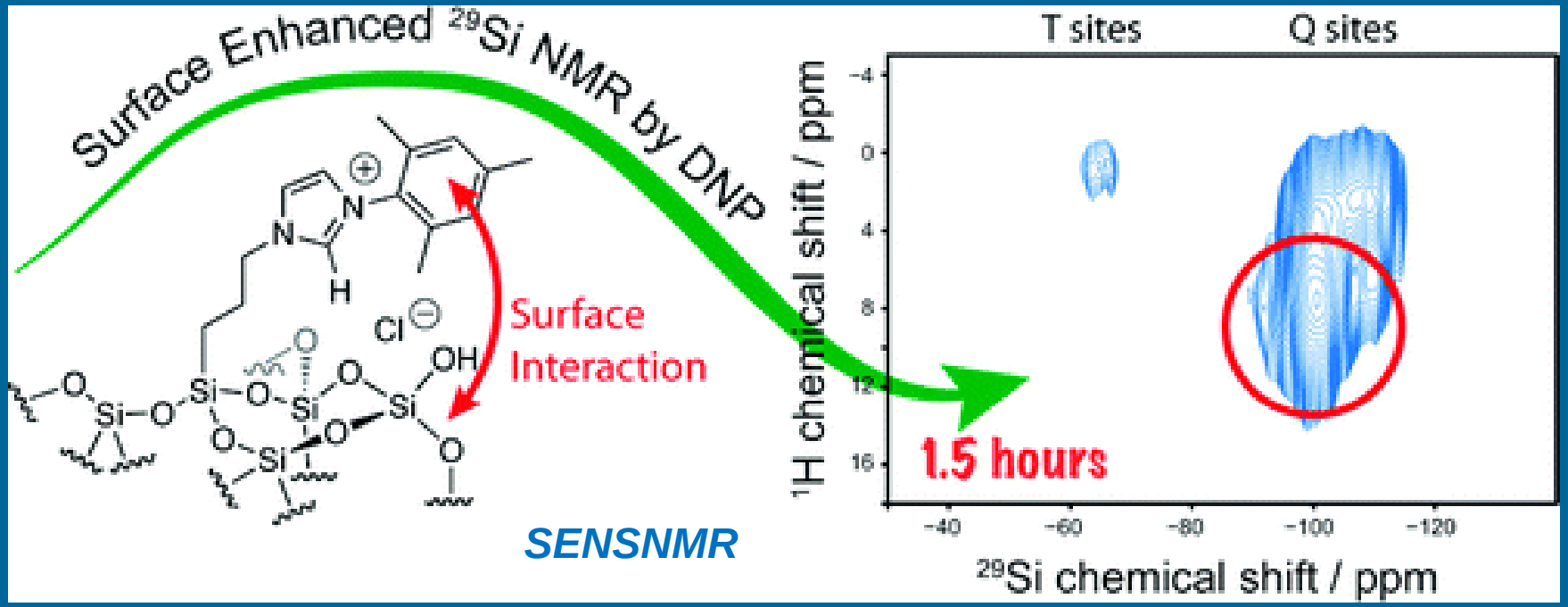

Emsley et al., *J. Am. Chem. Soc.* 2011;133:2104

Impregnação incipiente do material poroso (sílica, alumina, etc.) com uma solução contendo o agente polarizador (com radicais livres).

Outros materiais porosos

RMN de ^{29}Si em sílica – Método SENSNMR:

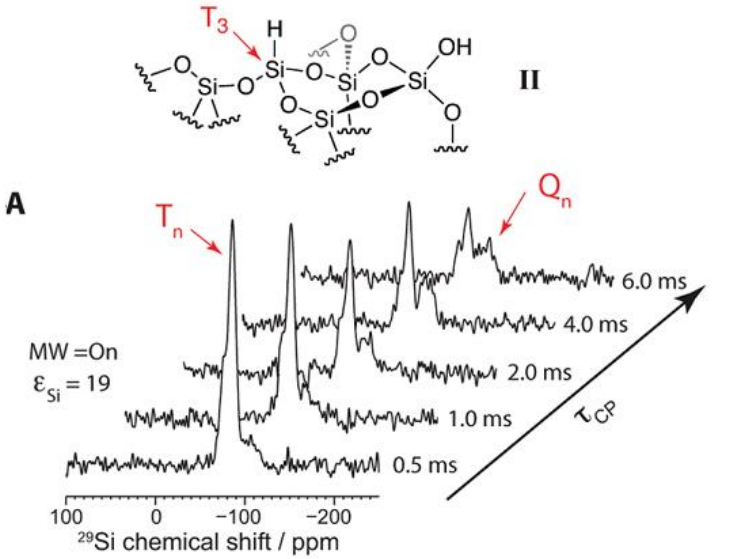

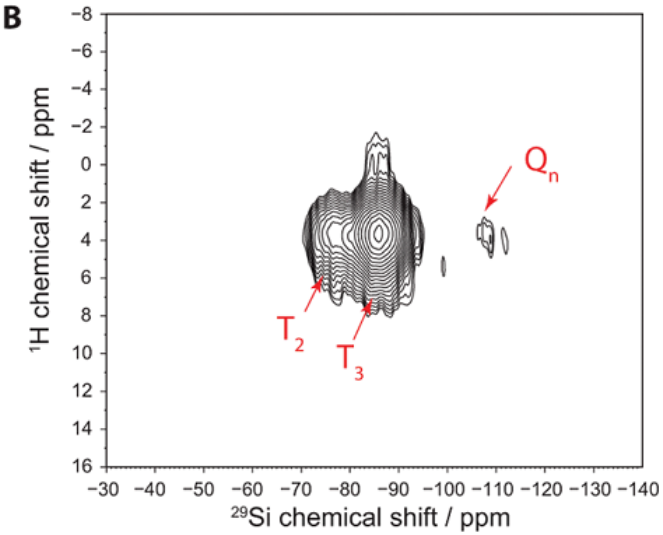

Figure 2. (A) DNP-enhanced silicon-29 CPMAS spectra of **II** as a function of the CP mixing time τ_{CP}. Spectra were recorded with 16 scans. (B) Contour plot of a two-dimensional $^{1}H-^{29}Si$ spectrum of **II** recorded with DNP. 64 t_1 increments with eight scans each were recorded with τ_{CP} = 1.0 ms. Total experimental time was 8.5 min.

Emsley et al., *J. Am. Chem. Soc.* 2011;133:2104

Outros materiais porosos

Estudos de estruturas metal-orgânicas ("*metal-organic frameworks*" – MOFs):

Figure 1. Schematic representation of the metal–organic frameworks (MOF lattice (here: DUT-8(Ni) [23]), consisting of organic linkers and inorganic secondary building units (SBUs). The MOF serves as a host structure for guests such as ^{129}Xe within the void spaces. C: grey, H: white, N: blue, O: red, Ni: green, Xe: cyan.

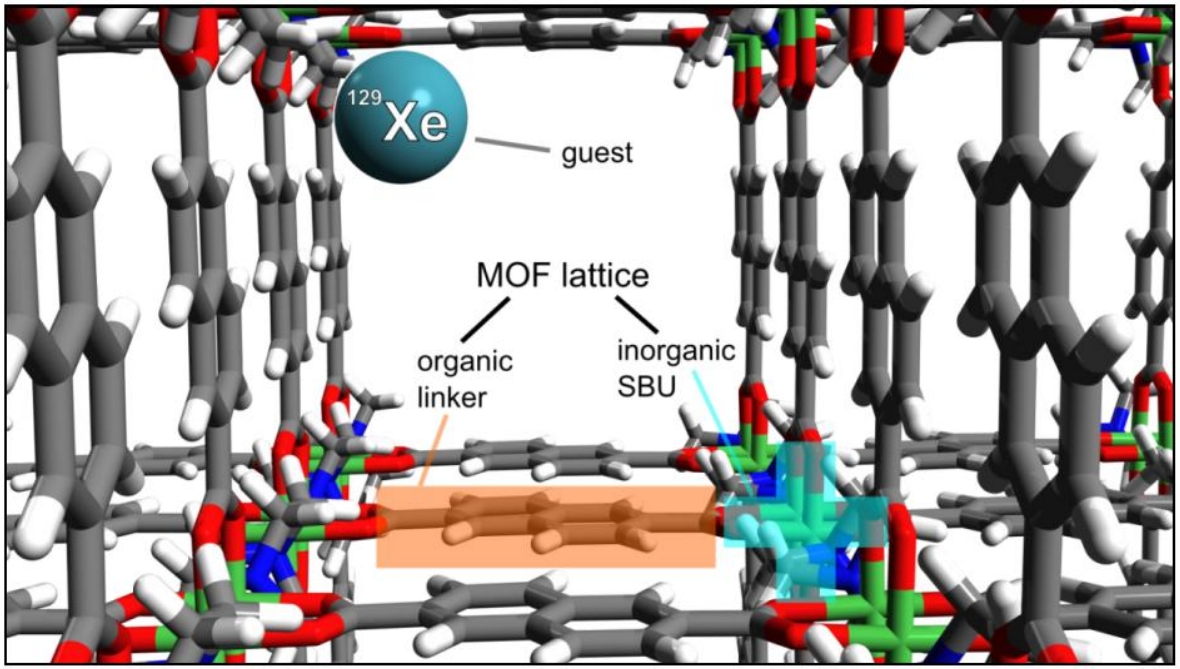

Hoffmann et al., *Materials* 2012;5:2537-2572

Outros materiais porosos

Estudos por RMN de moléculas adsorvidas em MOFs:

Figure 16. High-pressure apparatus for *in situ* NMR studies of gas adsorption. Reprinted with permission from [183]. Copyright 2011 American Chemical Society.

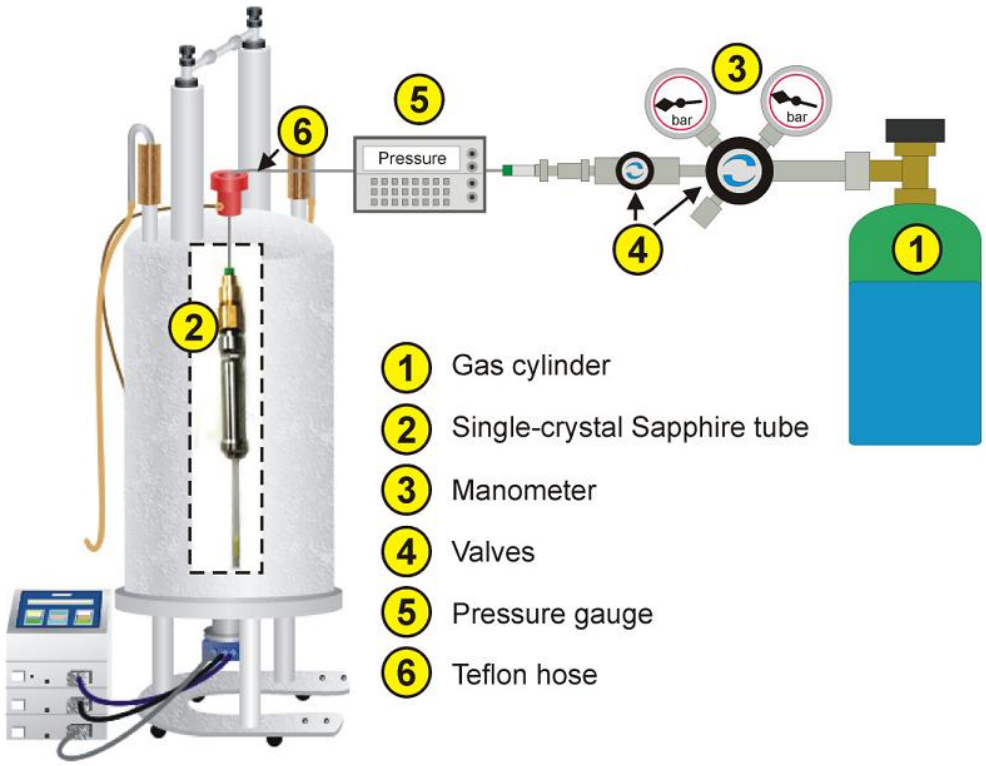

Hoffmann et al., *Materials* 2012;5:2537-2572

Outros materiais porosos

Estudos por RMN de moléculas adsorvidas em MOFs:

Figure 15. Schematic: MAS NMR of a sample sealed into a glass ampoule.

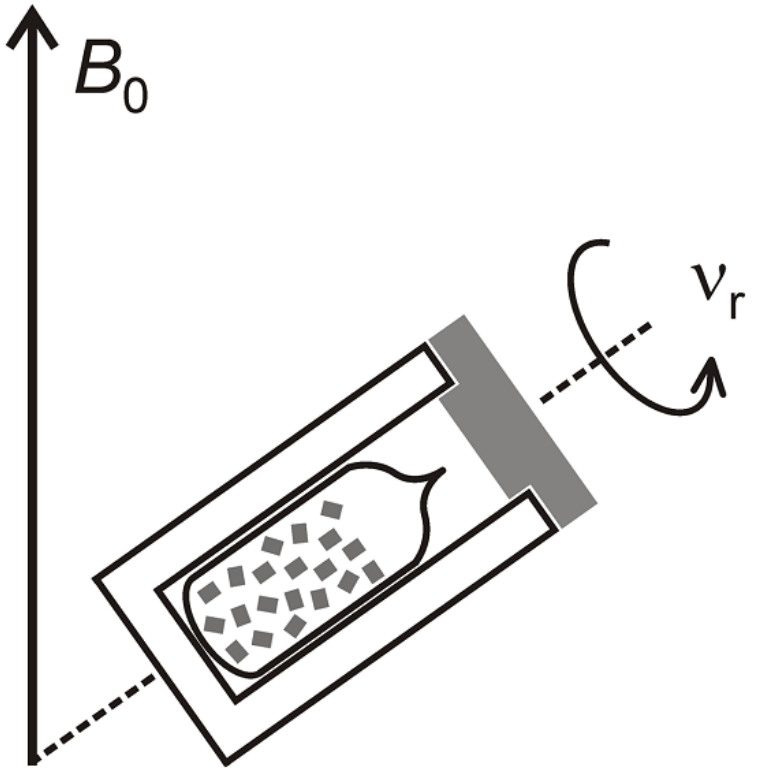

Hoffmann et al., *Materials* 2012;5:2537-2572

Outros materiais porosos

Estudos por RMN de moléculas adsorvidas em MOFs:

Figure 13. ^{129}Xe NMR spectra of DUT-8(Ni) pressurized with various amounts of xenon, measured at 237 K. Note that the initially closed structure opens during the adsorption experiment at a gate-opening pressure of *ca.* 12 bar whereas it remains open during desorption down to 1 bar (hysteresis). Reprinted with permission from [183]. Copyright 2011 American Chemical Society.

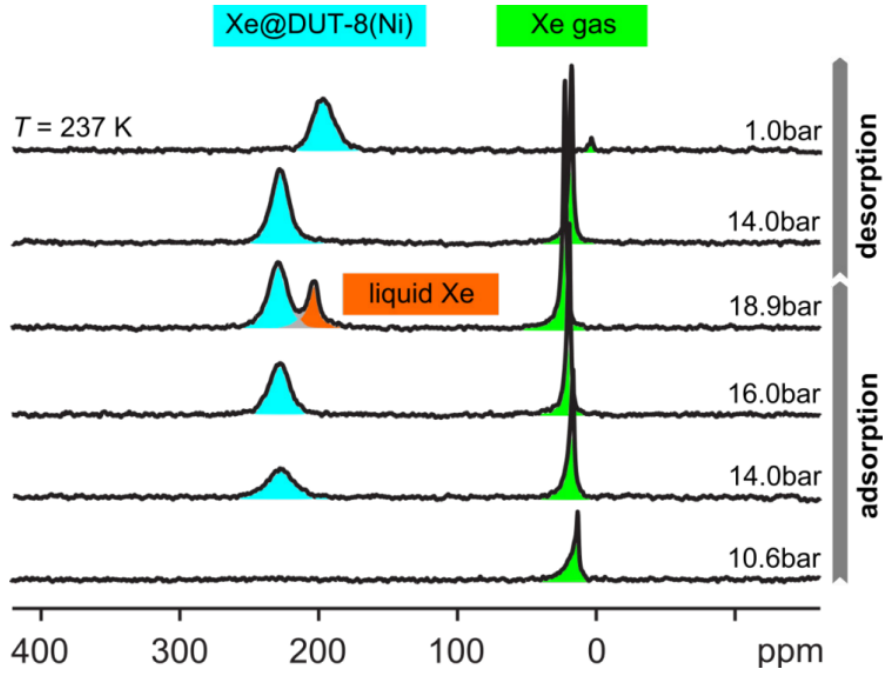

Hoffmann et al., *Materials* 2012;5:2537-2572

Outros materiais porosos

Estudos por RMN de moléculas adsorvidas em MOFs:

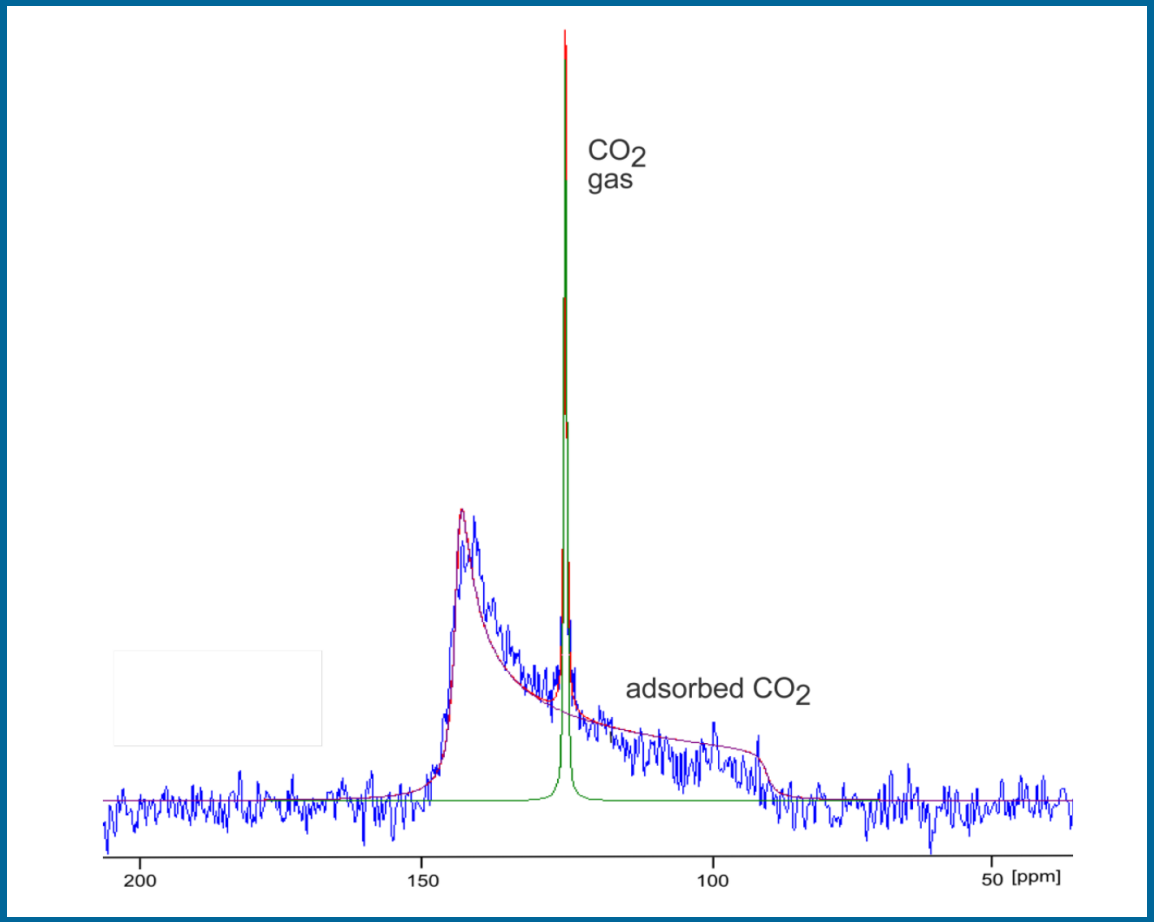

Figure 14. ^{13}C NMR spectrum of DUT-8(Ni) pressurized with 9.5 bar carbon dioxide measured at 237 K. Note that the initially closed structure opens during the adsorption experiment at temperature-dependent gate-opening pressure (*ca.* 5 bar at 237 K) whereas it remains open during desorption down to 1 bar (hysteresis). (Blue: experimental spectrum, green: simulated gas phase signal, magenta: simulated signal of adsorbed CO_2; red: Sum of the simulated signals.) The Figure has been prepared using DMFit [202].

Hoffmann et al., *Materials* 2012;5:2537-2572

Outros materiais porosos

Estudos por RMN de moléculas adsorvidas em MOFs:

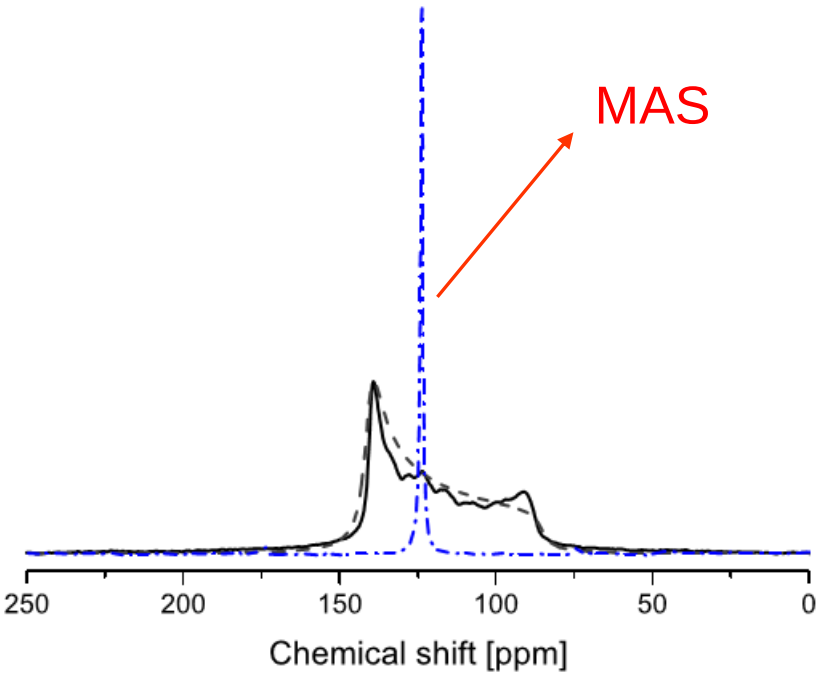

Fig. 2. ^{13}C NMR spectra of $^{13}CO_2$ adsorbed in DMOF-1. The broad static powder spectrum (black full line) was fitted by Pake pattern (gray dashed line). The narrow (blue dashed-dotted) line represents the ^{13}C MAS NMR spectrum of a corresponding sample spinning at 5 kHz.

Stallmach et al., *Microporous Mesoporous Mater.* 2015;205:11-15

Outros materiais porosos

Estudos por RMN de moléculas adsorvidas em MOFs:

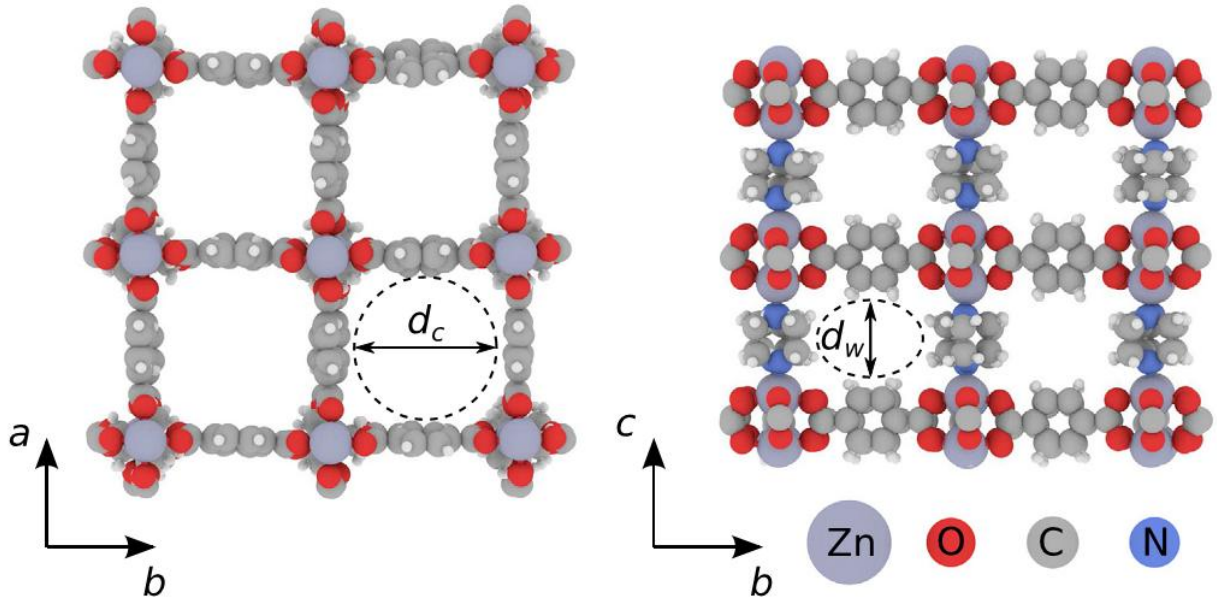

Fig. 1. Structure of the metal–organic framework DMOF-1 viewed perpendicular to the *ab* plane (left) illustrating the size of the nanochannels ($d_c = 0.75$ nm) in *c* direction and perpendicular to the *bc* plane (right) showing the smaller windows ($d_w = 0.40$ nm) connecting the nanochannels.

Stallmach et al., *Microporous Mesoporous Mater.* 2015;205:11-15

Outros materiais porosos

Estudos por RMN de moléculas adsorvidas em MOFs – efeitos de difusão:

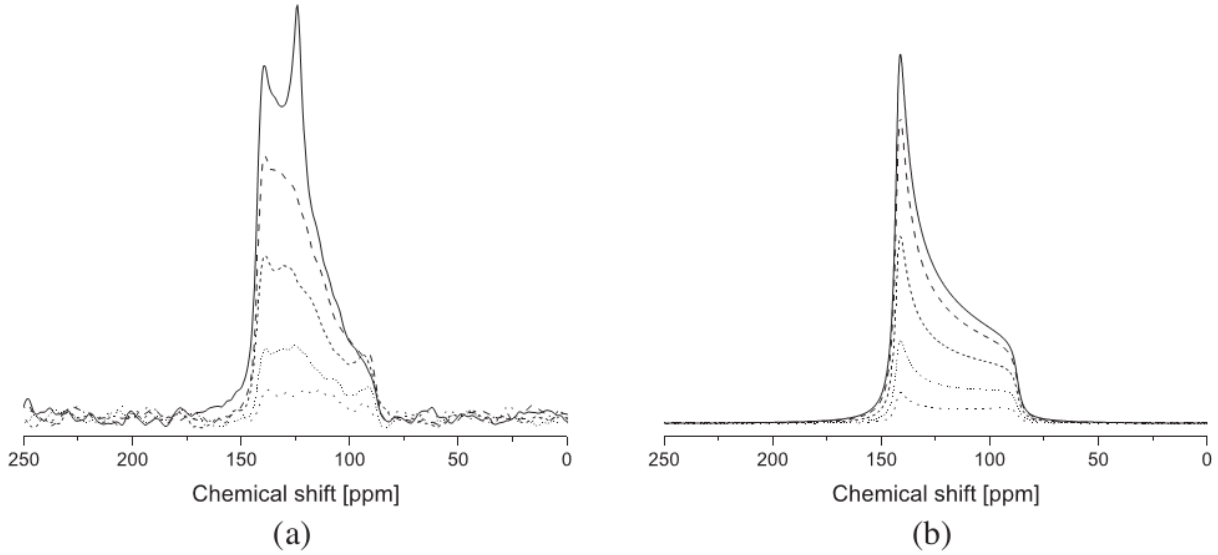

Fig. 6. (a) ^{13}C PFG NMR spectra of carbon dioxide in DMOF-1 measured under the influence of pulsed field gradients in *x*-direction. The distribution of orientations in the sample is not perfectly isotropical. There is a narrow peak of gaseous CO_2 contributing to the first spectrum. (b) Simulation of the diffusion attenuation with an anisotropy of $\eta = 3$ (all other parameters were the same as in Fig. 5(a)).

Stallmach et al., *Microporous Mesoporous Mater.* 2015;205:11-15

Bibliografia recomendada

- Fundamentos de RMN:
  - "**Spin Dynamics**", M. H. Levitt. John Wiley & Sons, 2002.
  - "**Principles of nuclear magnetic resonance in one and two dimensions**", R. R. Ernst, G. Bodenhausen, A. Wokaun. Oxford, 1987.
  - "**Ressonância magnética nuclear: fundamentos, métodos e aplicações**", V. M. S. Gil, C. F. G. C. Geraldes. Fundação Calouste Gulbekian, 1987.

Bibliografia recomendada

- Aplicações em ciência dos materiais:
  - "**Multinuclear solid-state NMR of inorganic materials**", K. J. D. Mackenzie, M. E. Smith, Pergamon, 2002.
  - "**NMR techniques and applications in geochemistry and soil chemistry**", M. A. Wilson, Oxford, 1987.
- Aplicações em petrofísica:
  - "**NMR Logging: Principles and Applications**", G. Coates, L. Xiao,M. G. Prammer, Halliburton Energy Services, 1999.

Agradecimentos

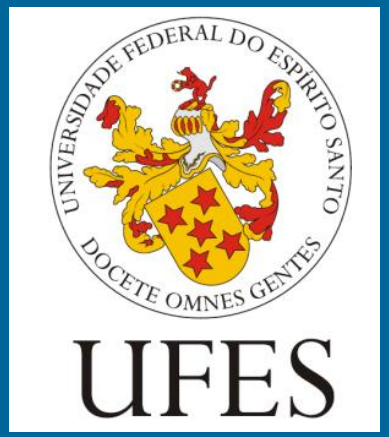

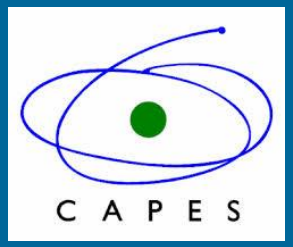

Contato: dúvidas, comentários, sugestões, etc.

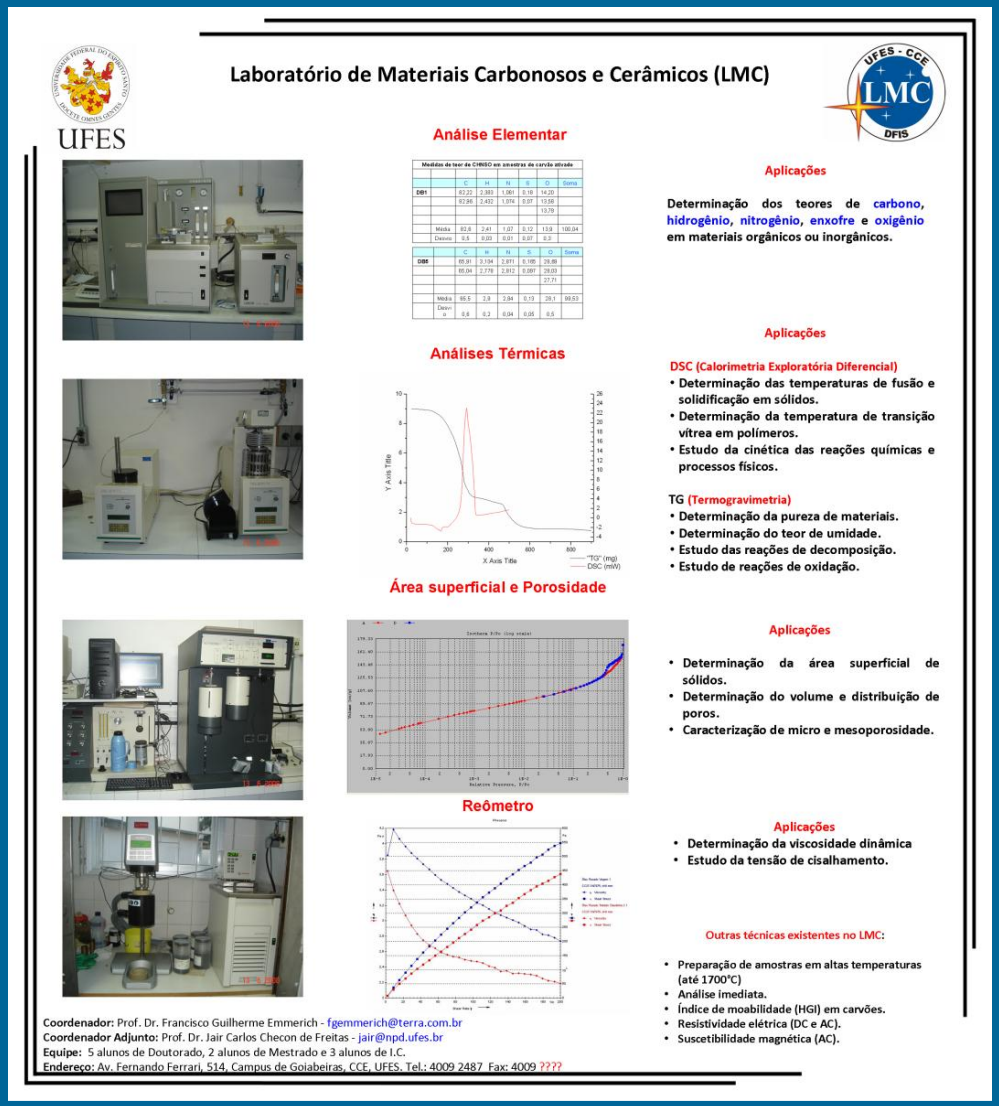

Laboratório de Materiais Carbonosos e Cerâmicos (LMC)

UFES

UFES - CCE LMC DFIS

Análise Elementar

Medidas de teor de CHNSO em amostras de carvão ativado

		C	H	N	S	O	Soma
DB1		82,22	2,383	1,061	0,18	14,20	
		82,96	2,432	1,074	0,87	12,58	
						13,79	
	Média	82,6	2,41	1,07	0,12	13,9	100,04
	Desvio	0,5	0,03	0,01	0,07	0,3	

		C	H	N	S	O	Soma
DB5		85,91	3,104	2,871	0,185	28,88	
		85,04	2,778	2,812	0,897	28,03	
						27,71	
	Média	85,5	2,9	2,84	0,13	28,1	99,53
	Desvio	0,6	0,2	0,04	0,05	0,5	

Aplicações

Determinação dos teores de carbono, hidrogênio, nitrogênio, enxofre e oxigênio em materiais orgânicos ou inorgânicos.

Análises Térmicas

Aplicações

DSC (Calorimetria Exploratória Diferencial)
- Determinação das temperaturas de fusão e solidificação em sólidos.
- Determinação da temperatura de transição vítrea em polímeros.
- Estudo da cinética das reações químicas e processos físicos.

TG (Termogravimetria)
- Determinação da pureza de materiais.
- Determinação do teor de umidade.
- Estudo das reações de decomposição.
- Estudo de reações de oxidação.

Área superficial e Porosidade

Aplicações

- Determinação da área superficial de sólidos.
- Determinação do volume e distribuição de poros.
- Caracterização de micro e mesoporosidade.

Reômetro

Aplicações
- Determinação da viscosidade dinâmica
- Estudo da tensão de cisalhamento.

Outras técnicas existentes no LMC:
- Preparação de amostras em altas temperaturas (até 1700°C)
- Análise imediata.
- Índice de moabilidade (HGI) em carvões.
- Resistividade elétrica (DC e AC).
- Suscetibilidade magnética (AC).

Coordenador: Prof. Dr. Francisco Guilherme Emmerich - fgemmerich@terra.com.br
Coordenador Adjunto: Prof. Dr. Jair Carlos Checon de Freitas - jair@npd.ufes.br
Equipe: 5 alunos de Doutorado, 2 alunos de Mestrado e 3 alunos de I.C.
Endereço: Av. Fernando Ferrari, 514, Campus de Goiabeiras, CCE, UFES. Tel.: 4009 2487 Fax: 4009 ????

Jair C. C. Freitas

Departamento de Física - UFES
jairccfreitas@yahoo.com.br
www.cce.ufes.br/jair